POROUS SILICON WAVEGUIDE BIOSENSORS WITH A GRATING COUPLER

By

Xing Wei

Dissertation

Submitted to the Faculty of the

Graduate School of Vanderbilt University

in partial fulfillment of the requirements

for the degree of

DOCTOR OF PHILOSOPHY

in

Electrical Engineering

May, 2012

Nashville, Tennessee

Approved:

Professor Sharon M. Weiss

Professor Bharat L. Bhuva

Professor Deyu Li

Professor Ronald D. Schrimpf

Professor Yaqiong Xu

To my beloved husband, Liyun, infinitely supportive

ACKNOWLEDGEMENTS

This work would not have been possible without the financial support of the National Science Foundation and Army Research Office, the technical support of Vanderbilt Institute of Nanoscale Science and Engineering and Center for Nanophase Materials Sciences of Oak Ridge National Laboratory.

I am grateful to all of those with whom I have had the pleasure to work during this project. Each member of my dissertation committee provided professional comments and guidance on this scientific research. I would especially express my gratitude to my academic advisor, Dr. Sharon M. Weiss, for her patience, encouragement, and criticism throughout my Ph.D. study. I really appreciate the pleasant cooperation with Dr. John E. Sipe of the University of Toronto and his post-docs Marco Liscidini. Without their theoretical work, the research would not be possible. I thank Mr. John Jackson of Metricon, Corp. for helping me with the prism coupler usage and maintenance.

I have had the pleasure to work with many post-docs and students at Vanderbilt University in the past 5 years, including Yandong Gao and Jiashu Sun of Mechanical Engineering, present and past members of the Weiss Group: Chris Kang, Jenifer L. Lawrie, Yang Jiao, Judson Ryckman, Dr. Jeremy Mares, Dr. Guoguang Rong, et al. Last, I would like to thank my husband for his understanding, endless love and encouragement. His support and help was in the end to make this dissertation possible. My parents receive my deepest gratitude and love for education and support ever since I was born.

TABLE OF CONTENTS

Page

ACKNOWLEDGEMENTS iii

Table of Contents iv

LIST OF TABLES vi

LIST OF FIGURES vii

Chapter

I INTRODUCTION 1

1.1 Introduction to biosensing 1
1.2 Introduction to porous silicon 3
1.2.1 Porous silicon background 3
1.2.2 PSi biosensors 4
1.2.3 Formation mechanism of PSi 9
1.3 Waveguide coupler structure 12
1.3.1 Waveguide 12
1.3.2 Coupling methods 15
1.4 Experimental instrument 22
1.5 Objective and overview of the dissertation 23

II PHOTORESIST GRATING COUPLED PSI WAVEGUIDE BIOSENSOR 26

2.1 Fabrication 27
2.1.1 PSi waveguide fabrication 27
2.1.2 Oxidation 28
2.1.3 Fabrication of photoresist grating coupled PSi waveguide 35
2.2 Photoresist grating coupled PSi waveguide characterization 40
2.2.1 Spectrum characterization 40
2.2.2 Infiltration effect with 3-APTES 43
2.3 DNA experiments 45
2.3.1 Surface functionalization 45
2.3.2 DNA hybridization 48
2.4 Conclusion 51

III ALL-PSI GRATING-COUPLED WAVEGUIDE BIOSENSOR 53

3.1 Theoretical Comparison 53

3.2 Fabrication 58
3.3 DNA hybridization experiments 61
3.3.1 All-PSi grating-coupled waveguide biosensor 61
3.3.2 Photoresist grating biosensor & SOI waveguide biosensor 66
3.4 Stamped grating-coupled PSi waveguide biosensor 68
3.4.1 Fabrication of stamped gratings 68
3.4.2 Waveguide loss measurement 70
3.4.3 DNA Hybridization 72
3.5 Conclusion 74

IV INTEGRATED PSI WAVEGUIDE BIOSESNOR 76

4.1 Adsoprtion kinetics in PSi 76
4.2 Fabrication 81
4.3 NaCl solution measurement 83
4.4 Biomolecule kinetics in PSi 85
4.5 Conclusion 89

V Conclusions and Future Work 91

5.1 Conclusions and research contribution 91
5.2 Future research opportunities 92

Appendix

MULTI-LAYER REFLECTANCE VS. INCIDENT ANGLE MATLAB CALCULATION CODE 98

MULTI-LAYER REFLECTANCE VS. WAVELENGTH MATLAB CALCULATION CODE 100

WAVEGUIDE ELECTRICAL FIELD DISTRIBUTION MATLAB CALCULATION CODE 102

REFERENCES 104

LIST OF TABLES

Table Page

Table 1. 1 Different PSi structures and their corresponding reflectance spectra before (blue) and after (red) an increase in refractive index of all layers by 0.1: single layer, double-layer waveguide, multilayer, and microcavity. 7

Table 3. 1 Resonance angle shifts after various molecular attachments in all-PSi grating-coupled waveguide, photoresist grating-coupled PSi waveguide, and SOI waveguide with SiO_2 gratings. 68

Table 4. 1 Diffusion coefficient, adsorption and desorption rate constants of 3-APTES, Sulfo-SMCC, probe DNA and antisense PNA in PSi. 88

LIST OF FIGURES

Figure Page

Figure 1. 1 Number of publications per year regarding PSi [44]. 4

Figure 1. 2 Progress in the development of theories on formation mechanisms of PSi (adapted from [77], reproduced by permission of ECS – The Electrochemical Society). 9

Figure 1. 3 Mechanism of PSi formation on p-type silicon [85]. 11

Figure 1. 4 (a) Band diagram of the p-Si/PSi/HF solution interface under current flow. (b) Schematic of the PSi etching cell. 12

Figure 1. 5 Waveguiding in a simple planar waveguide. 13

Figure 1. 6 (a) Ray depiction of three allowed modes in a waveguide. (b) Three TE modal field patterns of the waveguide. 13

Figure 1. 7 Left: Simulation of the light propagation in a planar PSi waveguide close to the site of light injection. Light is confined in the waveguiding film layer and exponentially decays into the air and the substrate. Right: Intensity profile along the surface. [89] 15

Figure 1. 8 Four techniques for coupling light into optical waveguides. 16

Figure 1. 9 Schematic of a prism coupler on a waveguide..... 18

Figure 1. 10 Schematic of a grating coupler on a waveguide. The incident beam (I_0), reflected beam (R), first-order defracted beam (I_{-1}), and guided optical beam (G) are shown. Insertion: spatial phase modulation caused by the gratings. 21

Figure 1. 11 Schematics of the measurement system of the Metricon Model 2010/M instrument: (a) the prism coupler mode; (b) the VAMFO mode. 23

Figure 2. 1 Cross-section SEM image of two-layer porous silicon waveguides. The brighter regions are the nanoscale silicon matrix and the dark regions are void spaces. 28

Figure 2. 2 Theoretical calculation of grating coupled PSi waveguide showing the waveguide resonance angle shift to smaller angles with a reduction in PSi refractive index associated with various levels of oxidation. 29

Figure 2. 3 Geometrical model for (a) as-anodized PSi, which includes air (ε_1) and silicon (ε_3); (b) model for oxidized PSi, which includes air (ε_1), SiO_2 (ε_2) and silicon (ε_3). [82] 31

Figure 2. 4 Refractive index shifts of PSi single layer after oxidation at various temperatures for five minutes..... 33

Figure 2. 5 Change of PSi porosity (a) and SiO_2 thickness (b) after oxidation. 33

Figure 2. 6 Refractive index change of PSi layer due to 3-APTES attachment at different oxidation temperatures. Saturation of the refractive index shift is expected when 3-APTES monolayer coverage in the pores is complete..... 35

Figure 2.7 Experimental and theoretical values for the reflectance of one PSi waveguide sample [125]. 37

Figure 2.8 Top-view (a) and section-view (b) SEM images of a photoresist grating coupled PSi waveguide structure. 40

Figure 2. 9 Experimental and theoretical reflectance as a function of the angle of incidence for the PSi waveguide with the grating coupler. 41

Figure 2. 10 Theoretical transmittance as a function of the angle of incidence for the PSi waveguide with the grating coupler. 42

Figure 2. 11 Principle of reversibility in reflection [128]. 43

Figure 2. 12 (a) Measured and (b) calculated angle-resolved reflectance at 1550 nm for empty (solid line) and infiltrated (dashed line) PSi waveguide with a photoresist grating coupler. 45

Figure 2. 13 PSi waveguide surface functionalization procedure..... 46

Figure 2. 14 Photoresist grating coupled PSi waveguide reflectance spectra after oxidation and attachment of 3-APTES, Sulfo-SMCC, and probe DNA. The resonance shifts confirm the attachment of these molecules in the oxidized PSi waveguide [116]. 48

Figure 2. 15 Resonance shifts of grating-coupled PSi waveguides after exposure to (a) antisense DNA, (b) mismatch DNA, and (c) HEPES buffer. Selectivity and stability of the PSi waveguide sensor is demonstrated. 50

Figure 2. 16 Resonance angle shifts due to different antisense concentrations. 51

Figure 3. 1 RCWA calculations showing (a) magnetic field distribution of the SOI guided mode resonance sensor; (b) electric field distribution of the photoresist grating-coupled PSi waveguide; and (c) electric field distribution of the all-PSi grating-coupled waveguide structure. Reflectance spectra of (d) SOI guided mode resonance sensor, (e) photoresist grating-coupled PSi waveguide, and (f) all-PSi grating-coupled waveguide structure before and after attaching a 0.8 nm thick monolayer of biomolecules. 57

Figure 3. 2 SEM image of the all-PSi gratings and the waveguide (cross-section)..... 59

Figure 3. 3 SEM images of (a) photoresist gratings on top of a PSi waveguide and (b) SOI waveguide with SiO_2 gratings. The image in (a) was taken at an angle of 30^o to the planar surface. The apparent non-planarity of the interface between the silicon waveguide and SiO_2 substrate layer in (b) is an artifact due to the sample cleavage. 60

Figure 3. 4 (a) Measured and (b) calculated angle-resolved reflectance spectra at 1550 nm (TE) for all-PSi grating-coupled waveguide after oxidation (solid line) and after 3-APTES attachment (dashed line).63

Figure 3. 5 (a) Reflectance spectra of all-PSi grating-coupled waveguide after oxidation and attachment of 3-APTES, Sulfo-SMCC, 16-mer probe DNA (50 µM) and complimentary PNA (50 µM). (b) Resonance shifts of all-PSi grating-coupled waveguides functionalized with 16-base probe DNA (50 µM) after exposure to complimentary PNA (50 µM), mismatch PNA (50 µM) and HEPES buffer. 64

Figure 3. 6 Detection sensitivity estimation for all-PSi grating-coupled waveguide sensor based on resonance angle shifts due to exposure of sensor to different complementary PNA concentrations. The 16-mer probe DNA concentration for all samples represented in the figure is 100 µM. The typical sample-to-sample variation in the resonance angle for each data point is ±0.1°..... 66

Figure 3.7 Top view (a) and cross-sectional (b) SEM images of PSi gratings and waveguide fabricated using the DIPS technique. The pores in the stamped regions are partially occluded compared to the unstamped regions. 70

Figure 3.8 (a) Measured PSi waveguide losses as a function of oxidation time at 500^{o}C. Curve fits are provided as a guide for the eye. Insertion is a digital image of the light scattering. (b) 3-layer and 2-layer PSi waveguide electric field distributions. 72

Figure 3.9 Stamped grating-coupled PSi waveguide reflectance spectra after oxidation and attachment of 3-APTES, Sulfo-SMCC, probe DNA, and complementary PNA molecules. 74

Figure 4. 1 Design of the PDMS flow cell integrated biosensor. (a) A schematic of the two components: the bottom is the PSi (light grey round area) with grating couplers (orange rectangular area); the top is the PDMS flow cell. (b) A picture of the fabricated device. (c) PSi waveguide integrated with the flow cell geometry used for Equation (4.1)~(4.6). (d) A single pore cross-section geometry (axially symmetric) used for finite element simulations with COMSOL. 79

Figure 4. 2 (a) Resonance angle positions during the injections of 0%, 1%, 2%, 3%, 5%, 7.5% and 10% NaCl solutions. The blue circles are experimental data, and the red lines are the average value of each concentration and drawn as visual guides. (b) The relation between NaCl concentrations and resonance angle shifts with a linear fit shown. The typical variation in the resonance angle shift for each data point is ± 0.005°. 84

Figure 4. 3 (a) Resonance angle shifts of integrated PSi waveguide biosensor during the injection of 3-APTES. The fitted curve is shown for visual guidance. (b) Time dependent change of 3-APTES surface coverage upon binding to a flat silicon surface. 87

Figure 4. 4 Experimental (blue circle) and COMSOL simulated (red line) normalized resonance angle changes during (a) 3-APTES, (b) Sulfo-SMCC, (c) probe DNA and (d) antisense PNA binding. 89

Figure 5.1 Schematic of BSW biosensor with a grating coupler. 95

Figure 5.2 Schematic of PDMS flow cell integrated PSi membrane waveguide biosensor with a grating coupler. 96

Figure 5.3 Schematic of an ideal portable biosensor based on PSi waveguide with a grating coupler structure. 97

CHAPTER I

INTRODUCTION

1.1 Introduction to biosensing

Human beings have many senses to recognize the surrounding environment. In addition to the traditionally recognized five senses of sight, hearing, taste, smell, and touch, other qualities including pain, balance, and acceleration also help us to interact with the world. For the detection and identification of small biomolecules, however, it is hard to simply use human senses without any additional physical aids. Therefore, special tools and techniques are required that comprise biosensing technology.

Biosensing technologies are devices or systems (biosensors) used for identifying, monitoring and controlling biological phenomena [1]. Generally, a biosensor consists of a biological recognition element (e.g., enzyme, antibody, DNA, microorganism) and a transducer that translates the interaction of the biological analyte with the recognition element into a measurable signal by means of electrical, optical, mechanical or thermal technologies [2]. Biosensors are usually classified into various groups either by the type of bio-recognition element utilized (e.g., enzyme biosensors, DNA biosensors) or by the type of transducer employed (e.g., electrochemical biosensors, optical biosensors). Both components of the biosensor, namely, the bio-recognition element and transduction platform play an important role in the construction of a sensitive and

selective device for identifying and detecting the analyte of interest [3]. Among the many types of biosensors, optical biosensors have attracted a great deal of attention since they are among the most sensitive, are immune to electromagnetic interference, and are amenable to multiplexed detection within a single device. Furthermore, nanoscale materials and modern nanofabrication technology have enabled smaller and cheaper optical biosensors to be realized and commercialized.

Since the first label-free optical biosensor was commercialized in 1990 [4], the classification of labeled and label-free biosensors has been widely accepted. Labeled biosensors rely on the attachment of special “labels” to one or more of the molecules/viruses/cells being studied in order to provide a means of detecting these species. Label-free biosensing technologies do not require such specialized sample preparation. A label is designed to be easily measured by its color, fluorescence, or other distinctive property to indirectly indicate the presence of the analyte to which it has been attached [5]. Unfortunately, labels invariably affect the binding kinetics of interaction by modifying the structure of binding partners. Consequently, there has been a strong drive to realize label-free biosensors. A great number of current label-free biosensors utilize optical transduction approaches [6], such as surface plasmon resonance (SPR) based biosensors [7-10], interferometer-based biosensors (Mach-Zehnder interferometer [11-13], Young’s interferometer [14-16], Hartman interferometer [17], backscattering interferometry [18-20]), optical waveguide-based biosensors (resonant mirror [21-23], metal clad waveguide or metal clad leaky waveguide

[24-26]), optical ring resonator based biosensors [27-30], optical fiber based biosensors [31-33], and photonic crystal based sensors [34-36]. The common ground of these biosensors is that they all utilize the optical refractive index change as the sensing transducer signal to monitor biomolecule interactions. Other methods, such as acoustic [37] and calorimetric [38] techniques, can also be applied in biosensors. This thesis will focus on label-free optical biosensors.

1.2 Introduction to porous silicon

1.2.1 Porous silicon background

Porous silicon (PSi) is a crystalline form of silicon with nanoscale void spaces introduced into its microstructure. It was first discovered by A. Uhlir [39] in 1956, but did not initially receive much attention. Sixteen years after its discovery, Nippon Telegraph and Telephone Public Corporation (Tokyo, JA) patented oxidized PSi for use as dielectric isolation components [40]. For the next two decades, PSi remained a relatively obscure material that was occasionally considered for its function as an isolator in integrated circuits [41-43]. As shown in Figure 1.1 [44], a noticeable increase in interest in PSi occurred after 1990, when L. T. Canham demonstrated visible photo-luminescence at room temperature [45]. Electroluminescence of PSi was demonstrated in 1992 by N. Koshida and H. Koyama [46], and PSi based light-emitting diodes (LEDs), switches and photodetectors gained significant attention through the 1990s [47-49]. In the late 1990's, PSi began to serve as a host material in some

biochemistry sensors [18]. As interest in PSi as a visible light source waned due to a lack of significant improvement in efficiency, research efforts into PSi for chemical and biological sensing began to rapidly increase. Biochemistry applications of PSi continue to be one of the major research focuses in the PSi community.

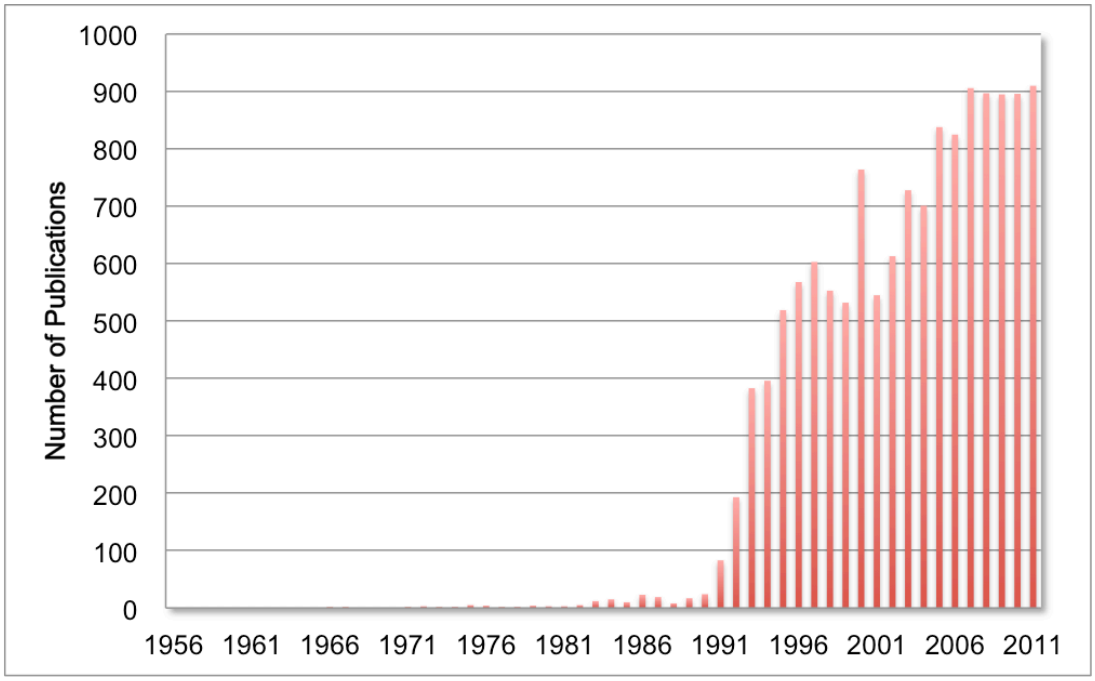

Figure 1. 1 Number of publications per year regarding PSi [44].

1.2.2 PSi biosensors

In the development of a biosensor, sensitivity attracts a great deal of concern and research effort. A typical recognition element in a label-free biosensor consists of a substrate, chemical linking molecules, and receptor molecules (e.g. antibodies, DNA) that are designed to bind to only one type of target molecule. The presence of a particular analyte is therefore detected by

measuring the binding between the analyte and the surface-bound receptors. For small molecule detection, the sensitivity of a biosensor is often limited by the number of receptor molecules attached to the sensor and available to capture target molecules. As a host material for sensing, PSi has the advantage of a large internal surface area (>100 m^2/cm^3) [50], which leads to improved capabilities for detecting small molecules.

Many types of PSi-based transducers have been applied to biosensors to monitor the refractive index changes upon a specific bio-recognition event, providing a simple yet effective label-free detection mechanism[51]. The four primary structures utilized for PSi sensors are the single-layer [18], double-layer (waveguide) [52], multi-layer [53], and microcavity [54]. As shown in Table 1.1 (adapted from [55]), the refractive index of the low porosity PSi layer (light grey) is n_h=1.8, while the refractive index of the high porosity PSi layer (dark grey) is n_l=1.2. Light illumination of PSi films of several micrometer thickness results in reflection from the PSi-PSi and the PSi-crystalline silicon interfaces, producing interference patterns (blue solid lines) for the single-layer, multi-layer and micro-cavity structures. For the double layer structure, a grating coupler is used to excite a waveguide mode for comparison. When biomolecules are introduced to PSi and affect the refractive indices of the films, these reflectance patterns will shift, and biomolecular information can be extracted. The red dashed lines in Table 1.1 give the reflectance of the various PSi structures after n_h and n_l are increased by 0.1, which represents biomolecule infiltration. Focusing on the features near 1200 nm wavelength, the multi-layer and micro-cavity both give

approximately 80 nm wavelength shift due to the refractive index increase, which is larger than that of single layer, only around 60 nm. The largest shift comes from the waveguide structure, about 115 nm. As will be discussed throughout the thesis, the resonant mode of the waveguide enables enhanced light-matter interaction, leading to a larger spectral shift and therefore higher biosensor sensitivity. Considering the sensitivity advantage as well as minimizing the challenges of infiltrating biomolecules into deep structures, the waveguide structure is highly desirable in biosensing applications. Therefore, in this thesis, attention is focused on PSi waveguide sensors.

Table 1. 1 Different PSi structures and their corresponding reflectance spectra before (blue) and after (red) an increase in refractive index of all layers by 0.1: single layer, double-layer waveguide, multilayer, and microcavity.

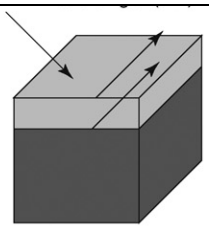 Single-layer (n=1.8, h=2 μm)	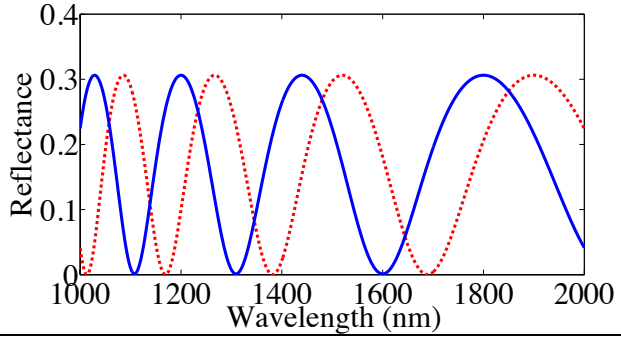
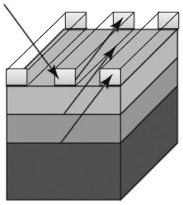 Double-layer (waveguide) (n_h=1.8, h_h=340 nm, n_l=1.2, h_l=1.5 μm)	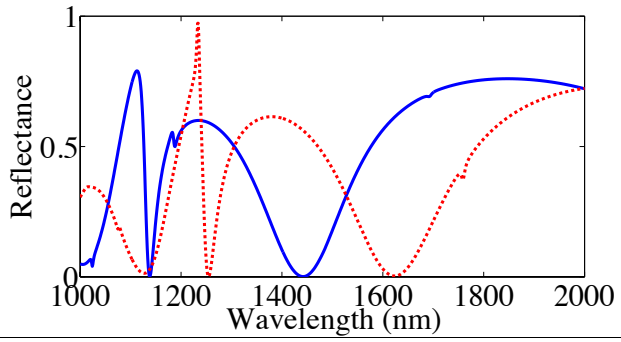
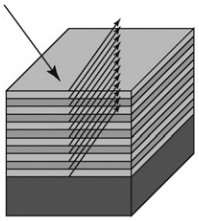 Multi-layer (n_h=1.8, h_h=180 nm, n_l=1.2, h_l=270 nm, 10 periods)	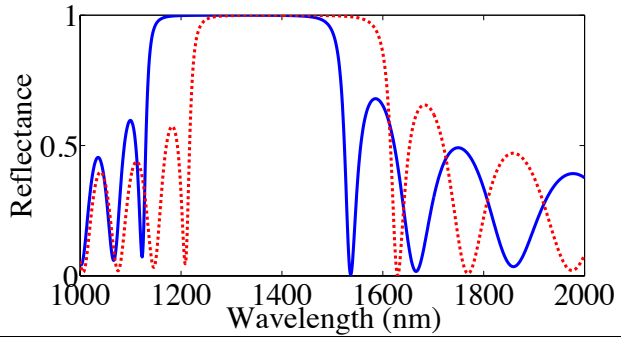
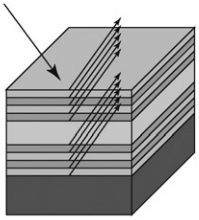 Microcavity (n_h=1.8, h_h=180 nm, n_l=1.2, h_l=270 nm, active layer thickness h_a= 1.44 μm, 5 periods on each side)	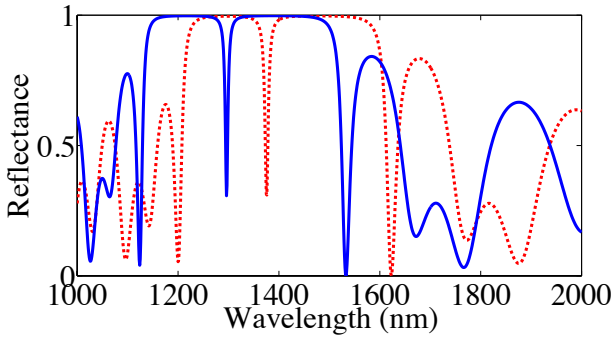

Similar to the evolution of basic PSi research, PSi waveguides first appeared for optoelectronics applications [56-59] before being recognized for their potential in sensing. The relatively large scattering loss in PSi waveguides (7-20 dB cm^{-1}) [60] does not significantly inhibit the sensitivity of the waveguides for detection of gases, liquids, and biomolecules. In 1998, PSi waveguides were first studied for sensing applications. H. F. Arrand et al. used a porous silicon waveguide to detect various solvents based on the degree of waveguide loss reduction when the pores of PSi waveguides were filled with different liquids [61, 62]. P. Rivolo et al. constructed a PSi waveguide gas sensor by means of absorption measurements [63]. P. Pirasteh et al. continued this research and focused on surface optical scattering measurements [64]. In 2005, J. J. Saarinen et al. demonstrated a detailed theoretical analysis on a prism coupled PSi waveguide structure for biosensing application [65], and the first experimental demonstration of these PSi waveguides for biomolecule detection came in 2006 [52, 66-68]. In 2007, K. Awazu et al. utilized the surface plasmon resonance technique to interrogate gold-cladded porous silica waveguides, and found a nine times larger resonance shift compared to bulk waveguides [69]. A label-free PSi membrane waveguide biosensor, introduced by G. Rong et al. in 2008 [70, 71], used a polymer film and air as cladding layers. In 2012, J. Xia et al. first combined a nanoporous silicon ridge waveguide with a Mach-Zehnder interferometer to form a highly sensitive optical sensor [72].

1.2.3 Formation mechanism of PSi

The type of PSi described in this work is fabricated by electrochemical etching of silicon in a hydrofluoric acid based electrolyte. It is the most commonly used method of fabricating PSi and is usually conducted in the dark to prevent photogenerated currents from contributing to the formation process [73, 74]. The exact formation process of PSi is still under debate. A number of theories have been proposed on the formation mechanisms and morphologies of PSi. Figure 1.2 shows the progress in the development of theories on formation mechanisms of PSi. In the early 1990s, Lehmann and Gösele proposed the quantum wire effect to explain pore formation on p-type silicon [75]. Figure 1.3 illustrates this chemical dissolution mechanism, which is recognized as the main mechanism during the PSi formation [76].

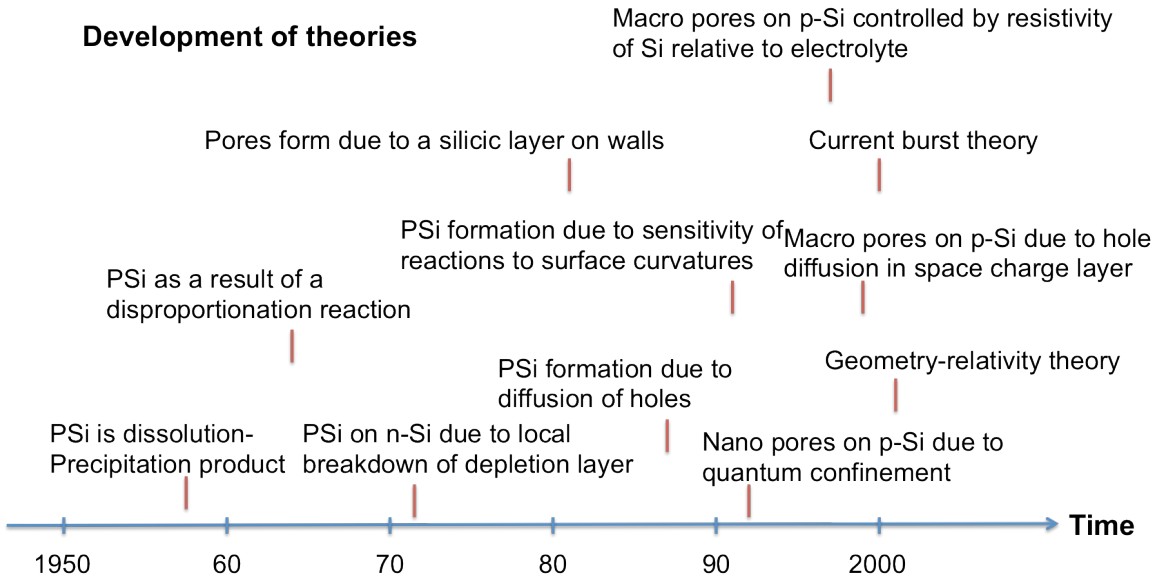

Figure 1. 2 Progress in the development of theories on formation mechanisms of PSi (adapted from [77], reproduced by permission of ECS – The Electrochemical Society).

In the Lehmann and Gösele theory, the silicon/HF solution interface behaves like a Schottky contact [78]. Figure 1.4 (a) shows the band diagram of the p-type Si/PSi/HF electrolyte solution interface under current flow. Hole transfer occurs at the bottom of the valence band (VB) edge, which is physically at the PSi/Si interface (pore tips, Figure 1.4 (b)) [79]. The pore walls are depleted of the holes necessary for the dissolution, which inhibits lateral etching of the pores and maintains pore directionality. In the p-type Si, the bandgap of PSi opens by quantum confinement effects [75].

The resulting characteristics of the PSi layer, including the average pore width, porosity, pore orientation, and layer thickness, depend upon the fabrication conditions used, including the substrate doping and type, the hydrofluoric acid concentration, the anodization current density and anodization time [73, 76, 80]. PSi can have pore sizes ranging from a few nanometers to several microns, as primarily dictated by the silicon substrate doping and space charge region that forms during the etching process [81]. In this work, PSi of ~10 nm-radius pore size is used. For a specific hydrofluoric acid concentration, the porosity, which determines the refractive index of the PSi layer, is proportional to the current density [82]. Varying the current density is a convenient way to form PSi layers with different refractive indices. Consecutive PSi layers can also be fabricated [83, 84]. Changing the current density does not affect the layer previously formed because silicon dissolution occurs preferentially at the silicon-electrolyte interface. The pore orientation tends to follow the <100> direction in the crystalline silicon

substrate. Additionally, the thickness of each layer can be precisely controlled by the etching time for a given applied current density.

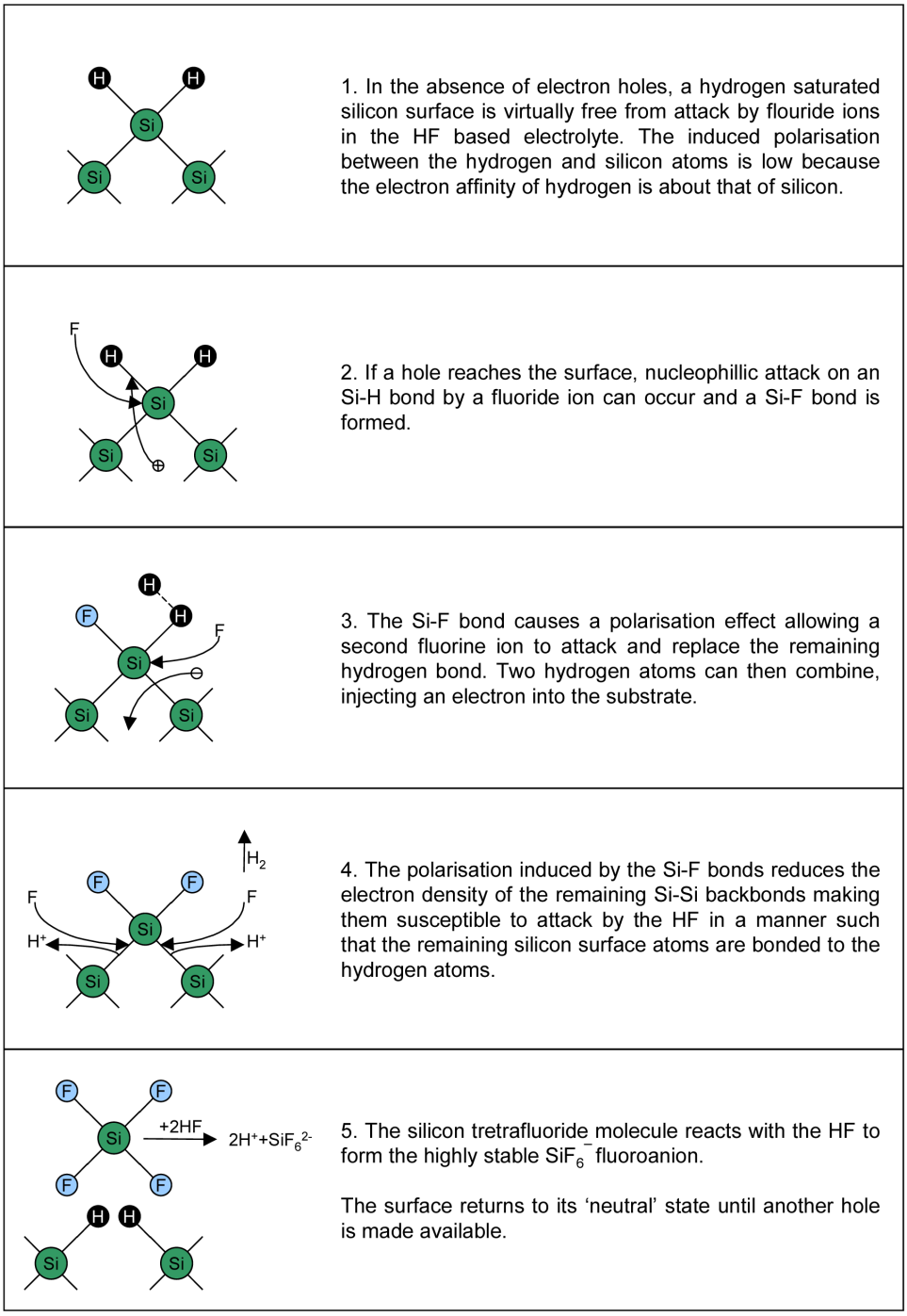

Figure 1. 3 Mechanism of PSi formation on p-type silicon [85].

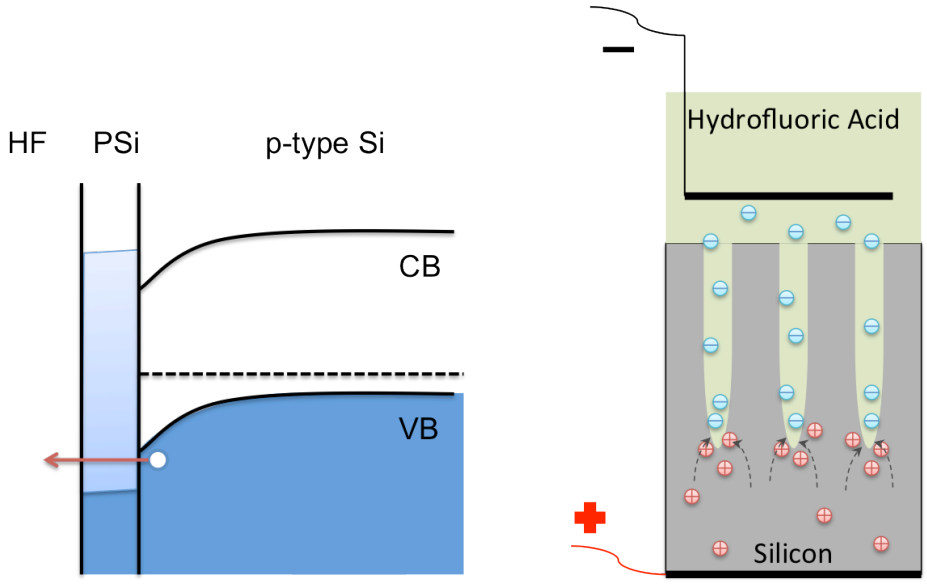

Figure 1. 4 (a) Band diagram of the p-Si/PSi/HF solution interface under current flow. (b) Schematic of the PSi etching cell.

1.3 Waveguide coupler structure

1.3.1 Waveguide

A simple planar waveguide is shown in Figure 1.5. It consists of a high-index dielectric layer surrounded on either side by lower-index material. The refractive index of the waveguiding film, n_f, must be larger than that of the cover material, n_c, and the substrate material, n_s, in order for total internal reflection to occur at each interface and for light to remain confined in the waveguide film layer [86]. A waveguide structure can support only a discrete number of guided modes based on the thickness and refractive index of each layer of the waveguide [87]. For example, a single-mode waveguide has only a single guided

mode per polarization direction (transverse electric (TE), or transverse magnetic (TM)). Figure 1.6(a) shows a ray depiction of three allowed modes in a waveguide. Each ray has a different direction within the film layers of the waveguide and each ray has a different effective refractive index. Figure 1.6(b) gives the three corresponding TE mode field patterns of the waveguide.

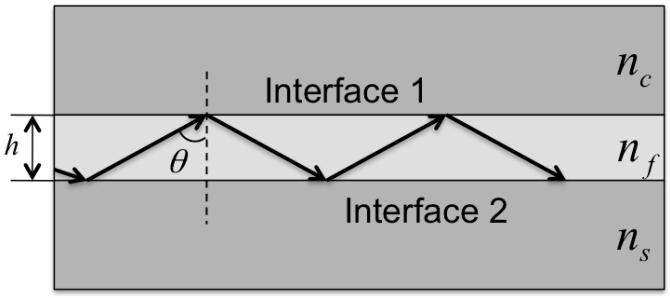

Figure 1. 5 Waveguiding in a simple planar waveguide.

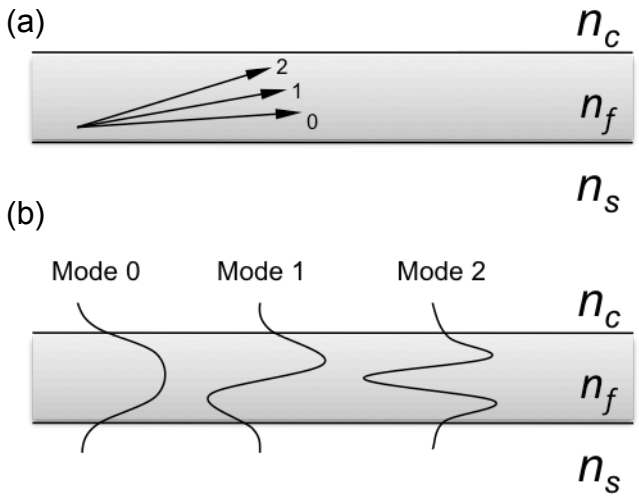

Figure 1. 6 (a) Ray depiction of three allowed modes in a waveguide. (b) Three TE modal field patterns of the waveguide.

To avoid decay of energy due to destructive interference as the wave travels through the waveguide, the total phase change for a point on the wavefront that travels from one interface to the next, and back again, must be a multiple of 2π [88]. For a wave incident at angle θ (Figure 1.5), the transverse resonance condition requires that

$$2kn_f h\cos\theta - 2\Phi_c - 2\Phi_s = 2m\pi \tag{1.1}$$

where k is the wavevector in the vacuum, h is the thickness of the film, n_f is the refractive index of the film, and m is an integer. A phase shift of $kn_fh\cos\theta$ is accumulated on the first transverse passage through the film. A phase shift of $-2\Phi_c$ occurs at the film-cover interface. Another $kn_fh\cos\theta$ is accumulated travelling back down, and finally there is a $-2\Phi_s$ phase shift at the film-substrate interface. A. Bruyant et al. demonstrated the first near-field observation of light propagation in a planar PSi waveguide close to the site of light injection, which clearly illustrates the phenomenon of light confinement in waveguide (see Figure 1.7) [89]. In the cover medium and substrate, the field is an evanescent wave. The amplitude decays exponentially with increasing distance from the interface between the waveguiding film and cover or substrate. Based on the exponentially decaying field outside the waveguide film, simple planar waveguides with air as the cover material can be utilized as sensors [90]. Analyte in the cover region interacts with the evanescent field of the waveguide mode, causing a change in the effective index of the mode that can be measured by a variety of optical methods. PSi waveguide sensors have the advantage of allowing analyte to

penetrate into the waveguide layer, allowing the analyte to interact with the majority of the optical field that is localized primarily in the waveguiding layer.

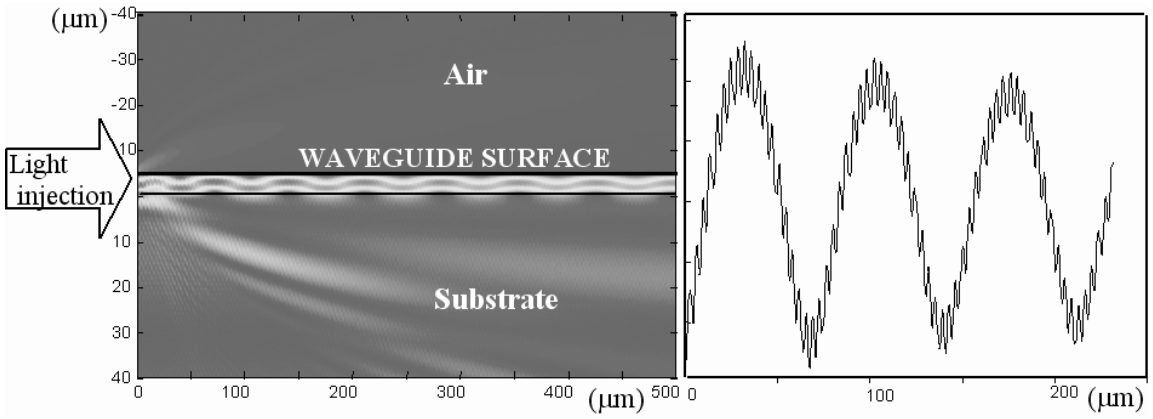

Figure 1. 7 Left: Simulation of the light propagation in a planar PSi waveguide close to the site of light injection. Light is confined in the waveguiding film layer and exponentially decays into the air and the substrate. Right: Intensity profile along the surface. [89]

1.3.2 Coupling methods

Based on the principle of reversibility of light, since light propagating in a waveguide is confined to the waveguiding layer, guided modes of a slab waveguide cannot be directly excited by light incident from the cover or substrate. For light to couple into a waveguide, it is necessary that both the energy of the light and the component of the wavevector along the propagation direction must be identical. Thus, light may be injected from the side into the waveguiding layer such as butt coupling or end-fire coupling. Alternatively a coupling element may be used to couple light into the waveguide via an evanescent wave, such as a prism coupler or grating coupler [91].

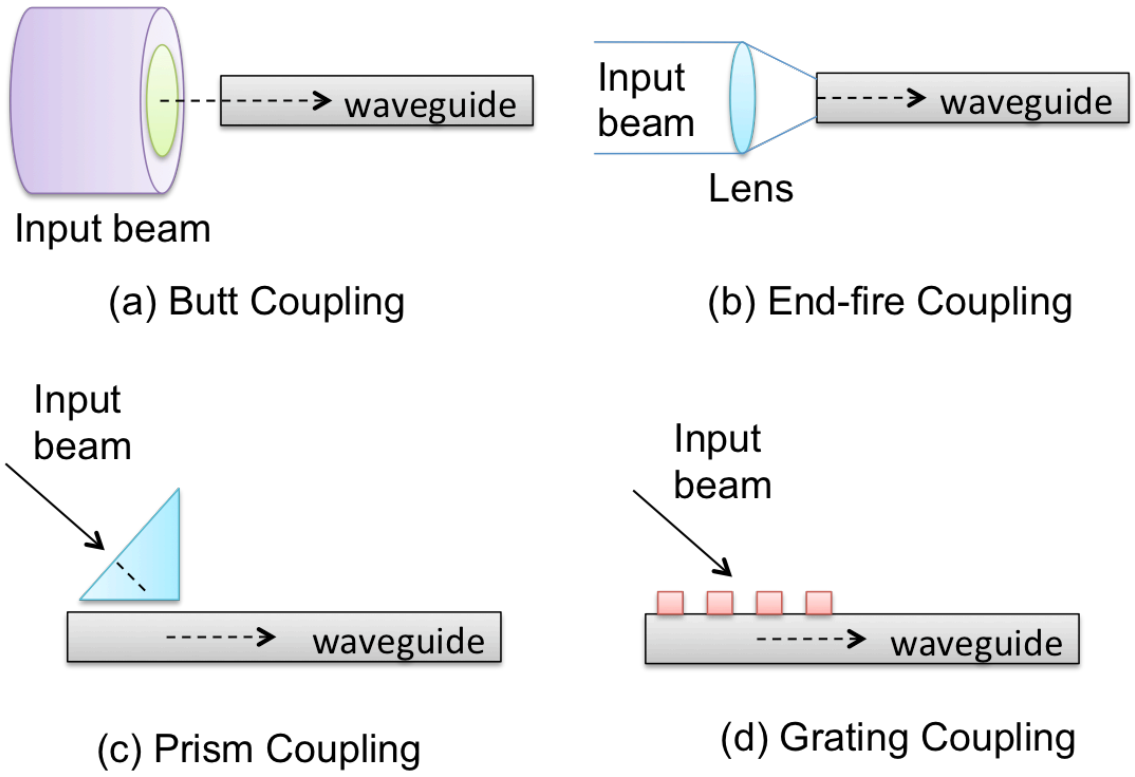

Figure 1. 8 Four techniques for coupling light into optical waveguides.

1) Butt coupling and end-fire coupling

Butt coupling (Figure 1.8 (a)) and end-fire coupling (Figure 1.8 (b)) both utilize injection of a light beam into one end of the waveguide. The difference between the two techniques is that end-fire coupling uses a lens to focus light into the waveguide while butt coupling injects light into the waveguide directly from another waveguide, fiber, or light source. Many elements affect coupling efficiency: (1) how well the fields of the excitation and the waveguide modes match; (2) the degree of reflection from the waveguide facet; (3) the quality of the waveguide end face; (4) the spatial misalignment of the excitation and waveguide fields; (5) the numerical aperture mismatch in which the input angles of the

optical waveguide are not well matched to the range of excitation angles; and (6) the match of polarization. Efficient coupling of light into the waveguide requires fine adjustment of the relative positions of beam and waveguide as well as matching of the intensity profiles of both light beam and waveguide. Both of these two coupling methods can be time-consuming and experimentally challenging for high efficiency coupling. They are mostly used in optical circuits and optic fiber coupling [92, 93].

2) Prism coupling

The prism coupler (Figure 1.8 (c)) is commonly used for coupling light into or out of a planar optical waveguide. It was first introduced in 1969 [94]. The prism is placed above the thin-film waveguide and is separated from it by a small air gap of low refractive index (Figure 1.9). A light beam is directed through a side of the prism, and normally reflected back out the opposite side. In the vicinity of the waveguide the overlapping incident and reflected beam generate a standing wave. The evanescent field of that standing wave penetrates into the waveguide. However, at certain values of the incident angle and if the phase match conditions are fulfilled, the light does not reflect back out. The evanescent field stimulates a mode that is guided by the waveguide, resulting that the incident light is transmitted through the prism base into the waveguide film. The phase matching condition can only be achieved when the refractive index of the prism is at least as high as the effective refractive index of the waveguide and the distance between the prism and the waveguide film is on the order of half a

wavelength because of the short propagation distance of the evanescent wave in the z-direction, as shown in Figure 1.9.

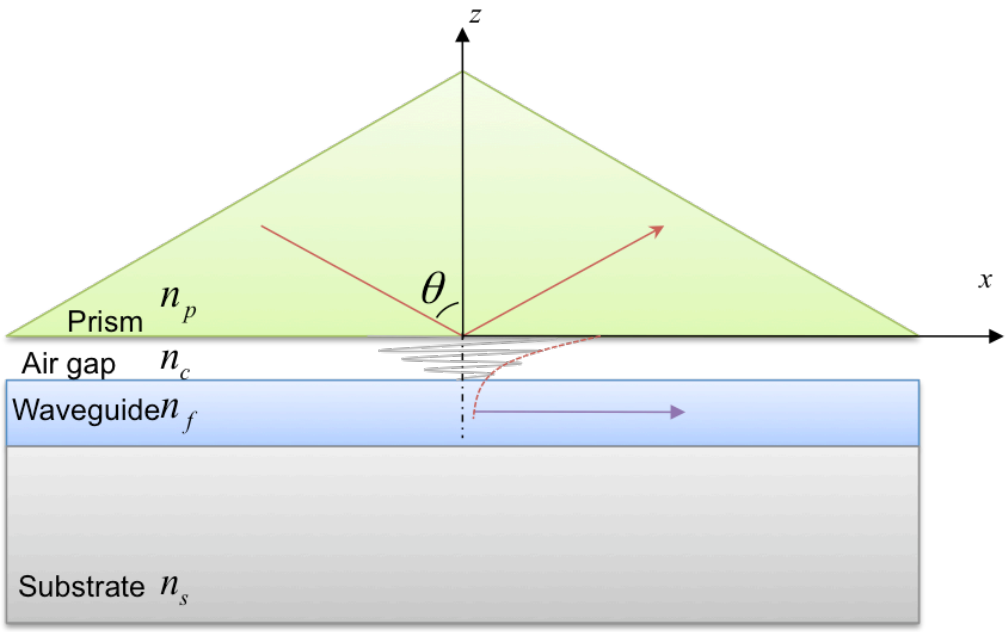

Figure 1. 9 Schematic of a prism coupler on a waveguide.

In order to understand the phenomenon of prism coupling, let us divide the wavevector of the incident light in the prism into components parallel (*x* direction) and normal (*z* direction) to the air gap. The *x*-component wavevector is $kn_p\sin\theta$, where $k=2\pi/\lambda$, λ is the wavelength, n_p is the refractive index of the prism, and θ is the incident angle. As we discussed in section 1.3.1, a thin waveguide film can support a number of guided modes. When the direction of the incident beam is such that the *x*-component wavevector, $kn_p\sin\theta$, is equal to the propagation constant of one of the waveguide film modes kn_{eff}, where n_{eff} is the effective refractive index of the waveguide film, coupling becomes efficient and optical

energy can be transferred from the prism to the waveguide film. Thus, the coupling condition for prism coupling is

$$n_{eff} = n_p \sin\theta \tag{1.2}$$

If there are multiple guided modes supported by the waveguide, then there will be a different coupling angle θ for each mode.

As early as 1973, R. Ulrich and R. Torge determined the refractive index and the thickness of a light-guiding thin film by a prism coupler [95]. In 1975, R. T. Kersten proved that the prism coupler could be used to measure refractive indices within an accuracy of $\Delta n < 10^{-3}$ [96]. The prism coupler has been used to determine the refractive index of PSi layers [97, 98], and it has been used as a primary element in PSi waveguide biosensors. However, the prism coupling approach usually requires a critical adjustment of the gap between the prism and the waveguide and there is always a possibility to damage the waveguide or the prism if the waveguide is pressed too hard against the prism. Also, coupling to high index waveguides requires the use of expensive and higher index prisms. Furthermore, the bulky nature of the prism makes it unsuitable for applications in integrated devices.

3) Grating coupling

Serving the same purpose as the prism coupler, a grating at the waveguide surface can also couple light into or out of the waveguide; however, it is by diffraction, not by the evanescent field. As shown in Figure 1.10, a laser beam incident on a grating at an angle θ has a phase variation in the *x* direction given by $\exp\left[i \cdot (2\pi / \lambda_c) \cdot (\sin\theta) \cdot x\right]$, where λ_c is the wavelength in the cover layer.

As the beam passes through the grating it undergoes an additional phase delay $\Delta\varphi \cdot \sin(2\pi x/\Lambda)$, where Δφ is the amplitude of the spatial phase modulation caused by the grating and is sometimes called the phase depth of the grating (here we assumed for convenience the phase modulation to be sinusoidal [99, 100]), and Λ is the grating periodicity (see the insertion of Figure 1.10). Thus, the light reaching the top surface of the waveguide film varies as $\exp\{i\cdot[\Delta\varphi\cdot\sin(2\pi x/\Lambda)+(2\pi/\lambda_c)\cdot(\sin\theta)\cdot x]\}$. In the simple derivation for an ideal case, we normalize the phase depth Δφ to be 1. Then, the polarized light can be treated as a superposition of many waves with individual phase variations $\exp\{i\cdot[m\cdot(2\pi/\Lambda)\cdot x+(2\pi/\lambda_c)\cdot(\sin\theta)\cdot x]\}$, where m is any integer [101]. The polarized light will couple most strongly to a film guided wave of the form $\exp[i\cdot(2\pi/\lambda_g)\cdot x]$, where λ_g is the wavelength of the guided wave. If one of the waves is phase matched to the guided wave, then the following condition applies,

$$\frac{2m\pi}{\Lambda}+\frac{2\pi}{\lambda_c}\sin\theta=\frac{2\pi}{\lambda_g}$$

where $\lambda_c=\lambda_0/n_c$, $\lambda_g=\lambda_0/n_{eff}$, and λ_0 is the vacuum wavelength. With $k_0=2\pi/\lambda_0$, we then find

$$k_0\cdot n_{eff}=m\cdot\frac{2\pi}{\Lambda}+k_0\cdot n_c\cdot\sin\theta \tag{1.3}$$

and at last, we get the well-known grating equation below.

$$n_{eff}=n_c\cdot\sin\theta+m\cdot\frac{\lambda_0}{\Lambda} \tag{1.4}$$

Equation 1.4 is the basic relationship for the grating coupler design, and a good approximation to calculate n_{eff} especially for the case of a relatively shallow

grating. However, in a real structure, many aspects of the grating should be considered, including the shape, fill factor, and refractive index, as each plays an important role in the light coupling.

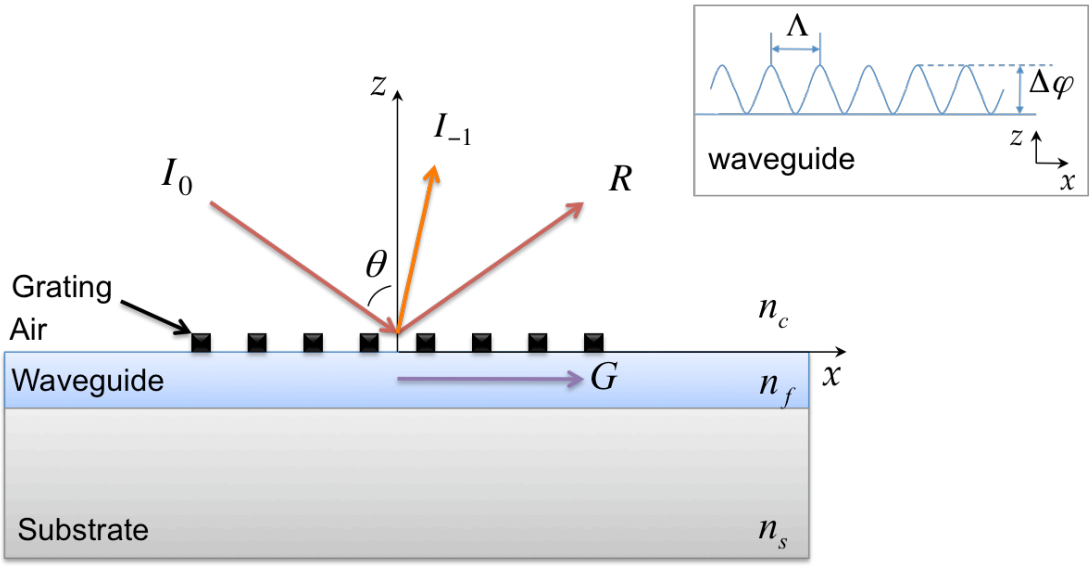

Figure 1. 10 Schematic of a grating coupler on a waveguide. The incident beam (I_0), reflected beam (R), first-order defracted beam (I_{-1}), and guided optical beam (G) are shown. Insertion: spatial phase modulation caused by the gratings.

As early as the 1960's, the potential for producing miniaturized optical integrated circuits on a single wafer, resistant to vibration and thermals effects, has raised the need for a simple and efficient means of coupling light into and out of thin film waveguides [94, 99]. The grating coupler was first proposed in 1970 starting with the work of Dakss [102]. Many varieties of grating couplers on various materials have, over the years, been designed and fabricated. Grating couplers have been etched on semiconductors [103] and dielectric waveguides [104] as well as onto polymeric waveguides [105]. However, no one previous to

the work described in this thesis has worked on a grating coupler in PSi. The advantage of the grating is that it is a simple, reproducible, and permanent coupler which is compatible with planar device technology. Furthermore, because it is open on the top of the gratings, the grating coupled PSi waveguide can be integrated with microfluidics to form a compact biosensor system.

1.4 Experimental instrument

The Metricon Model 2010/M Prism Coupler (Metricon Corp., USA) was used to monitor the angular interrogated reflectance in this work. Note that equivalently, a system could be used with a fixed angle and variable wavelength. Two schematics of the measurement configuration are shown in Figure 1.11. Measurements are taken by using a computer-driven rotary table which varies the incident angle. There are two modes that can be chosen: one is the regular prism coupler mode utilizing the prism coupling technique (Figure 1.11(a)); the other is the non-contact, variable-angle monochromatic fringe observation (VAMFO) mode (i.e., without a prism), which could be used to monitor the reflectance of the grating-coupled waveguides (Figure 1.11(b)). A 1550 nm diode laser was used as the light source. Light from the laser is incident on the waveguide at variable angle by rotating the stage, and the reflected light intensity is measured by an InGaAs photodetector.

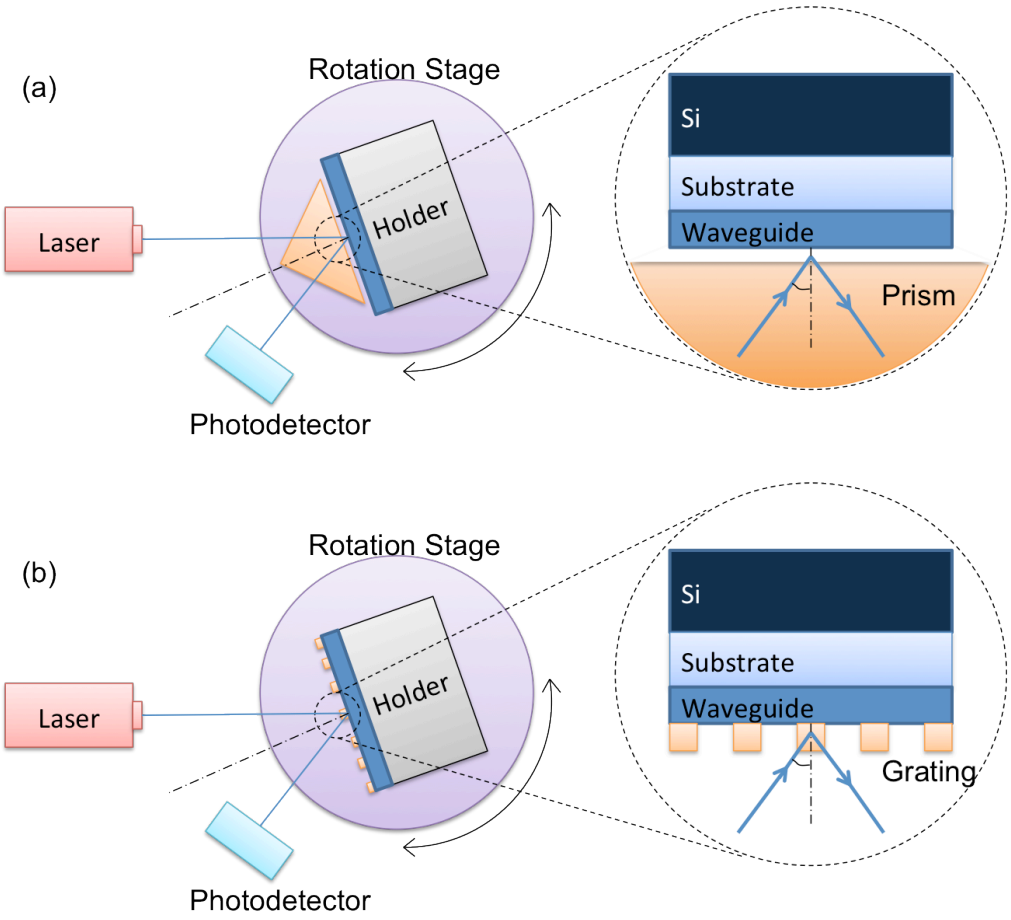

Figure 1. 11 Schematics of the measurement system of the Metricon Model 2010/M instrument: (a) the prism coupler mode; (b) the VAMFO mode.

1.5 Objective and overview of the dissertation

The two primary objectives of this dissertation are as follows:

1) Design and optimize grating-coupled PSi waveguide biosensors for small molecule detection.

2) Theoretically and experimentally characterize the sensor performance via both static and kinetic measurements and analysis.

This is the first time combining the benefits of both PSi and diffraction gratings for the detection of small molecules. The use of a grating coupler instead of a prism coupler allows the device to be more compact. The large surface area available for biomolecular attachment and strong field confinement in the waveguide region where biomolecules are immobilized make it possible to detect biomolecule interactions in PSi with high sensitivity. Chapter II will focus on a photoresist grating coupled-PSi waveguide structure, including the design, fabrication, characterization and small molecule sensing performance of the structure. It is the basic structure used for biosensor design. The experimental results will show that, the performance of the photoresist grating coupled PSi waveguide biosensor is satisfied and it could be used for small biomolecule detection. Chapter III will discuss an all-PSi grating-coupled waveguide biosensor which is improved from the photoresist grating-coupled PSi waveguide because it allows all regions of the PSi waveguide to be accessible for biomolecule infiltration. A rigorous comparison of the all-PSi grating coupled waveguide, photoresist grating-coupled PSi waveguide, and an SOI planar waveguide biosensor is presented. Both the theoretical simulation and experimental results certify that the all-PSi waveguide grating-coupled waveguide biosensor is a highly efficient biosensor and has the highest sensitivity of the aforementioned three grating-coupled waveguide biosensor designs. Chapter IV presents the design and fabrication of a fluidic-channel integrated all-PSi grating-coupled waveguide biosensor, which is feasible for near real-time sensing of liquids and DNA hybridization and analysis of kinetic parameters of molecules in nanoscale

pores. At last in Chapter V, conclusions and future research to improve sensor performance and expand the sensing applications of the PSi waveguide platform are suggested. General prospects for biosensor research is also discussed.

CHAPTER II

PHOTORESIST GRATING COUPLED PSI WAVEGUIDE BIOSENSOR

For more than two decades, gratings have been combined with waveguide structures to form biosensors because of their outstanding integrability and relatively high sensitivity detection of analytes [106-114]. Although these grating-coupled sensors have been demonstrated using a variety of different materials and different configurations, they all realize label-free detection by means of affecting the evanescent tail of a waveguide mode near the interface. When target analytes bind to surface-bound probe molecules, the effective refractive index of the media surrounding the waveguide is changed, resulting in a perturbation to the original waveguide mode. By monitoring this perturbation, molecular binding can be detected. The key disadvantage of this evanescent wave-based detection method is that typically >80% of the total optical power is contained within the waveguide and does not contribute to the surface attachment sensing [115]; the evanescent wave that interacts with molecules is an exponentially decaying field that only exists within a few hundred nanometers, or even tens of nanometers, of the waveguide interface [6]. Therefore, detection of small molecule binding, which causes only a small perturbation to the field distribution, is challenging for evanescent wave sensors and results in low detection sensitivity.

In this chapter, photoresist gratings are combined with PSi waveguides to form compact biosensors that can detect molecular binding events in a straightforward manner based on guided mode perturbations. The nanoscale void spaces in PSi allow molecules to be infiltrated directly into the core of the waveguide where they interact with a guided mode. The large internal surface area of PSi allows immobilization of more probe molecules compared to a flat surface, which increases the likelihood of capturing low concentration target molecules in a complex solution. However, approximately half of the available PSi internal surface area is blocked by the photoresist gratings.

2.1 Fabrication

2.1.1 PSi waveguide fabrication

Based on the electrochemical etching method introduced in chapter 1.2.2, a PSi waveguide structure is fabricated (Figure 2.1(a)) using the etching cell shown in Figure 2.1 (b) [116]. The PSi waveguide is fabricated by electrochemical etching of p+ (0.01Ω-cm) silicon wafers in a 15% ethanoic hydrofluoric acid electrolyte, which is composed of 175 mL 99% ethanol and 75 mL 49% aqueous HF. The waveguide consists of two thin PSi films: a top, low porosity (high refractive index) layer etched at 5 mA/cm^2 for 62 seconds and a bottom, high porosity (low refractive index) layer etched at 48 mA/cm^2 for 53 seconds. After anodization, the waveguides are soaked in 1.5 mM KOH for 30 minutes to widen the pores. The nominal thicknesses of the PSi waveguide

layers, as measured by scanning electron microscope (SEM), are as follows: 325 ± 20 nm top PSi layer and 1500 ± 20 nm bottom layer.

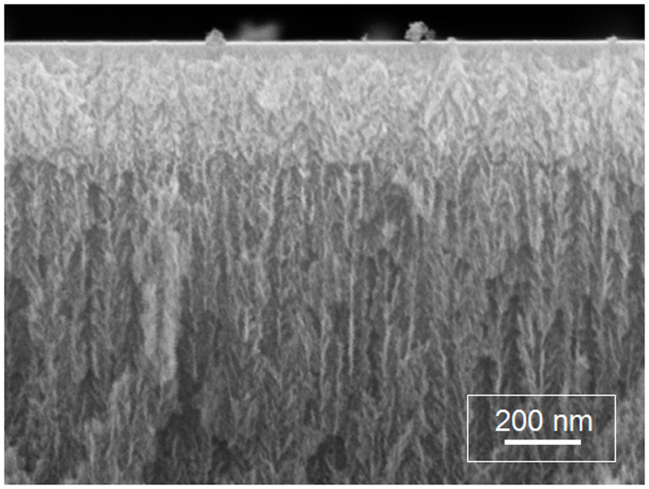

Figure 2. 1 Cross-section SEM image of two-layer porous silicon waveguides. The brighter regions are the nanoscale silicon matrix and the dark regions are void spaces.

2.1.2 Oxidation

In order to let biomolecules interact greatly with the strongly confined field in the PSi waveguide region, biomolecules must be immobilized within the pores. Several methods for immobilizing different kinds of biomolecules onto a silicon dioxide surface are available [117, 118]. Therefore, PSi waveguides need to be firstly oxidized in order to utilize these techniques. There is an optimal thickness of oxide to grow on the pore walls. Insufficient oxide will lead to incomplete attachment of biomolecules. Over-oxidation will compromise the refractive index contrast of the waveguide, which subsequently reduces the electric field confinement in the waveguide film layer and reduces the sensitivity of detecting

biomolecules in that layer. Oxidation can dramatically reduce refractive index of a PSi layer (n_{Si} = 3.4784 at 1550nm, n_{SiO2} = 1.45 at 1550nm) [119]. Figure 2.2 shows simulation results of varying the refractive index of the waveguide film layer n_f from 2.00 to 1.80. If the grating period is fixed, from Equation 1.4, a shift toward lower angles is expected. The calculation results show that the shift is about 12°. The field confinement of the waveguide is also reduced from 50.8% to 42.6% and the resonance broadens because the refractive index contrast between the cover layer and the waveguide film decreases. Hence, the minimum amount of oxidation that allows biomolecule attachment needs to be determined in order to achieve the best sensing performance. Other techniques exist for linking biomolecules to silicon without oxide [120, 121], but these methods were not pursued in this work.

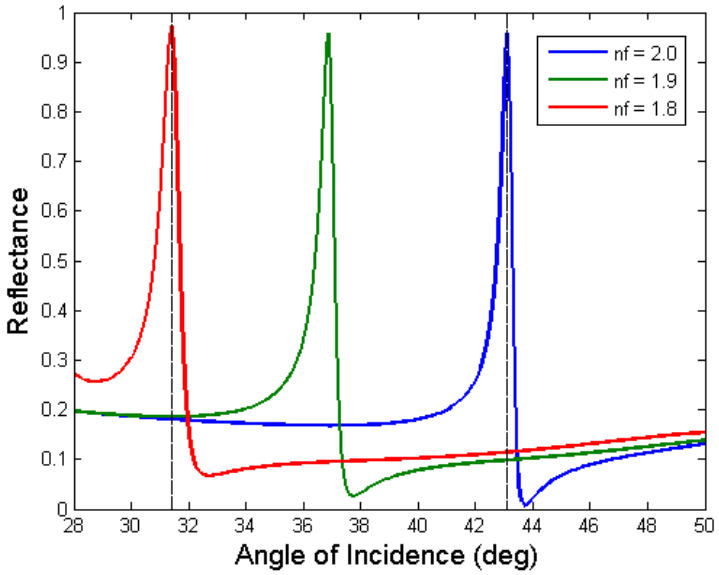

Figure 2. 2 Theoretical calculation of grating coupled PSi waveguide showing the waveguide resonance angle shift to smaller angles with a reduction in PSi refractive index associated with various levels of oxidation.

There are two major elements that can affect the oxidation rate: temperature and time. For bulk silicon, it is typical to heat the sample at 800^{o}C for tens to hundreds of minutes to create a 10-20 nm thin gate oxides for submicron devices [122]. For PSi waveguide sensors, it is not necessary to grow a thick insulating oxide layer. Only a thin SiO_2 film is needed for biomolecule attachment. Due to its distinct structure and morphology, PSi oxidizes at different rates compared to bulk silicon. Therefore, a series of oxidation testing experiments were conducted for PSi under different temperature and time conditions. For simplicity, single-layer PSi samples were used to test the oxidation conditions.

Single-layer PSi samples are fabricated by electrochemical etching of boron doped p+ silicon with a 0.01Ω·cm resistivity and <100> growth direction. The electrolyte is 15% hydrofluoric (HF) acid. The PSi layer is formed by applying 48 mA/cm^2 for 100 seconds. Then 100 μL of 1.5 mM KOH solution is dropped on the PSi to open the pores. After incubating for 30 min in KOH, washing the sample with ethanol, and drying with nitrogen, the sample is ready for oxidation. The thickness of the PSi layer is approximately 3 μm, and the porosity is about 88%.

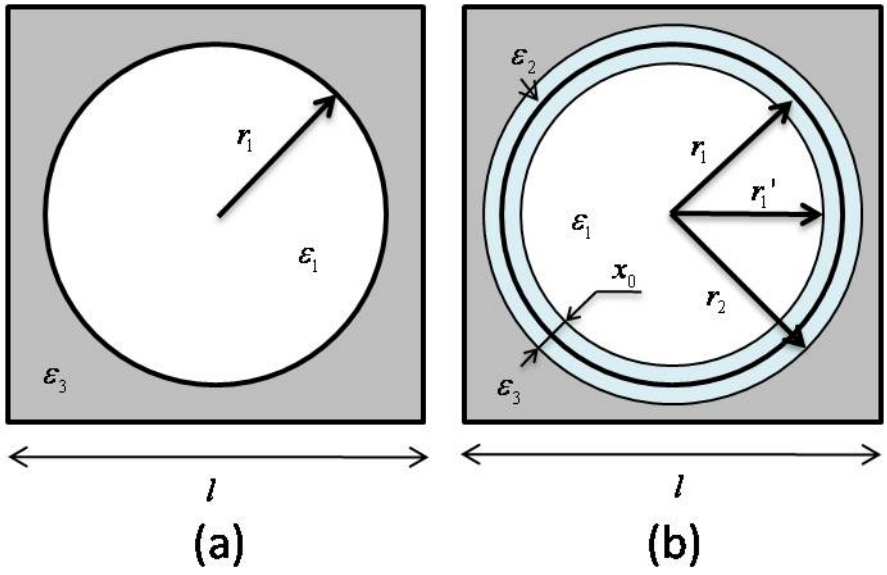

Figure 2. 3 Geometrical model for (a) as-anodized PSi, which includes air (ε_1) and silicon (ε_3); (b) model for oxidized PSi, which includes air (ε_1), SiO_2 (ε_2) and silicon (ε_3). [82]

J. E. Lugo introduced a simple model of PSi oxidation which is shown in Figure 2.3 [82]. PSi samples can be described as an array of infinite columnar holes of radius r_1 and dielectric function ε_1, with crystalline silicon as the host with a dielectric function ε_3 (Figure 2.3 (a)). After oxidation, we need to consider the silicon dioxide as a third component, between the columnar holes and the crystalline silicon, with a dielectric function ε_2 (Figure 2.3 (b)). The porosity (P) of the PSi samples without oxide is expressed based on Maxwell-Garnett theory as:

$$\frac{\varepsilon_{eff} - \varepsilon_3}{\varepsilon_{eff} + \varepsilon_3} = P\frac{\varepsilon_1 - \varepsilon_3}{\varepsilon_1 + \varepsilon_3} \tag{2.1}$$

where ε_{eff} is the effective dielectric function of unoxidized PSi as a mixture of two components.

Figure 2.3 (b) shows the three components of Lugo's oxidized PSi model. During the oxidation of silicon, the SiO_2 film will not be coplanar with the original silicon surface because a volume expansion occurs during oxidation. This expansion occurs because the density of SiO_2 is slightly less than the density of silicon. Growth of an oxide of thickness x_0 will consume a layer of silicon of about $0.45x_0$ thick. Taking into account this expansion, the initial porosity P, without oxide, is transformed in

$$P_{ox} = P[1 - 0.55X]^2 \tag{2.2}$$

where P_{ox} is the PSi porosity after oxidation, $X = \frac{x_0}{r_1}$ and x_0 is the oxide coating thickness.

For minimal oxidation, several samples are heated 5 min [123] at different temperatures using the following procedure: first, the oven is heated to a certain temperature, second, the sample is inserted, and third, after 5 min, the sample is removed from the oven. The refractive index of the PSi layer is measured before and after oxidation using the Metricon 2010 prism coupler. The change in refractive index of the PSi layer due to oxidation at each temperature is shown in Figure 2.4. At an oxidation temperature of 800°C, the refractive index shift is about 0.11 RIU. As the temperature is reduced, the refractive index shifts also are reduced. For 400°C - 600°C, the refractive index shifts are almost the same within the accuracy of the measurement, around 0.05 RIU, which is significantly smaller than at 800°C, as we expected. The weight change of the PSi layer due to oxidation in 400°C - 600°C is comparatively small, about 0.0005 dm/dT [124]. Therefore, its refractive index change is also not significant.

By using Lugo's model, we can calculate the porosity changes and the surface coating SiO_2 thickness x_0 with the assumption that the pore radius is 10nm. The results are shown in Figure 2.5 (a) and (b).

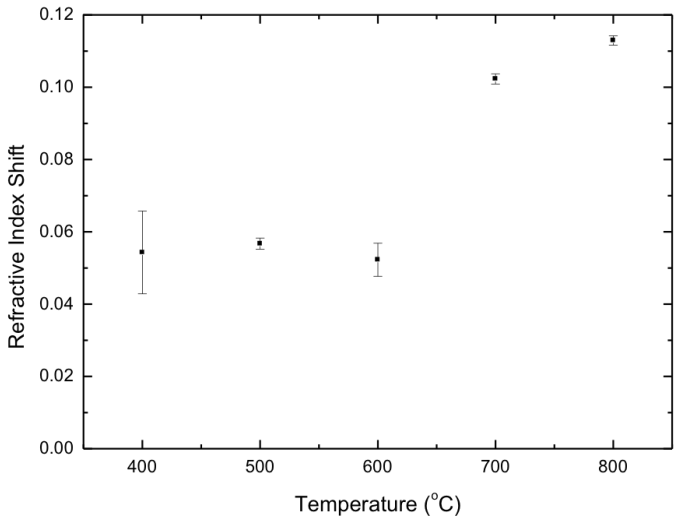

Figure 2. 4 Refractive index shifts of PSi single layer after oxidation at various temperatures for five minutes.

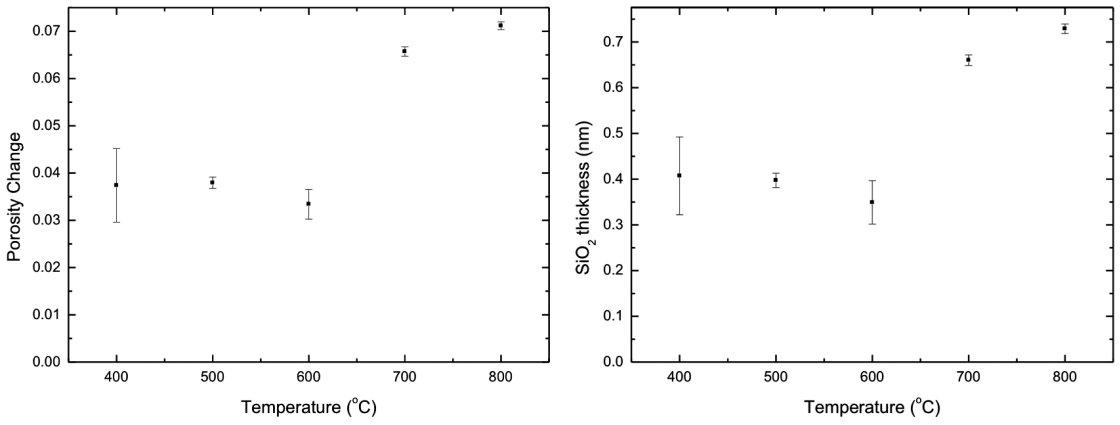

(a) (b)

Figure 2. 5 Change of PSi porosity (a) and SiO_2 thickness (b) after oxidation.

Since the purpose of oxidation is to attach biomolecules in the pores, the appropriate oxidation conditions must be selected only after attaching molecules in the oxidized pores. Hence, after oxidation, 3- aminopropyltriethoxysilane (3-APTES) is assembled on the SiO_2 surface in the pores. It contains an amino group which is commonly used in sensing applications to promote adhesion between silica substrates and organic materials. The details of the process will be discussed in the next section. Due to the infiltration of the 3-APTES molecules, the refractive index of the PSi layer is changed (Figure 2.6), and this variation demonstrates how much 3-APTES is linked to the SiO_2. In Figure 2.6, the refractive index change curve is saturated at about 0.035 for the 800^{o}C sample whose 3-APTES coverage is therefore assumed to be 100%. By a simple calculation, the 700^{o}C sample gives about 98% 3-APTES coverage, the 600^{o}C sample gives about 97% coverage, and 500^{o}C sample gives 85% coverage. For the 400^{o}C sample, the coverage is comparatively low, only about 43%. T. Unagami examined the oxidation process of PSi by infrared spectroscopy [123]. He demonstrated that the PSi layer could be oxidized at such low temperature as 200^{o}C. However, at temperatures below 400^{o}C, Si_2O_3, as well as SiO_2, is produced by the oxidation. Only SiO_2 is formed by oxidation at temperatures above 500^{o}C. Therefore, for the 400^{o}C sample, the small shift may be due in part to insufficiently oxidized PSi since no reports in the literature describe stable 3-APTES attachment to Si_2O_3. Compared with the 3-APTES saturation shift, 500^{o}C is a reasonable temperature which gives enough oxidation

for biomolecular attachment but will enable a maximally high index contrast between the two layers of the PSi waveguide.

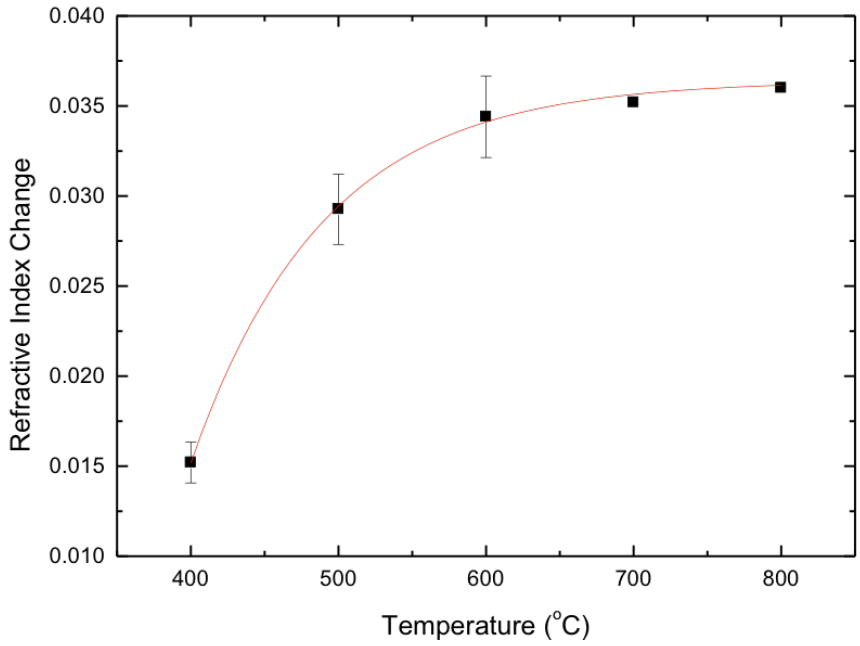

Figure 2. 6 Refractive index change of PSi layer due to 3-APTES attachment at different oxidation temperatures. Saturation of the refractive index shift is expected when 3-APTES monolayer coverage in the pores is complete.

2.1.3 Fabrication of photoresist grating coupled PSi waveguide

1) Design of grating period

A resonant feature in the angle resolved spectra can be observed when the light is coupled into a guided mode and in particular when the mode wave vector satisfies the grating relation (Equation 1.3) derived in section 1.3. Let us rewrite it here:

$$k_0 \cdot n_{eff} = m \cdot \frac{2\pi}{\Lambda} + k_0 \cdot n_c \cdot \sin\theta_g \qquad (2.3)$$

where k_0 is the wave number in vacuum, n_{eff} is effective refractive index of the waveguide, m is an integer, Λ is the grating period, n_c is the external medium refractive index, and θ_g is the resonance angle of incidence of the grating coupler. Here, the external medium is air, so n_c=1. Assuming that the first-order of diffraction (m=1) is used to couple light into the waveguide, and substituting in an expression for the wave number k_0 by $k_0=2\pi/\lambda_0$, the equation can be simplified as

$$\frac{2\pi}{\lambda_0} \cdot n_{eff} = 1 \cdot \frac{2\pi}{\Lambda} + \frac{2\pi}{\lambda_0} \cdot \sin\theta_g \tag{2.4}$$

A critical parameter is the grating period Λ, which provides the incident beam its momentum for coupling to the waveguide mode. Solving the above equation for the grating period gives

$$\Lambda = \frac{\lambda_0}{n_{eff} - \sin\theta_g} \tag{2.5}$$

Due to slight variations that occur during the fabrication process, the n_{eff} of each PSi waveguide may be slightly different even though the same electrochemical etching parameters are used. In order to maintain the resonance angle θ into a strict region, the n_{eff} must be measured for each sample to determine an appropriate grating period Λ. The value of n_{eff} for each sample can be evaluated in a straightforward manner by performing a prism-coupler measurement before grating fabrication according to the relation in section 1.3

$$n_{eff} = n_p \sin\theta_p \tag{2.6}$$

where n_p is the prism refractive index at λ_0 and θ_p is the internal incident angle of the prism coupler that corresponds to a resonance condition. Thus:

$$\Lambda = \frac{\lambda_0}{n_p \sin\theta_p - \sin\theta_g} \tag{2.7}$$

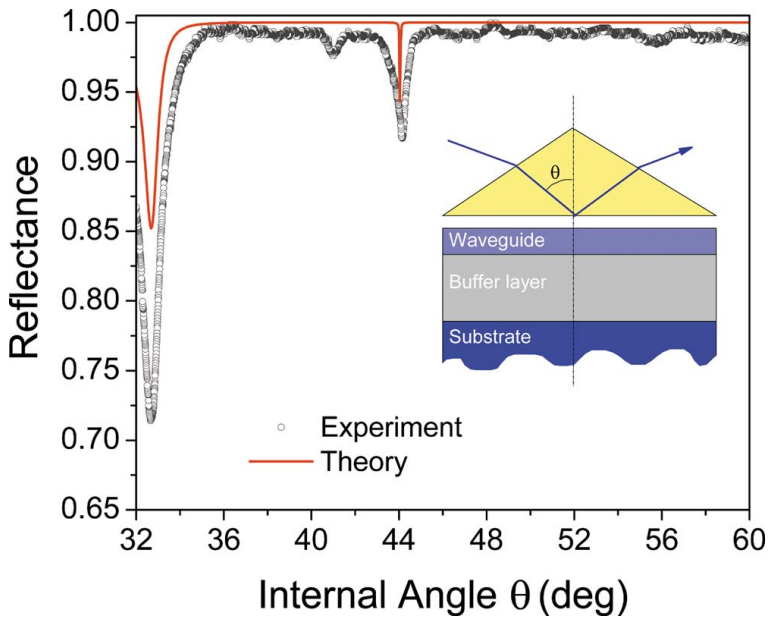

Figure 2.7 Experimental and theoretical values for the reflectance of one PSi waveguide sample [125].

In Figure 2.7, a typical angle-resolved attenuated total reflectance measurement is presented. It was obtained by means of a Metricon 2010/M prism coupler mode, with a cubic zirconia prism n_p=2.1252, in the Otto configuration (see inset) for Transverse Electric (TE) polarized incident light at the wavelength λ_0 =1550 nm. The prism is placed above the structure a few hundred nanometers from the waveguide surface. For incident angles above the critical angle, the light is entirely reflected at the prism base unless it satisfies the condition given in Equation 2.6 and is coupled through the air gap into the waveguide. The coupled light can be absorbed, scattered, or even transmitted

through the lower PSi substrate layer into the bulk silicon; thus, for each guided mode, a dip in the reflectance is observed. In particular, the spectrum in Figure 2.7 presents a structure that corresponds to the fundamental TE waveguide mode at about 44°. The effective index of the mode is found to be n_{eff} =1.4763, according to Equation 2.6. The width of the dip is determined by the overall mode losses; they depend on the distance between the prism and the waveguide, the substrate layer thickness, as well as absorption and scattering within the PSi.

The red line in Figure 2.7 shows the theoretical values for attenuated total reflectance. It can be derived by the Fresnel reflection coefficient formula and Airy's formula [126]. For TE light, the Fresnel formula gives the amplitude reflection at a plane interface between two media with different refractive index:

$$r_{12} = \frac{n_1 \cos\theta_1 - n_2 \cos\theta_2}{n_1 \cos\theta_1 + n_2 \cos\theta_2} \tag{2.8}$$

where r_{12} is the reflection coefficient of media 1 and 2, n_1 and n_2 are their refractive indices respectively, and θ_1 and θ_2 are the incident and refractive angles. Airy's formula gives the reflection coefficient of three-layer structure:

$$r_{123} = \frac{r_{12} + r_{23} e^{-2i\varphi_2}}{1 + r_{12} r_{23} e^{-2i\varphi_2}}, \ \varphi_2 = \frac{2\pi}{\lambda_0} n_2 d_2 \cos\theta_2 \tag{2.9}$$

where r_{123} is the total reflection coefficient of the three-layer structure, r_{12} and r_{23} are the reflection coefficient of media 1 and 2, 2 and 3, respectively, which can be easily found from Equation 2.8, and d_2 is the thickness of medium 2. Similarly, for a four-layer structure, we can find

$$r_{1234} = \frac{r_{12} + r_{234} e^{-2i\varphi_2}}{1 + r_{12} r_{234} e^{-2i\varphi_2}} \tag{2.10}$$

where r_{234} is the reflection coefficient of three-layer structure composed by media 2, 3 and 4. Finally, for the prism coupled PSi waveguide, which is a five-layer structure ((1) prism, (2) air gap, (3) waveguide film layer, (4) substrate layer, and (5) silicon), the reflection coefficient is

$$r_{12345} = \frac{r_{12} + r_{2345} e^{-2i\varphi_2}}{1 + r_{12} r_{2345} e^{-2i\varphi_2}} \tag{2.11}$$

where r_{2345} is the reflection coefficient of four-layer structure composed by media 2, 3, 4 and 5. In the calculation, the refractive indices at 1550 nm are taken to be n_f =1.81 for the waveguide layer and n_s =1.26 for the substrate layer, which were measured by the Metricon 2010/M prism coupler. For grating coupling of light into a waveguide mode at an incidence angle of θ_g=30^o, which is in the middle of the accessible range for our measurement instrument, it is possible to find the correct grating period for this particular sample, Λ=1590 nm, by using Equation 2.7.

2) Fabrication of grating coupler

Grating structures are fabricated on each PSi waveguide using electron beam lithography. A positive e-beam resist, ZEP 520A (Zeon Corp.), is spin-coated onto the PSi waveguide and then soft-baked for 2 minutes on a 180°C hotplate. The resulting resist film is approximately 400 nm thick. Grating exposures are performed on a JEOL-9300FS electron beam lithography tool at the Center for Nanophase Materials Sciences at Oak Ridge National Laboratory at an acceleration voltage of 100 kV and beam current of 2 nA. Completed patterns are

developed in xylenes solution for 30 seconds. Inspection of grating structures after fabrication clearly shows the PSi to be intact and with open pores between the grating resist lines (Figure 2.8) [125].

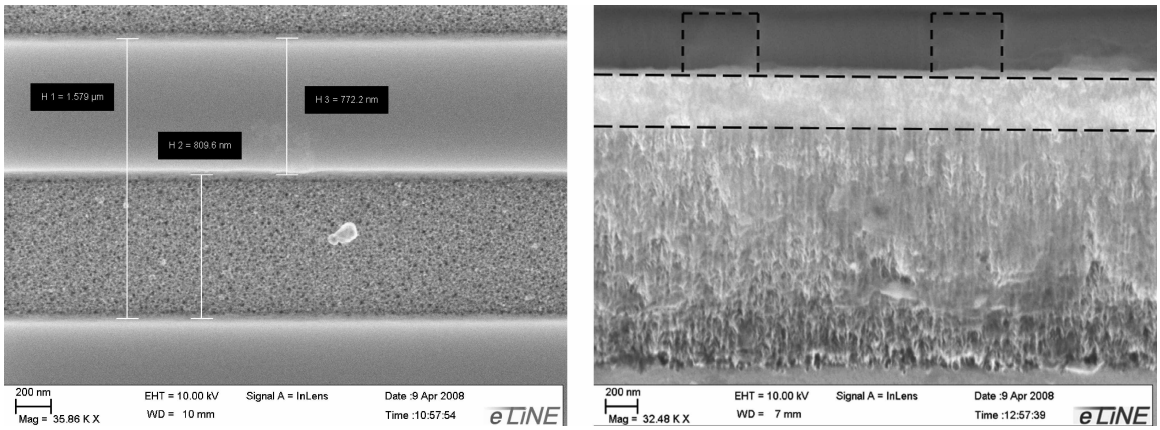

(a) (b)

Figure 2.8 Top-view (a) and section-view (b) SEM images of a photoresist grating coupled PSi waveguide structure.

2.2 Photoresist grating coupled PSi waveguide characterization

2.2.1 Spectrum characterization

In Figure 2.9, the theoretical reflectance (measured by the Metricon Model 2010/M, VAMFO mode) and experimental reflectance of the waveguide after the fabrication of the grating coupler are shown. Figure 2.9 presents the theoretical transmittance of the structure. The theoretical reflectance and transmittance are calculated based on rigorous coupled-wave analysis (RCWA) for rectangular profile gratings [127]. The ZEP 520A (n_{ZEP}=1.54 at 1550nm) grating has

thickness of h=380 nm, air fraction of *f* =0.582, and period of Λ=1590 nm as measured by SEM. This should yield a coupling angle around 30° according to Equation 2.7. The angle-resolved measurements are performed at λ=1550 nm for TE incident light in a range between 10° and 45°. There is a good agreement between theory and experiment.

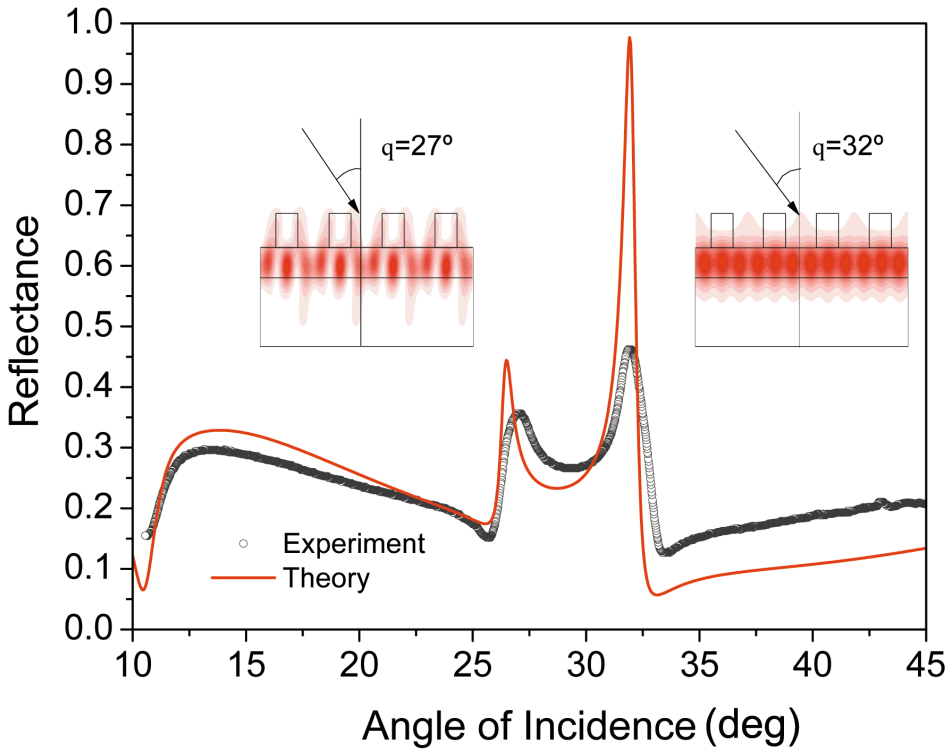

Figure 2. 9 Experimental and theoretical reflectance as a function of the angle of incidence for the PSi waveguide with the grating coupler.

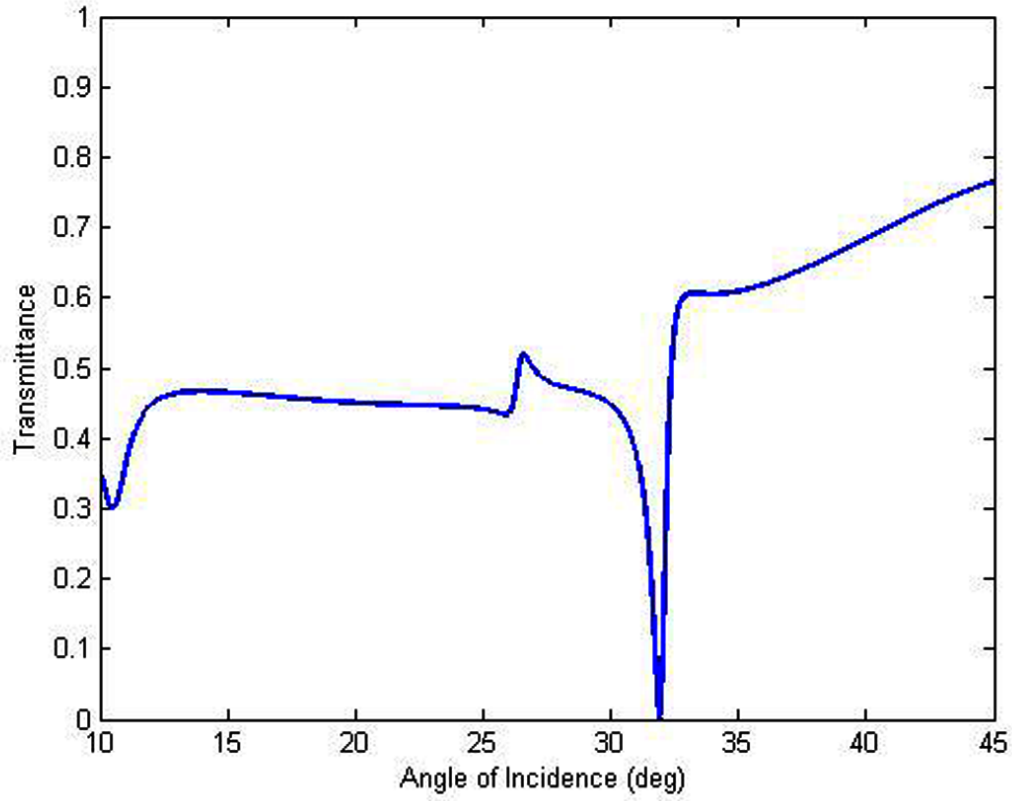

Figure 2. 10 Theoretical transmittance as a function of the angle of incidence for the PSi waveguide with the grating coupler.

When the light energy is coupled into the waveguide, the zeroth-order transmitted intensity will drop, corresponding to the dips at about 27° and 32° in Figure 2.10. In reflection, however, a narrow peak in intensity is observed, as was shown in Figure 2.9. This is due to the principle of reversibility, which states that if light can be coupled into the waveguide then it can also be coupled out of it. As shown in Figure 2.11, the out-coupled light will be coincident with the reflected beam, which will increase the intensity of the reflected light.

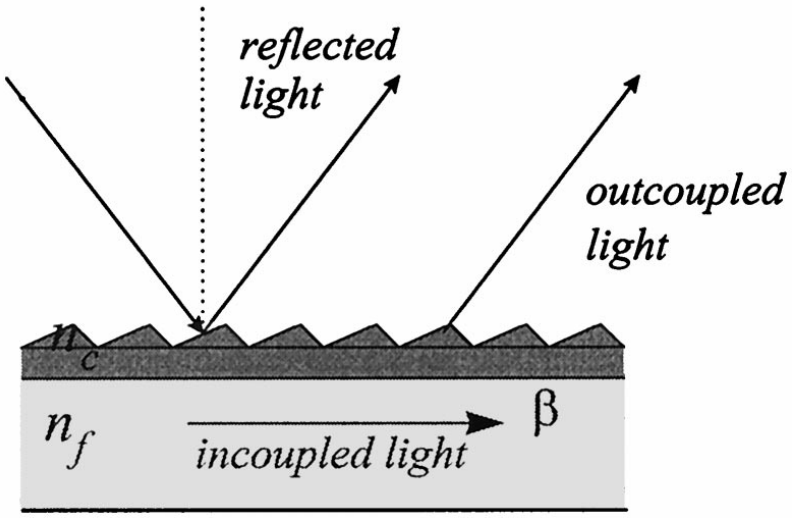

Figure 2. 11 Principle of reversibility in reflection [128].

Two peaks arise because the grating can couple two diffraction orders at two different incident angles. Two field distributions are possible when the guided mode is excited, as shown in Figure 2.9, each with its own peak in the reflectance spectrum. In particular, when the light is incident at 32°, the guided mode, which propagates to the right in the waveguide, is excited by the +1 diffraction order beam. When the light is incident at 27°, however, the guided mode, which propagates to the left, is excited by the -2 diffraction order light. The -2 diffraction order light has lower energy than the +1 diffraction order. Thus, the reflectance peak at 27^o is lower than that at 32^o.

2.2.2 Infiltration effect with 3-APTES

In order to test the photoresist grating coupled PSi waveguide, the effects of infiltration with 3-APTES, which contains an amino group, was first studied. Once the amine is available, numerous cross-linking agents can be used to

immobilize proteins, DNA, or other molecules to silica surfaces. To form a 3-APTES thin film on the PSi pore walls, 100 µl of 4% 3-APTES solution [3−APTES (99%, Aldrich) : methanol : deionized water = 4:46:50] was dropped on the surface of the grating sample. After incubation in a humid environment for 20 min, the sample was rinsed with de-ionized water, dried with nitrogen, and baked at 100 °C for 10 min. In Figure 2.12 (a), the experimental reflectance spectra of the grating-coupled waveguide before and after 3-APTES infiltration is shown. The infiltration leads to the formation of a monolayer of 3-APTES on the surface of the PSi pores and to an increase in the refractive index in the waveguide film and substrate layers in the regions that are not covered by photoresist. As a consequence of the increase in refractive index, the resonance splitting is enhanced. The shifted peaks are found at 25.8° and 33.6°, respectively, for a total splitting of 7.7°, which is almost 3° larger than what is observed with the empty waveguide. Each resonance peak contributes approximately half of the total splitting.

The theoretical model was used to confirm that the splitting could indeed be understood as due to the infiltration of the waveguide. Since the 3-APTES refractive index is almost identical to that of silica, Lugo's model can be used to calculate the effective refractive index change by simply adjusting the air fraction to take into account the infiltration. In Figure 2.12(b), the calculated reflectance spectra for the empty and infiltrated structures are plotted. There is a good agreement with the experimental results when assuming refractive index changes n_f = 0.03351 and n_s = 0.03769 in the waveguide and substrate layers,

respectively, corresponding to monolayer (0.8nm) coverage of 3-APTES in the pores.

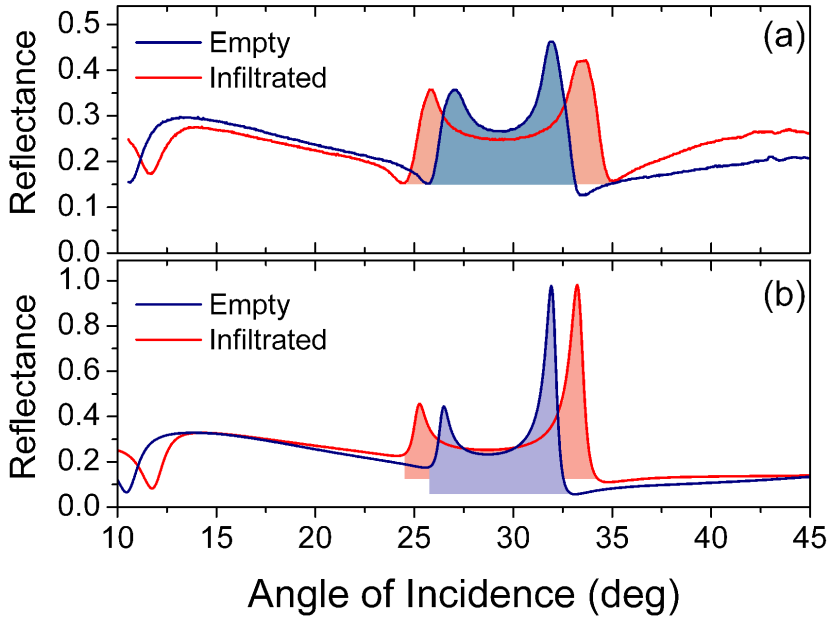

Figure 2. 12 (a) Measured and (b) calculated angle-resolved reflectance at 1550 nm for empty (solid line) and infiltrated (dashed line) PSi waveguide with a photoresist grating coupler.

2.3 DNA experiments

2.3.1 Surface functionalization

With the goal of creating a highly sensitive and selective DNA biosensor, additional functionalization of the silanized PSi waveguides is necessary. After the 3-APTES attachment described in section 2.2.2, the silanized sample were incubated in 2.5 mg/mL Sulfosuccinimidyl 4 - [N-maleimidomethyl] cyclohexane -

1 - carboxylate (Sulfo-SMCC, Pierce) solution for 2 hours, followed by a 1 hour soak in HEPES buffer, rinsing with deionized water, and drying with nitrogen gas. Sulfo-SMCC is a heterobifunctional cross-linking chemical that attaches to an amine group on one side and a thiol group on the other side. 16-base thiol modified probe DNA (5'-TAG CTA TGG TCC TCG T-3', 3' Thiol C3, Eurofins MWG Operon) in HEPES buffer was mixed 1:1 by volume with TCEP (Pierce) in water and ethanol for 30 minutes, and then directly infiltrated into the functionalized PSi waveguide sample. After 1 hour incubation at 37°C, the sample was soaked in HEPES buffer for 20 minutes at the same temperature, rinsed with deionized water, and dried with nitrogen gas to remove any remaining unattached molecules. The functionalization process is illustrated in Figure 2.13. The final antisense DNA hybridization step will be discussed in next section.

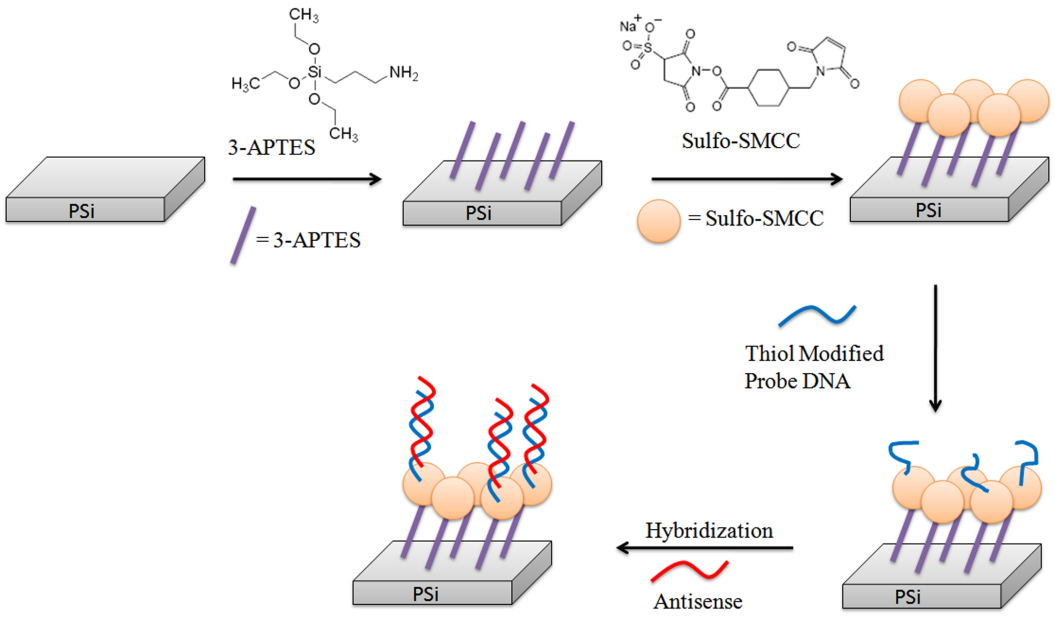

Figure 2. 13 PSi waveguide surface functionalization procedure.

Reflectance measurements were taken after each functionalization step in order to confirm the attachment of the silane, cross-linker, and probe DNA molecules. Figure 2.14 shows the reflectance spectra of a grating coupled PSi waveguide after the attachment of 3-APTES, Sulfo-SMCC, and probe DNA. The reflectance spectra in Figure 2.14 are slightly different from those in Figure 2.12. The reason is that the reflectance spectrum consists of a combination of multi-layer Fabry-Perot oscillations and the grating resonances. Generally, both peaks and dips can be seen for a certain resonance. A resonance peak is only shown at the minimum of the Fabry-Perot spectrum, while a resonance dip can be seen at its maximum. Complete theory details describing this phenomenon can be found in Ref. [129]. Focusing on the resonance near 38^{o} in Figure 2.14, it can be seen that the peak shift after Sulfo-SMCC attachment is almost two times larger than the shift due to attachment of 3-APTES, which is consistent with their molecular sizes (3-APTES monolayer: 0.8 nm [130]; Sulfo-SMCC monolayer: 1.27 nm [131]). Based on the magnitudes of these shifts, it is believed that complete monolayers of 3-APTES and Sulfo-SMCC are formed on the pore walls of the waveguide and theoretical calculations confirm this to be the case. It is noted that if these chemicals were attached only on the surface of the waveguide, a significantly smaller resonance shift would result [52]. Given the size of the probe DNA oligos, the peak shift after probe DNA attachment was smaller than expected, suggesting that there is a relatively low probe density in the PSi waveguide. The probe coverage is estimated to be 13% [132]. DNA

immobilization may have been inhibited in part by the small pore diameters of approximately 30 nm [133].

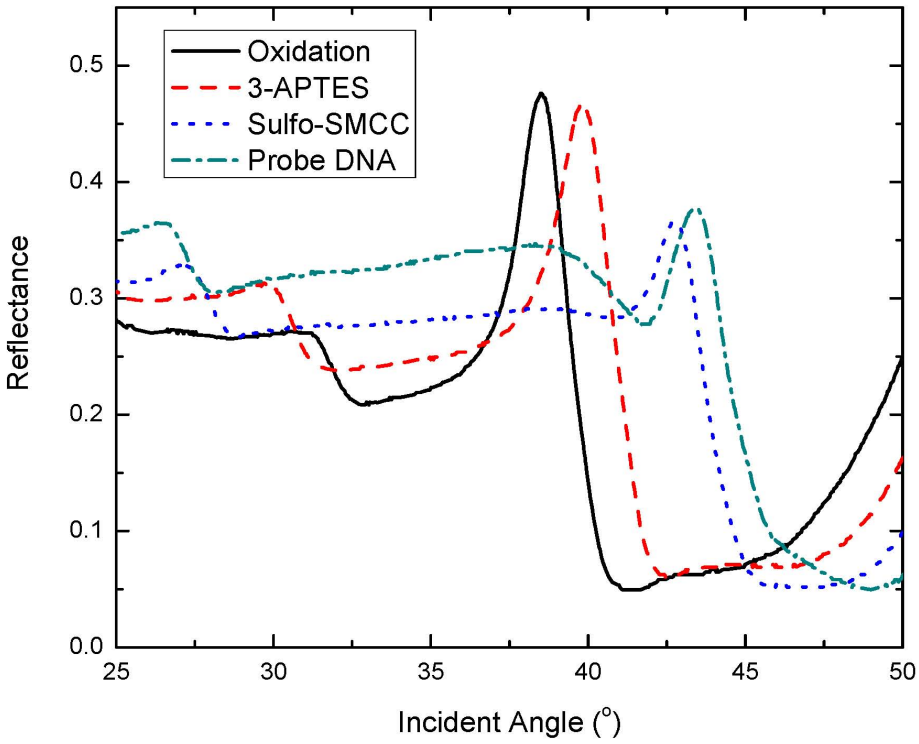

Figure 2. 14 Photoresist grating coupled PSi waveguide reflectance spectra after oxidation and attachment of 3-APTES, Sulfo-SMCC, and probe DNA. The resonance shifts confirm the attachment of these molecules in the oxidized PSi waveguide [116].

2.3.2 DNA hybridization

In order to demonstrate the small molecule biosensing capabilities of our structures, two functionalized grating-coupled PSi waveguides were spotted separately with 100 µmol/L of antisense (5'- ACG AGG ACC ATA GCT A - 3', complementary strand to probe DNA) and mismatch (5' - GGT TTC TGA TGC

TGA C - 3', non-complementary strand to probe DNA) DNA. After 1 hour incubation at 37^{o}C, the waveguides were soaked in HEPES buffer for 20 minutes to rinse out the non-hybridized oligos. Figure 2.15(a) shows a 0.420^{o} resonance shift after the hybridization of antisense, suggesting that the PSi waveguide is indeed capable of detecting DNA sequences. This shift is almost equal to the probe DNA attachment shift in Figure 2.14, which suggests the binding efficiency of DNA strands in pores is relatively high.

In demonstration of the selectivity of this detection, Figure 2.15(b) shows a much smaller, 0.075^{o}, resonance shift due to non-specifically bound mismatch DNA. Slight modification of the rinsing protocol, immobilization procedure, and PSi pore size is expected to reduce the magnitude of this non-specific shift. The magnitude of the resonance shifts after hybridization and exposure to mismatch DNA are reproducible upon measurement of multiple samples. For comparison, a third functionalized PSi waveguide was exposed to HEPES buffer for 1 hour at 37^{o}C. As shown in Figure 2.15(c), a negligible shift results, confirming the stability of the sensor.

By performing several experiments with varying antisense concentration, we can estimate the detection limit of the sensor (Figure 2.16). The average sensitivity is approximately 0.007^{o}/μM. Considering that the resolution of the Metricon prism coupler instrument is 0.015^{o}, the detection limit of the grating coupled PSi waveguide biosensor is estimated to be 2 μM. One method to enhance the sensitivity of the grating coupled PSi waveguide sensor will be discussed in the next chapter. A second approach is to increase the probe DNA

density. One way to do this is to use in-situ DNA synthesis, which has been shown to produce much higher surface coverage (up to ~50%) in a similar PSi waveguide [134].

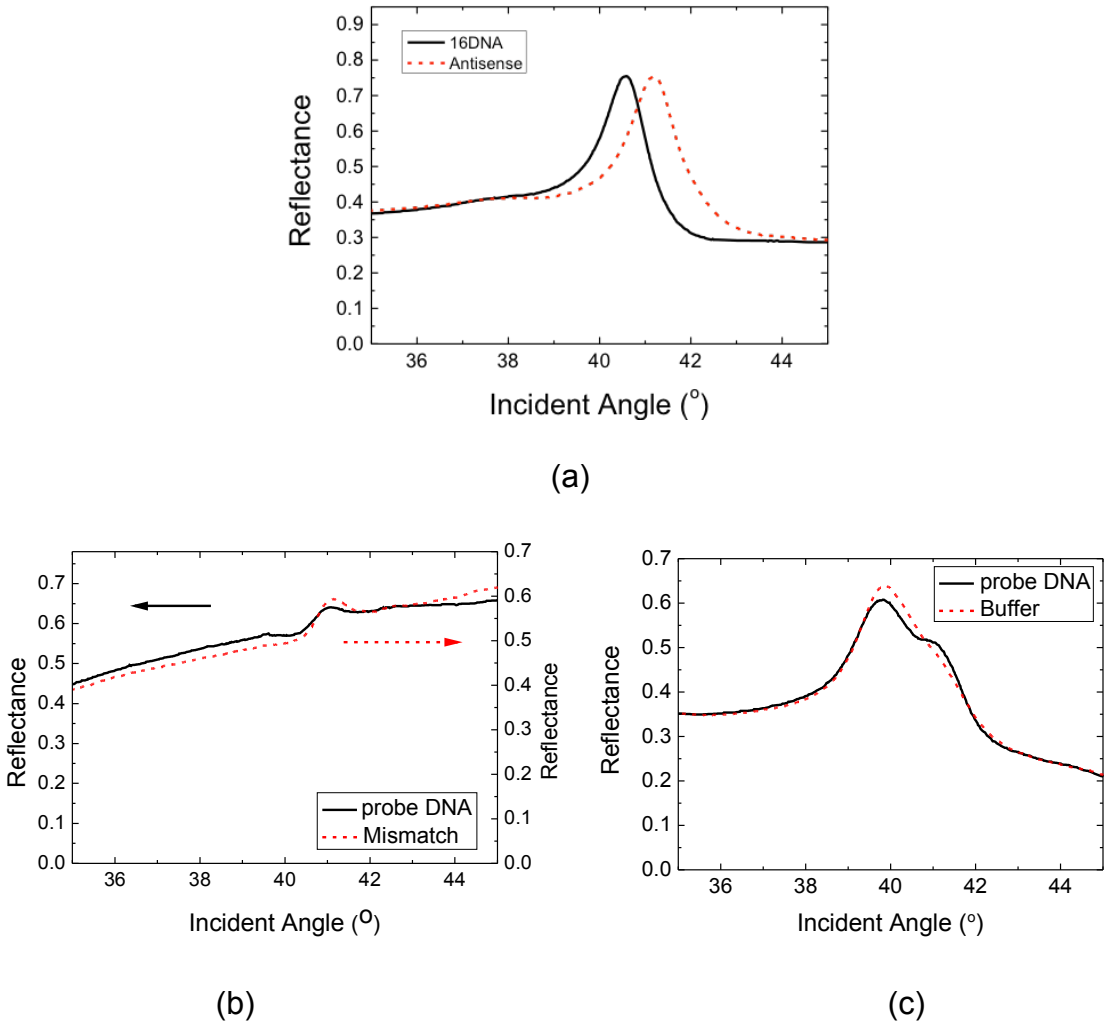

Figure 2. 15 Resonance shifts of grating-coupled PSi waveguides after exposure to (a) antisense DNA, (b) mismatch DNA, and (c) HEPES buffer. Selectivity and stability of the PSi waveguide sensor is demonstrated.

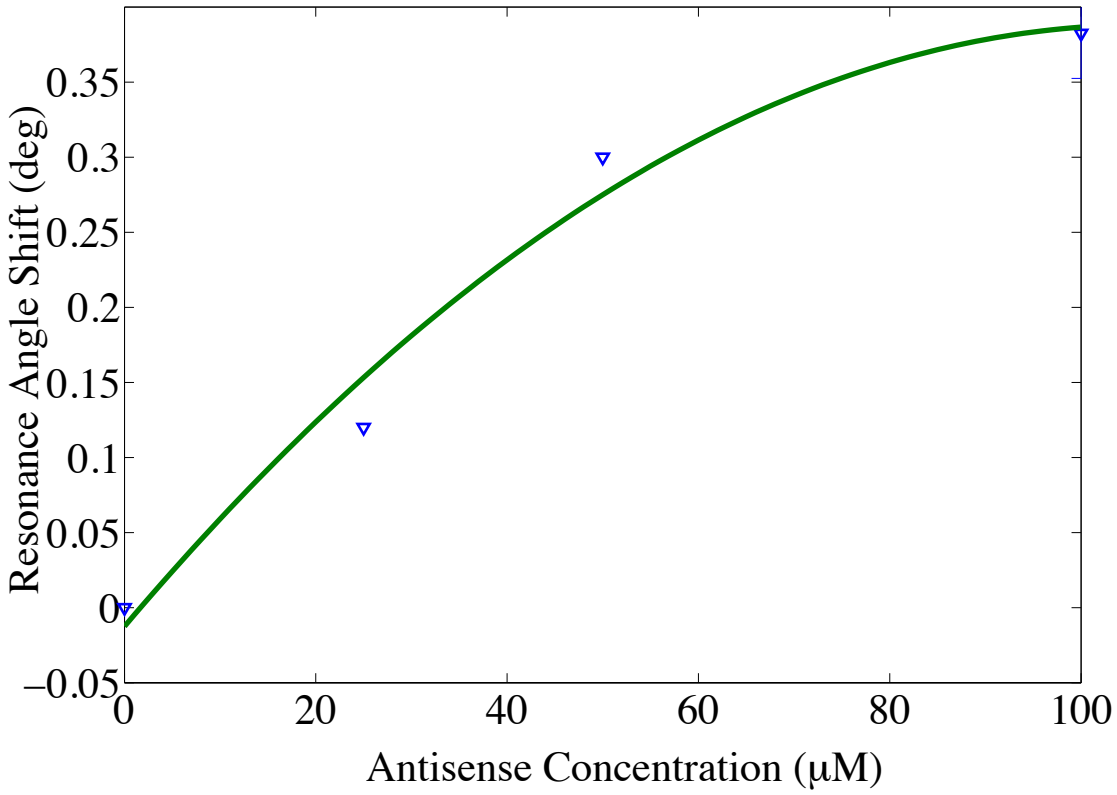

Figure 2. 16 Resonance angle shifts due to different antisense concentrations.

2.4 Conclusion

A label-free PSi waveguide with a photoresist grating coupler is demonstrated for biosensing applications. This is the first time that the benefits of both PSi and diffraction gratings have been combined for the detection of small molecules. The use of a grating coupler instead of a prism coupler allows the device to be more compact. Compared to surface-based sensors, p-type PSi with 10 nm radius pores gives more than 10^5 times larger surface area, which makes it suitable for biomolecular attachment. Strong field confined in the waveguide

region and easy biomolecule infiltration makes it possible to detect small molecules with high sensitivity. There is a good agreement with theory for 3-APTES forming monolayer on pores. DNA hybridization experiments were carried out to test this new structure. Through variable angle reflectance measurements, 16-base antisense DNA oligos were clearly distinguished from mismatch DNA oligos, and the current sensor's sensitivity is found to be 0.007^{o}/μM.

CHAPTER III

ALL-PSI GRATING-COUPLED WAVEGUIDE BIOSENSOR

In chapter II, a compact PSi waveguide biosensor with a photoresist grating coupler is demonstrated to detect molecular binding events in a straightforward manner based on guided mode perturbations. However, the main drawback of the photoresist gratings is that the gratings cover almost half of the PSi waveguide's top surface. Therefore, half of the surface inside the PSi cannot be used for molecule attachment. This results in the experimental sensitivity of the grating coupled PSi waveguide being compromised. In this chapter, an all-PSi grating-coupled waveguide biosensor is created which opens the entire PSi waveguide layer as an active sensing area, thus improving the detection sensitivity compared to the photoresist grating coupled waveguide.

3.1 Theoretical Comparison

In order to evaluate the potential sensing capabilities of grating-coupled waveguides and better understand the advantages of the PSi guided mode sensor, three different configurations of grating-coupled waveguides are examined here, as illustrated in Figure 3.1 [135]. First, for baseline comparison, a traditional silicon-on-insulator (SOI) waveguide with SiO_2 grating, following [113], is considered. Next, PSi waveguides with either photoresist gratings, following chapter II, or lithographically etched PSi gratings are considered. PSi

waveguides with lithographically etched PSi gratings, referred to as all-PSi grating-coupled waveguides, enable the entire internal surface area of the PSi films to be accessible for molecular infiltration. The dimensions of the all-PSi grating-coupled waveguides were chosen such that the total PSi thickness was similar to that of the photoresist grating-coupled PSi waveguide.

RCWA calculations are performed to determine the field distributions in each of the grating-coupled waveguide structures and to evaluate the potential sensing capabilities of each design. For the SOI waveguide (thickness of gratings h_g=180nm; grating period Λ=1240nm; refractive index of gratings n_g=1.45; thickness of waveguide layer h_w=220nm; refractive index of waveguide layer n_w=3.476; thickness of substrate h_s=3000nm; refractive index of substrate n_s=1.45; incident light wavelength λ=1531nm), molecules can only be attached to the top surface of the grating-waveguide structure while for the PSi waveguides, biomolecules can be additionally attached to the pore walls inside the waveguide. Note that for the photoresist gratings on PSi waveguides (h_g=380nm; Λ=1590nm; n_g=1.54; h_w=340nm; n_w=1.80; h_s=1500nm; n_s=1.21; λ=1550nm), only half of the available surface area of the PSi film is accessible for molecular infiltration. As shown in Figure 3.1(a-c), only 1.67% of the transverse magnetic (TM) field power distribution is localized at the top surface (within 180nm of the waveguide surface in the cover region) of the SOI grating-coupled waveguide where molecules can be attached. In contrast, for all-PSi grating-coupled waveguides (h_g=135nm; Λ=1685nm; n_g=1.80; h_w=190nm; n_w=1.80; h_s=1500nm; n_s=1.21; λ=1550nm), 54.07% of the transverse electric (TE) field power distribution is localized within

the waveguide and at the top surface where molecules can be attached. For PSi waveguides with photoresist gratings, the surface area accessible for molecular infiltration is reduced and only 23.27% of the TE field power distribution is localized where molecules will be present. Note also that the fraction of field power in the grating region is increased for the PSi waveguides with photoresist gratings (16.03%) compared to those with etched PSi gratings (3.72%).

Figure 3.1(d-f) show the theoretical reflectance spectra, based on the RCWA calculations, of the three grating-coupled waveguide structures before and after attaching a 0.8 nm thick biomolecule monolayer (n_{bio} = 1.45; e.g., 3-aminopropyltriethoxy-silane). As expected, the magnitude of the resonance shift for each structure directly relates to the fraction of field overlap with molecules [71]. The all-PSi grating-coupled waveguide sensor exhibits a 1.72° resonance angle shift, the photoresist grating-coupled PSi waveguide sensor exhibits a 1.4° shift, and the SOI guided mode resonance sensor exhibits a 0.05° shift due to molecular attachment. From Equation 1.4, the relation between the angular spectrum shift Δθ, acquired at fixed laser wavelength, and the wavelength spectrum shift Δλ, measured at fixed angle θ, can be obtained by derivative calculations on both sides [136]:

$$\Delta\lambda = \Lambda \cdot \cos\theta \cdot \Delta\theta \tag{3.1}$$

where λ is the wavelength, Λ is the gratings period and θ is the incident anlge. The 0.05° resonance angle shift for the SOI guided mode resonance sensor corresponds to an equivalent refractive index change as a resonance wavelength shift of approximately 0.76 nm (for a fixed angle of 45°, a grating period of 1240

nm, and a resonance wavelength near 1530 nm), which is consistent with the simulations and data presented in [113]. Considering the 0.8 nm biomolecules size, the sensitivity of the SOI guided mode resonance sensor is ≈ 1 nm/nm. Similarly, the detection sensitivities of the all-PSi grating-coupled waveguide sensor and the photoresist grating-coupled PSi waveguide sensor are calculated to be ≈ 56 nm/nm and ≈ 41 nm/nm, respectively. Clearly, the additional available surface area in the PSi drastically improves the grating-coupled waveguide sensor performance for small molecule detection. Use of the etched PSi grating instead of the photoresist grating further increases the available active sensing surface area, and will be investigated in detail in the following sections.

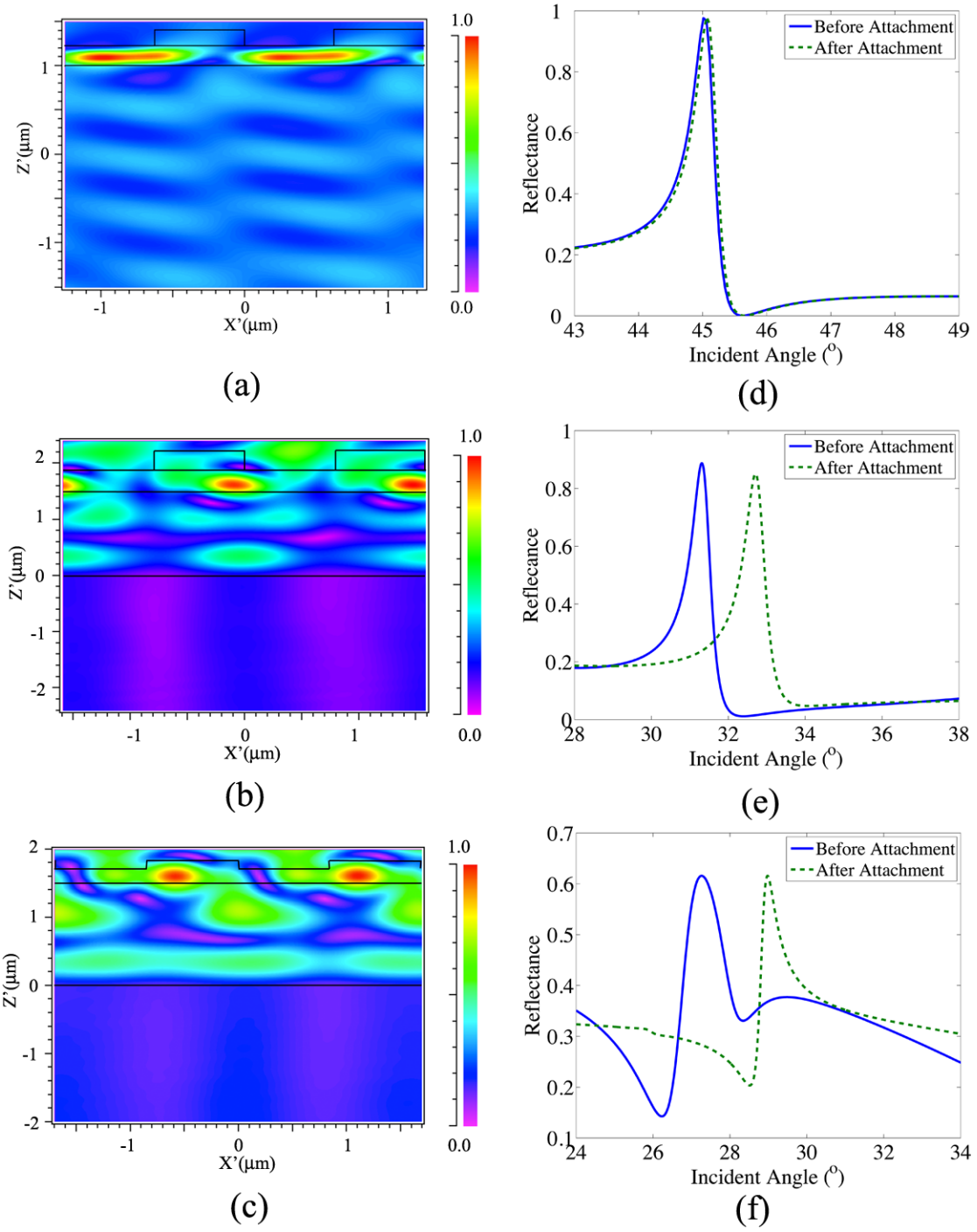

Figure 3. 1 RCWA calculations showing (a) magnetic field distribution of the SOI guided mode resonance sensor; (b) electric field distribution of the photoresist grating-coupled PSi waveguide; and (c) electric field distribution of the all-PSi grating-coupled waveguide structure. Reflectance spectra of (d) SOI guided mode resonance sensor, (e) photoresist grating-coupled PSi waveguide, and (f) all-PSi grating-coupled waveguide structure before and after attaching a 0.8 nm thick monolayer of biomolecules.

3.2 Fabrication

The two-layer PSi waveguide structures used in this work were fabricated by electrochemical etching of p+ (0.01Ω·cm) silicon in 15% ethanoic hydrofluoric acid, similar to the fabrication process in chapter II. The top PSi layer that constitutes the waveguide layer with low porosity (high refractive index) was etched at 5 mA/cm^2 for 62 sec. The bottom PSi layer that constitutes the substrate layer with high porosity (low refractive index) was subsequently etched at 48 mA/cm^2 for 53 sec. The PSi waveguide was then soaked in 1.5 $mmol \cdot L^{-1}$ KOH solution for 30 minutes to widen the pores to promote biomolecule penetration, followed by thermal oxidation at 500°C for 5 min.

PSi grating couplers were fabricated on the PSi waveguide by electron beam lithography and reactive ion etching (RIE). A 300 nm film of PMMA 950 photoresist was spun onto the PSi waveguide and exposed by a Raith eLINE electron beam lithography tool in the Vanderbilt Institute of Nanoscale Science and Engineering to form a diffraction grating with a grating period of approximately 1700 nm. After development, the PSi waveguide with PMMA gratings was reactive ion etched (Trion Technology) with 30 sccm SF_6 flow under 100 W RF power and 30 mTorr chamber pressure for 60 seconds. The PMMA gratings served as the etch mask for the formation of the PSi gratings. After the pattern transfer by RIE was completed, residual PMMA was removed by acetone. Figure 3.2 shows a cross-sectional SEM image of the all-PSi grating-coupled waveguide. Based on this SEM image and other SEM images, it was determined

that the PSi grating height is 132 nm, the period is 1682 nm, and the air fill factor is 49%. Moreover, the waveguide and substrate layers were determined to have thicknesses of 190 nm and 1507 nm, respectively. Based on reflectance spectra measurements and analysis [125], the refractive indices of the waveguide and substrate layers were determined to be 1.80 and 1.21, respectively.

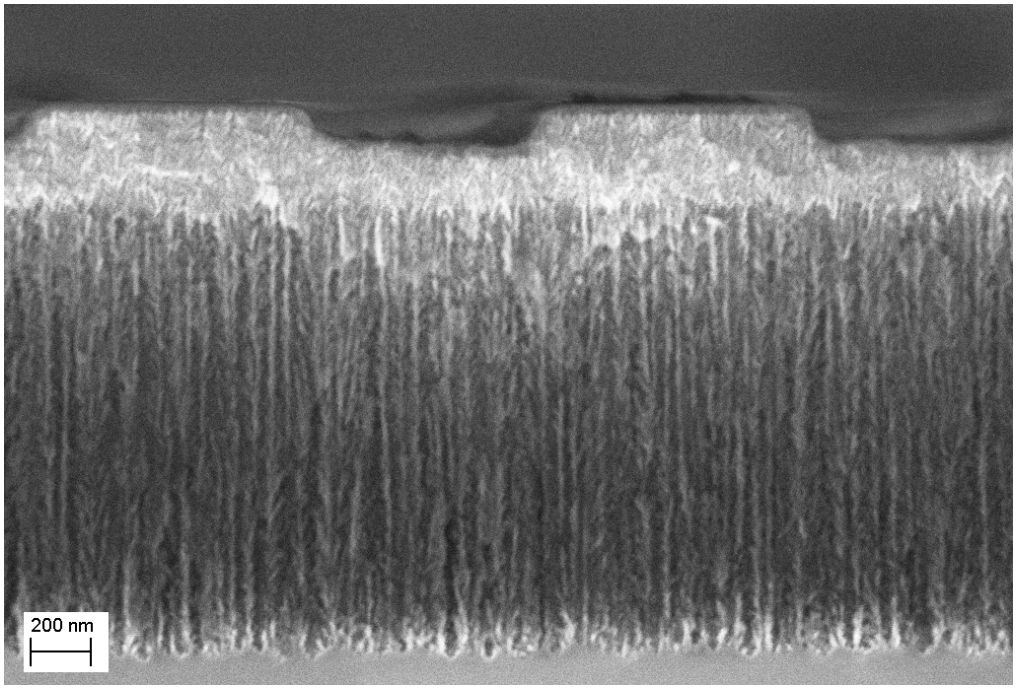

Figure 3. 2 SEM image of the all-PSi gratings and the waveguide (cross-section).

In order to realize experimental comparison of the performance of the PSi waveguide sensors with etched PSi gratings and photoresist gratings, we also fabricated photoresist gratings following the methods reported in chapter II and [113]. The PSi waveguide and photoresist gratings were made using the same procedure mentioned in chapter II. Figure 3.3(a) shows a cross-sectional SEM

image of the photoresist gratings on a PSi waveguide, revealing a grating height of 380 nm, 340 nm thick waveguide layer, and 1485 nm thick substrate layer. An SOI waveguide with SiO_2 gratings was also fabricated to enable experimental comparison of sensor performance for DNA hybridization. First, 180 nm of amorphous SiO_2 was deposited on an SOI substrate (220 nm thick silicon and 2 μm thick buried oxide layer) by plasma enhanced chemical vapor deposition using a Trion Orion II System. Similar to the method to fabricate photoresist gratings on the PSi waveguide, ZEP 520A photoresist was spun onto the amorphous SiO_2 coated SOI wafer and exposed by electron beam lithography (Raith eLINE) to form gratings with 1240 nm period. After serving as a RIE mask to etch the SiO_2 underneath, the photoresist was then removed by Remover PG (MicroChem Corp.). Figure 3.3(b) shows a cross sectional SEM image of the SOI waveguide with SiO_2 gratings, revealing a grating height of 180 nm.

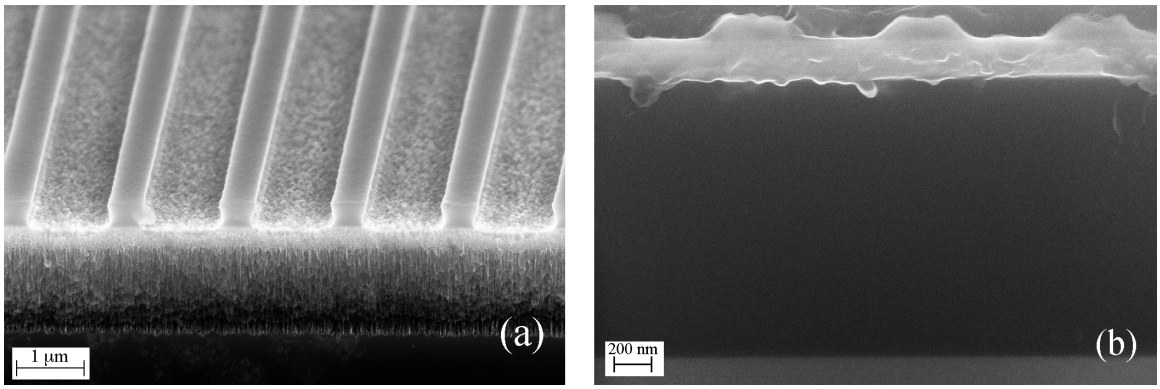

Figure 3. 3 SEM images of (a) photoresist gratings on top of a PSi waveguide and (b) SOI waveguide with SiO_2 gratings. The image in (a) was taken at an angle of 30^o to the planar surface. The apparent non-planarity of the interface between the silicon waveguide and SiO_2 substrate layer in (b) is an artifact due to the sample cleavage.

3.3 DNA hybridization experiments

3.3.1 All-PSi grating-coupled waveguide biosensor

With a similar functionalization procedure as introduced in section 2.3, the all-PSi grating-coupled waveguide biosensor was also used for detecting DNA hybridization. In this case, however, complementary peptide nucleic acid (PNA, ACG AGG ACC ATA GCT A, BioSynthesis) is chosen as the target molecule. Since the PNA contains no charged groups, it has been shown that the binding between PNA/DNA strands is stronger than between DNA/DNA strands due to the lack of electrostatic repulsion [137]. Complementary PNA in HEPES buffer was dropped on the probe DNA immobilized sample and incubated at 37^{o}C for 1 hour. Then the sample was soaked in HEPES buffer for 20 minutes to remove non-hybridized oligos, rinsed with deionized water, and dried with nitrogen gas.

Using the Metricon 2010/M in VAMFO mode, angular reflectance measurements of the all-PSi grating-coupled waveguide were taken after each functionalization step in order to confirm the molecular attachments. The reflectance spectra before and after the 3-APTES attachment are shown in Figure 3.4(a). The waveguide resonance angle is shifted to a higher angle (1.77° shift) due to the increase in refractive index of the PSi layers that results from the 3-APTES attachment on the pore walls. In order to verify monolayer attachment of 3-APTES (0.8 nm size, $n_{3\text{-APTES}}$ = 1.45), RCWA simulations were performed using the experimentally determined dimensions of the all-PSi grating-coupled

waveguide. In Figure 3.4(b), the calculated reflectance before and after attachment of a monolayer of 3-APTES molecules are plotted, which indicates a resonance shift of 1.80°. Thus, the calculated angular reflectance spectra exhibit good agreement to the experimental data, and we can assume nearly complete monolayer coverage of the small 3-APTES molecules in the pores. Based on the RCWA calculations, the refractive index changes caused by 3-APTES attachment are found to be $\Delta n_{waveguide}$ = 0.0427 and $\Delta n_{substrate}$ = 0.0509. Hence, the detection sensitivity of the all-PSi grating-coupled waveguide for small molecules is approximately 42°/RIU, corresponding to 1090 nm/RIU for a wavelength interrogation measurement. The detection limit of the sensor depends ultimately on the measurement instrument resolution. Given the Metricon 2010/M angular resolution of 0.0075° in the VAMFO mode or considering a spectral measurement instrument with a modest resolution of 0.1 nm, the anticipated detection limit of the sensor is on the order of 10^{-4} RIU.

Figure 3.5(a) shows the reflectance spectra of the all-PSi grating-coupled waveguide after the sequential attachment of 3-APTES, Sulfo-SMCC, 16-mer probe DNA (50 μmol·L^{-1}), and 16-mer complementary target PNA (50 μmol·L^{-1}). The measured resonance shifts are stable over time durations of several minutes, suggesting that there is no liquid remaining trapped in the pores after each molecular infiltration step that can evaporate during the duration of the experiment. Note that attachment of Sulfo-SMCC leads to a larger resonance peak shift than 3-APTES attachment, which is consistent with their molecular size (3-APTES monolayer: 0.8 nm [130]; Sulfo-SMCC monolayer: 1.27 nm [131].).

The resonance shift due to probe DNA attachment is comparatively small with respect to its molecule size (~ 3.5 nm in length), suggesting that there is a relatively low probe density in the PSi waveguide. Based on the magnitude of the experimentally measured resonance shift (0.42°), RCWA calculations suggest that the probe DNA coverage on the pore walls is approximately 10%. This low coverage is attributed primarily to the size-dependent infiltration efficiency of small molecules into the small pore diameters (~ 20 nm) [132], as well as a possible contribution of charge-based exclusion of the DNA molecules. When exposed to the complementary PNA sequence, the majority of the probe DNA molecules were hybridized. Based on the magnitude of the experimentally measured resonance shift after PNA attachment (0.39°), the hybridization rate is estimated to be ~90%.

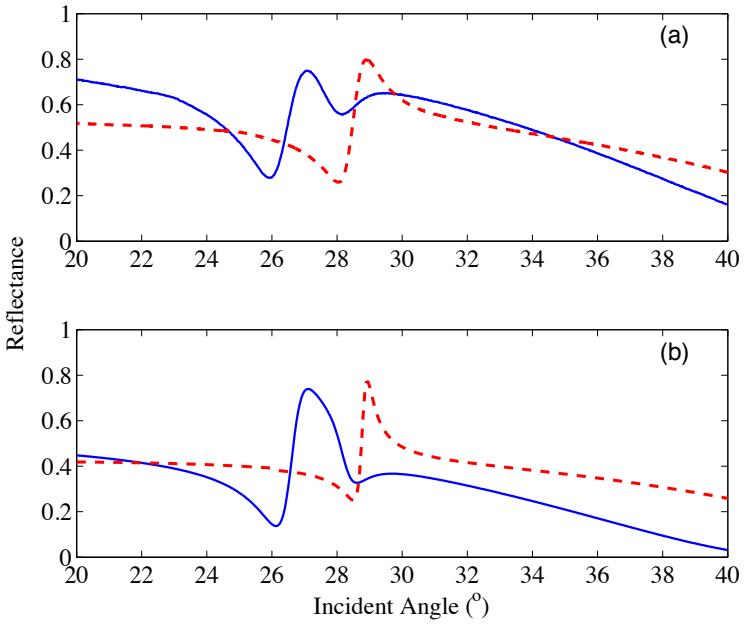

Figure 3. 4 (a) Measured and (b) calculated angle-resolved reflectance spectra at 1550 nm (TE) for all-PSi grating-coupled waveguide after oxidation (solid line) and after 3-APTES attachment (dashed line).

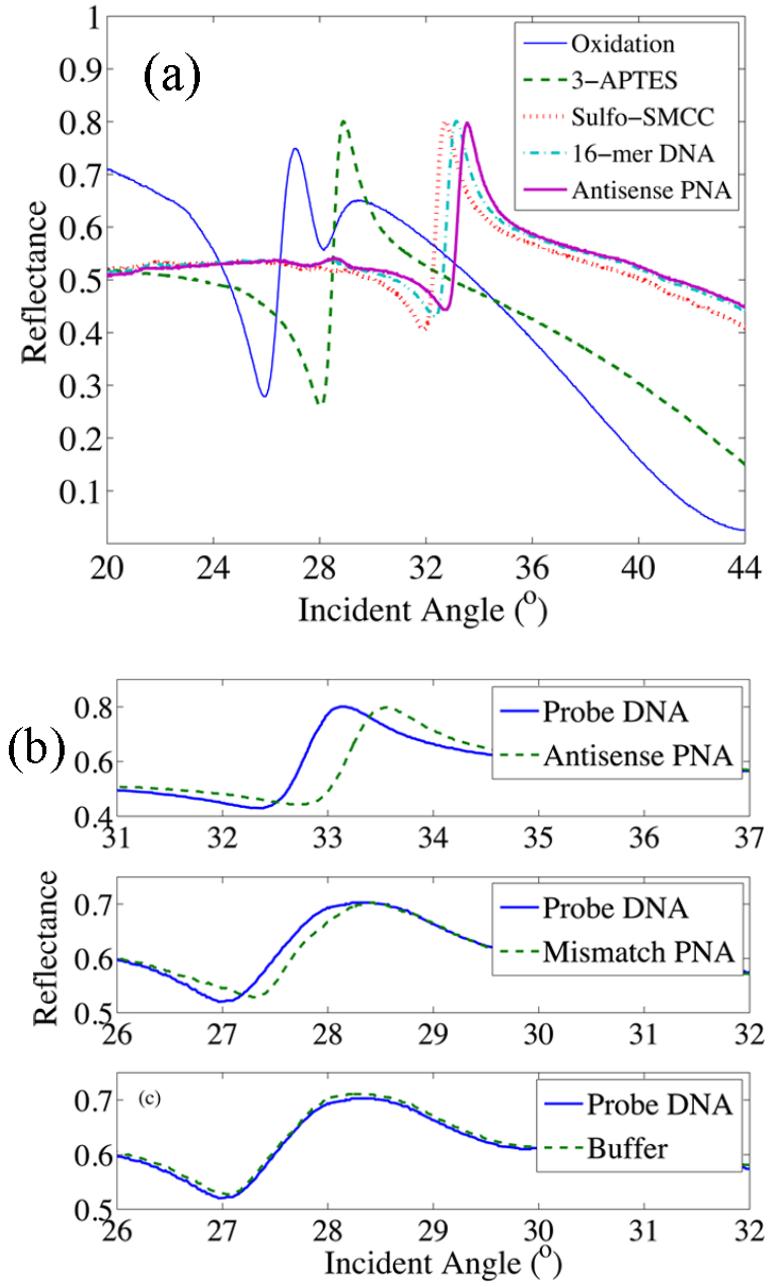

Figure 3. 5 (a) Reflectance spectra of all-PSi grating-coupled waveguide after oxidation and attachment of 3-APTES, Sulfo-SMCC, 16-mer probe DNA (50 μM) and complimentary PNA (50 μM). (b) Resonance shifts of all-PSi grating-coupled waveguides functionalized with 16-base probe DNA (50 μM) after exposure to complimentary PNA (50 μM), mismatch PNA (50 μM) and HEPES buffer.

In order to confirm the selectivity of the all-PSi grating-coupled waveguide sensor, a mismatched sequence of PNA (ACG AGG ACC ATA GCT A) and HEPES buffer solution were separately exposed to similarly prepared all-PSi grating-coupled waveguides. As expected, and as shown in Figure 3.5(b), the resulting shifts of the waveguide resonance angle for mismatch PNA (0.07°) and HEPES buffer (0.015°) were substantially less than that for the complementary PNA sequence.

Finally, in order to establish an approximate sensitivity for the all-PSi grating-coupled waveguide, several hybridization experiments were performed with fixed probe DNA concentration of 100 $\mu mol \cdot L^{-1}$ and variable complementary PNA concentration. As shown in Figure 3.6, the linearity of the resonance angle shift as a function of PNA concentration suggests a detection sensitivity of approximately 7.3°/mM. Note that the data point at 0 μM PNA concentration corresponds to the resulting resonance shift from exposure to the HEPES buffer alone. Given the angular resolution of the Metricon 2010/M in the VAMFO mode, the PNA detection limit is expected to be on the order of 1 μM.

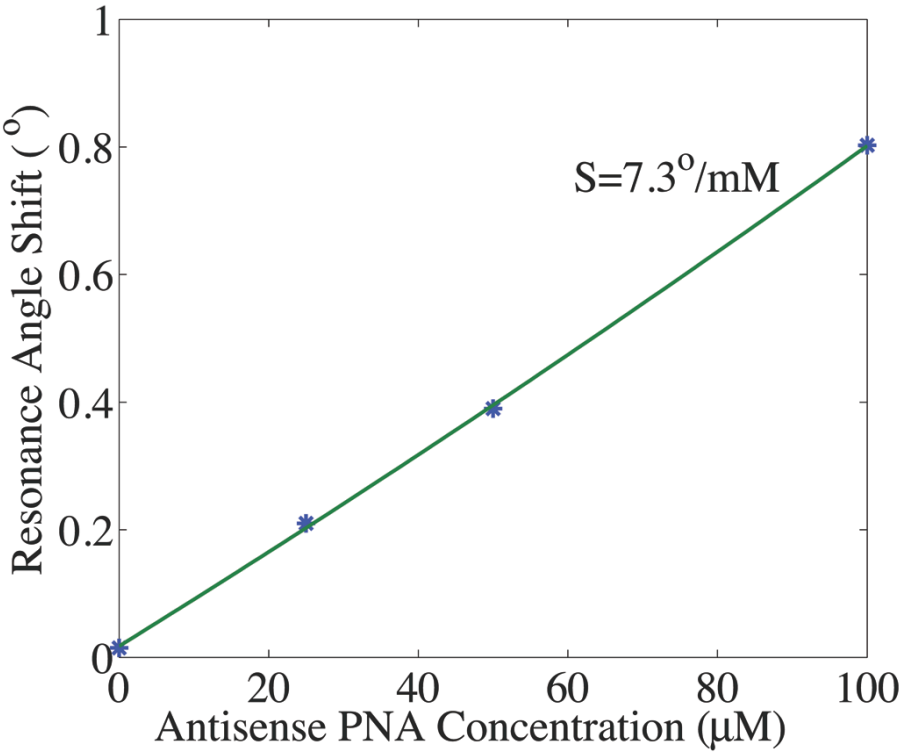

Figure 3. 6 Detection sensitivity estimation for all-PSi grating-coupled waveguide sensor based on resonance angle shifts due to exposure of sensor to different complementary PNA concentrations. The 16-mer probe DNA concentration for all samples represented in the figure is 100 μM. The typical sample-to-sample variation in the resonance angle for each data point is ±0.1°.

3.3.2 Photoresist grating biosensor & SOI waveguide biosensor

In order to experimentally compare the detection sensitivities of the different grating-coupled waveguide configurations considered in section 3.1, the same optical measurements described in section 3.3.1 were performed on both the photoresist grating-coupled PSi waveguide biosensor and the SOI waveguide with SiO_2 gratings biosensor. Although only one SOI guided mode resonance sensor was prepared for this study, the experimentally measured resonance

shifts due to molecular attachment are in good agreement with expectations based on theoretical calculations. Table 3.1 gives the resonance angle shifts of the three different biosensor structures after each molecule attachment step. As expected, the resonance angle shifts for the photoresist grating-coupled PSi waveguide were less than those of the all-PSi grating-coupled waveguide biosensor because the photoresist gratings inhibit molecular infiltration into the PSi regions beneath the gratings. Note, however, that the hybridization efficiency of the two types of grating-coupled PSi waveguide sensors is comparable: based on several DNA hybridization experiments, including those reported in [116], the hybridization efficiency in photoresist grating-coupled PSi waveguides is 80% - 92%. For the SOI grating-coupled waveguide biosensor that can only accommodate molecular binding on the top surface of the sensor, Table 1 shows that comparatively small resonance shifts were observed after molecular attachment, which are consistent with the theoretical calculations in section 3.1. The high hybridization efficiency is attributed to relatively low probe DNA coverage (~30%, according to RCWA calculations) on the surface of the SiO_2 gratings [138, 139], and ease of access of the complementary PNA molecules to the probe DNA molecules on the planar sensor surface.

Table 3. 1 Resonance angle shifts after various molecular attachments in all-PSi grating-coupled waveguide, photoresist grating-coupled PSi waveguide, and SOI waveguide with SiO_2 gratings.

	3-APTES	Sulfo-SMCC	Probe DNA (100 µmol·L^{-1})	Antisense PNA (100 µmol·L^{-1})
All-PSi grating	1.70° ± 0.17° [a]	3.82° ± 0.07° [a]	0.83° ± 0.16° [a]	0.81°
Photoresist grating	1.47° ± 0.13° [b]	2.46° ± 0.44° [b]	0.70° ± 0.04° [b]	0.59° ± 0.08° [b]
SOI-SiO_2 grating	0.038°	0.046°	0.058°	0.062°

[a]Data is based on three experiments.
[b]Data is based on five experiments.

3.4 Stamped grating-coupled PSi waveguide biosensor

An alternative,more cost-effective and more rapid way to fabricate a grating-coupled waveguide structure exclusively made of PSi is based on a recently reported technique that enables rapid and cost-effective nanoscale patterning of porous materials. This technique, known as DIPS (direct imprinting of porous materials), is reported in detail in reference [140].

3.4.1 Fabrication of stamped gratings

DIPS can be used to fabricate PSi gratings by using a silicon grating stamp to locally deform the PSi film [140]. Briefly, a reusable master stamp is fabricated using standard lithographic techniques. The stamp is then directly pressed into a porous substrate where pattern transfer occurs by local pore deformation or crushing. In this work, the master stamp consisted of a silicon grating with a pitch of 1700 nm. Since the imprinted grating depth scales with the hardness of the PSi film, three PSi layers were utilized for the waveguides with stamped gratings: the top layer that becomes the grating is of high porosity to

reduce the hardness compared to the silicon stamps; the second and the third layers that serve as the waveguide film and the substrate layer are designed in a manner similar to that reported in the previous section. Note that the field confinement of the guided mode will be slightly different in this three-layer design compared to the two-layer PSi waveguide design described previously. The fabrication process flow for the PSi waveguides with imprinted gratings is as follows. Electrochemical etching of p+ (0.01Ω•cm) silicon is first performed with sequential application of two current densities 60 mA/cm^2 for 10 sec and 5 mA/cm^2 for 73 sec to form the top two PSi layers. After widening the pore openings with a 30 min soak in KOH, the silicon stamp (area ≈ 9mm^2) was then pressed against the PSi sample using a force of 650 lbs to locally crush the top PSi layer and form PSi gratings with a depth of 250 nm and a pitch of 1700 nm [141]. A second electrochemical etching step was then performed with the application of 48 mA/cm^2 for 53 sec to form the waveguide substrate layer. While the pores in the stamped regions are partially occluded compared to the unstamped regions, the pores in all regions are sufficiently large to enable electrolyte penetration and uniform etching of the third PSi layer. The third PSi layer was formed after the stamping to ensure that this high porosity layer was not damaged during the stamping procedure. Figure 3.7 shows SEM images of the stamped gratings and PSi waveguide.

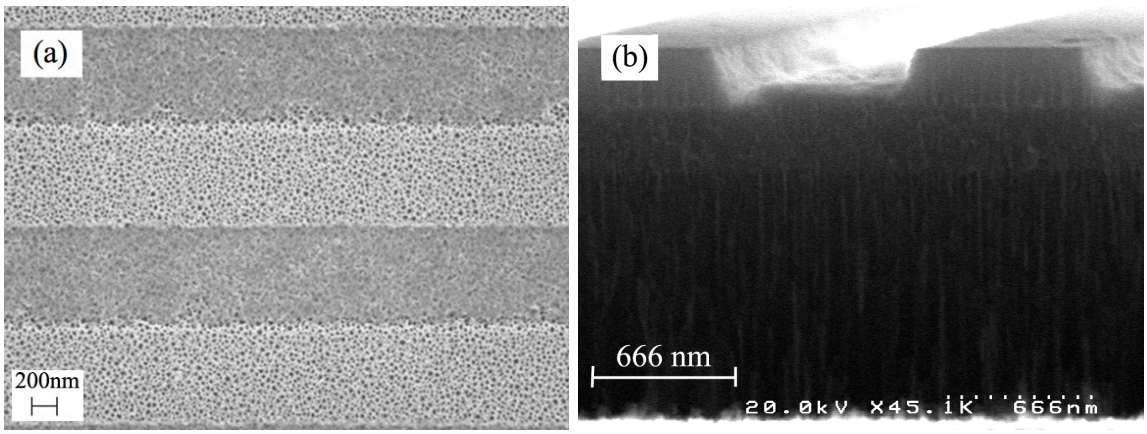

Figure 3.7 Top view (a) and cross-sectional (b) SEM images of PSi gratings and waveguide fabricated using the DIPS technique. The pores in the stamped regions are partially occluded compared to the unstamped regions.

3.4.2 Waveguide loss measurement

In order to obtain an experimental estimate of the difference in mode confinement of the two different waveguide designs, waveguide loss measurements were performed using the scattered light measurement approach [142]. To prevent guided light from coupling out through the gratings, which would lead to a misrepresentation of the waveguide propagation losses, regions of the waveguides without grating couplers were measured. Light from a 1550 nm diode laser was butt-coupled into each PSi waveguide using a tapered optical fiber. A camera positioned above the waveguide and focused on the sample plane collected the scattered light from the surface of the waveguide. Since the scattered light mimics the rate of decay of light in the waveguide, straightforward image processing can be used to determine the intensity of scattered light as a function of propagation distance. The waveguide loss in

dB/cm was estimated based on the best exponential fit to the intensity vs. distance curve.

Figure 3.8 shows experimental results for 2-layer and 3-layer PSi waveguides loss measurements. The PSi waveguides were fabricated as previously described and oxidized at 500°C for different lengths of time. It has been previously shown that oxidizing PSi films reduces their losses [142]. Accordingly, PSi waveguides without oxidation have comparatively high loss, ~20 dB/cm. A rapid reduction of the losses was observed after oxidation times as short as 5 min. Longer oxidation times lead to lower waveguide losses, although the rate of loss reduction with oxidation time drops significantly after 30 min. The slight differences between the 2-layer and 3-layer waveguide losses were found to be within normal sample variation. Moreover, calculations based on Maxwell equations suggest that the electric field confinement of the guided mode in the 2-layer waveguide (73%) is approximately the same as that in the 3-layer waveguide (77%). Therefore, since the losses and mode confinement of the two types of waveguides are nearly identical, any difference in the detection sensitivity towards molecular infiltration must arise from the grating fabrication process.

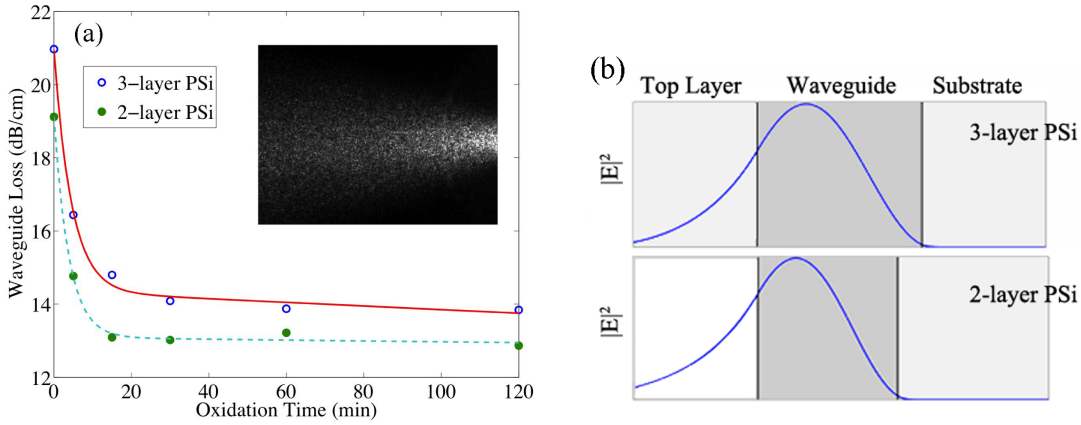

Figure 3.8 (a) Measured PSi waveguide losses as a function of oxidation time at 500°C. Curve fits are provided as a guide for the eye. Insertion is a digital image of the light scattering. (b) 3-layer and 2-layer PSi waveguide electric field distributions.

3.4.3 DNA Hybridization

While waveguide loss is an important characteristic of integrated optical devices, it is not a critical parameter for our biosensing application because long propagation length inside the waveguide is not required for molecular detection. In order to prepare the PSi waveguides for molecular attachment, the stamped grating sample was first thermally oxidized in air ambient at 500°C for 5 min. Next, similar to the hybridization procedure in chapter II, 3-APTES and Sulfo-SMCC were sequentially attached to the pore walls to suitably prepare the surface for binding of thiol-modified 16-mer probe DNA (5'-TAG CTA TGG TCC TCG T-3', 3' Thiol C3, 100 μmol·L^{-1}). Complementary peptide nucleic acid (PNA, ACG AGG ACC ATA GCT A, 100 μmol·L^{-1}) molecules were then selectively

hybridized to evaluate the performance of the stamped grating-coupled PSi waveguide sensor.

Figure 3.9 shows the results of angle-resolved reflectance measurements of the stamped grating-coupled PSi waveguides after thermal oxidation and attachment of 3-APTES, Sulfo-SMCC, 16-mer probe DNA and complementary PNA molecules. The resonance peak shift resulting from each functionalization step confirms that the molecules are indeed attached to the pore walls. Compared to the DNA hybridization results shown in Figure 3.5 for the all-PSi grating-coupler waveguide biosensor, the peak resonance shifts of the 3-APTES and Sulfo-SMCC attachment is slightly larger in the stamped grating samples, due to the thicker waveguide layer, which accommodates more molecules. In the case of the 16-mer probe DNA molecular (~3.52 nm) attachment, there is a significant difference in the magnitude of the corresponding resonance peak shifts for the all-PSi biosensor and the stamped grating-coupled waveguide. Although the stamped gratings are easier and more cost-effective to fabricate, the resulting partial pore occlusion in the stamped region inhibits the infiltration of larger molecules in the PSi waveguide sections beneath the stamped grating; effectively, half of the surface area of the waveguide is not accessible for sensing molecules larger than approximately 2 nm. Thus, for comparatively small molecules, the two types of grating-coupled waveguides provide similar detection sensitivities, while for larger molecules, the sensitivity of the all-PSi grating-coupled waveguides is superior.

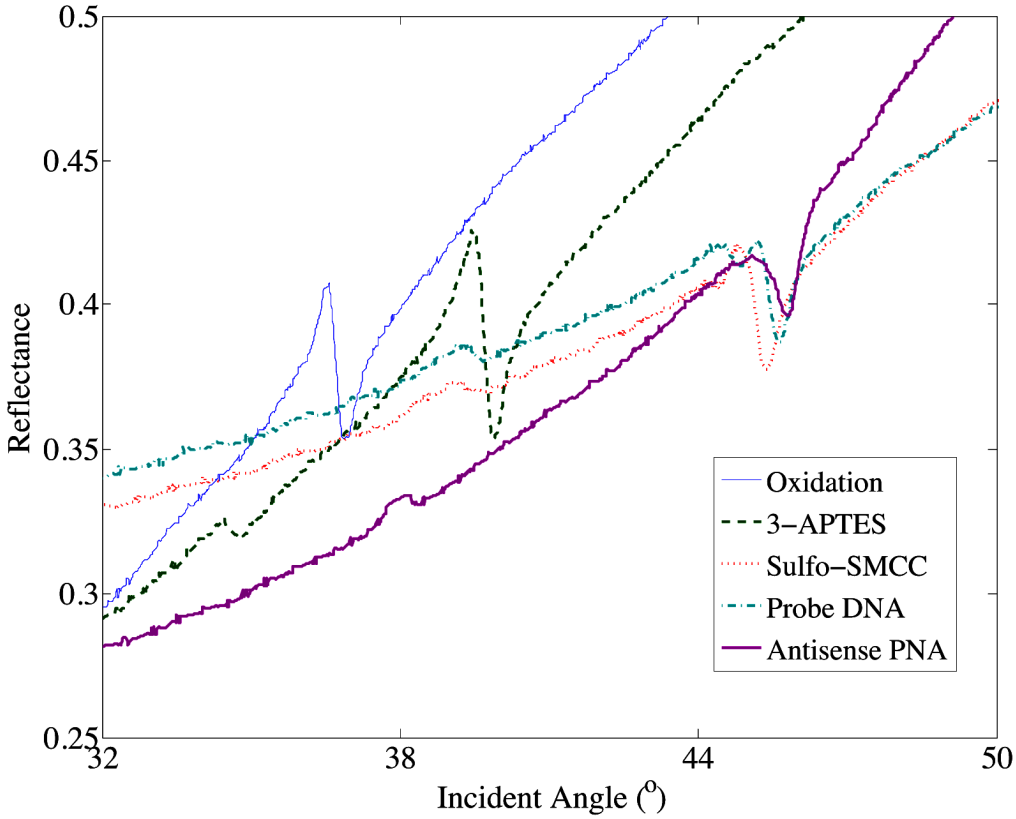

Figure 3.9 Stamped grating-coupled PSi waveguide reflectance spectra after oxidation and attachment of 3-APTES, Sulfo-SMCC, probe DNA, and complementary PNA molecules.

3.5 Conclusion

Due to their enhanced available surface area for molecular binding in regions of strong field localization, all-PSi grating-coupled waveguides were shown to be highly efficient biosensors. RCWA calculations demonstrated that all-PSi grating-coupled waveguides supported a 32-fold higher field distribution in regions where molecules could bind compared to planar grating-coupled SOI waveguides, and a 2-fold higher field distribution compared to photoresist

grating-coupled PSi waveguides. Experiments conducted on all three types of grating-coupled waveguides similarly showed that waveguide resonance shifts due to molecular attachment were substantially larger in the all-PSi grating-coupled waveguide sensor. A small molecule detection sensitivity of 42°/RIU (1090 nm/RIU), and PNA detection limit on the order of 1 μM were demonstrated using the all-PSi grating-coupled waveguide. A second type of PSi waveguide with a PSi grating coupler was also demonstrated based on the DIPS stamping process. Although DIPS allows for rapid and low-cost fabrication of grating-coupler waveguide biosensors exclusively made of PSi, the partial pore occlusion that results in the stamped regions inhibits the infiltration of some molecules into the waveguide sensing region. For molecules smaller than approximately 2 nm, the detection sensitivity of the PSi waveguides with stamped gratings was the same as that of the all-PSi waveguides. For larger molecules, such as 16mer nucleic acids, the lithographically fabricated all-PSi grating-coupled waveguides exhibited almost two times larger detection sensitivity. Waveguide losses in both designs of the PSi waveguide with PSi grating coupler were on the order of 10dB/cm.

CHAPTER IV

INTEGRATED PSI WAVEGUIDE BIOSESNOR

The all-PSi grating-coupled waveguide biosensor was fully studied in chapter III. This design with all of the PSi waveguide layer accessible to molecular infiltration gives the highest detection sensitivity compared to the photoresist grating-coupled PSi waveguide biosensor and the conventional evanescent wave-based biosensors such as the SOI waveguide biosensor. Other advantages of the all-PSi grating-coupled waveguide biosensor, such as silicon-compatibility and an open top-side, make it suitable to be combined with a micro-channel to form an integrated real-time sensing platform. In this Chapter, a flow cell integrated PSi waveguide biosensor is demonstrated to facilitate near real-time monitoring of biomolecule attachment events and enable determination of the kinetics parameters of several kinds of biomolecules. The diffusion coefficient, and adsorption and desorption rate constants of different sized chemical linker and nucleic acid molecules are determined based on the rate of change of the measured resonance angle after exposure to the molecules.

4.1 Adsoprtion kinetics in PSi

Quantifying the kinetic properties of biomolecules is essential to understanding many biomolecular mechanisms, from primary processes in biomolecular recognition to interaction networks in living cells [143]. Label-free

optical biosensors based on the resonant waveguide grating method for biomolecular interaction analysis have emerged over the last two decades as powerful tools that are capable of detecting the interactions of proteins and genes. They have received a great deal of attention for efficient, affordable, accurate, non-invasive and quantitative measurements in real-time [144-153]. Many of these devices utilize gratings to couple light into/out of waveguides. When molecules attach to the waveguides, which are functionalized with immobilized probe molecules, the optical sensing elements can efficiently convert refractive index changes caused by the attachments to a measurable spectral shift. Conventional grating-waveguide biosensors generally rely on evanescent field sensing techniques, which only allow target analytes to bind to planar surface-bound probe molecules [154]. However, the aforementioned all-PSi grating-waveguide biosensor, which allows molecules to infiltrate into the core of the waveguide where they interact with a guided mode, gives 32-fold greater detection sensitivity [125, 135]. In this chapter, the biosensor is combined with a polydimethylsiloxane (PDMS) flow cell to facilitate near real-time monitoring of biomolecule attachment events inside the PSi to derive the kinetics parameters of several kinds of biomolecules.

The two-dimensional model used in this work to analyze adsorption kinetics in PSi takes into account mass transport and binding reactions between molecules in bulk solution and immobilized groups at the pore walls. The PSi waveguide with flow cell geometry is shown in Figure 4.1(a)-(c). For the PSi waveguide biosensor used in this chapter, the porosity in the upper layer

(waveguide layer) is approximately 64%, with 200 nm depth, and 87% porosity for the lower layer (substrate layer), which is 1500 nm in depth. The waveguide was redesigned to optimize its performance with liquid instead of air in the cover region. Measurements were taken in a static state so the flow velocity in the fluid channel is zero and only diffusion in the y-direction is considered for mass transport. The diffusion equation is given as

$$\frac{\partial c(y,t)}{\partial t} = D\frac{\partial^2 c(y,t)}{\partial y^2}, 0 \le y \le b \tag{4.1}$$

with the following initial and boundary conditions:

$$\text{at } t = 0,\ c = c_b \text{ for all } 0 \le y \le b \tag{4.2}$$

$$\text{for all } t,\ c(y = \frac{b}{2}) = c_b \tag{4.3}$$

$$\text{at } y = 0, \frac{d\Gamma(t)}{dt} = D\frac{\partial c(0,t)}{\partial y} = k_{ad}c(0,t)(\Gamma_{\max} - \Gamma(t)) - k_{des}\Gamma(t) \tag{4.4}$$

where *c(y, t)* is the concentration of the molecule, *D* is the diffusion coefficient of the molecule, c_b is the bulk concentration of the molecule in the flow cell, *b* is the thickness of flow cell, *Γ(y, t)* denotes molecule surface concentration, Γ_{max} is the maximum surface concentration, k_{ad} is the adsorption rate constant and k_{des} is the desorption rate constant of the molecule. The boundary condition give in Equation (4.4) assumes first order Langmuir kinetics at the PSi top surface [155, 156].

The Equation (4.1), together with boundary condition (4.2), (4.3) and (4.4), can be solved by various numerical methods. Here, since the numerical solutions

are complex and time-consuming, these equations need to be simplified to yield useful analytical results.

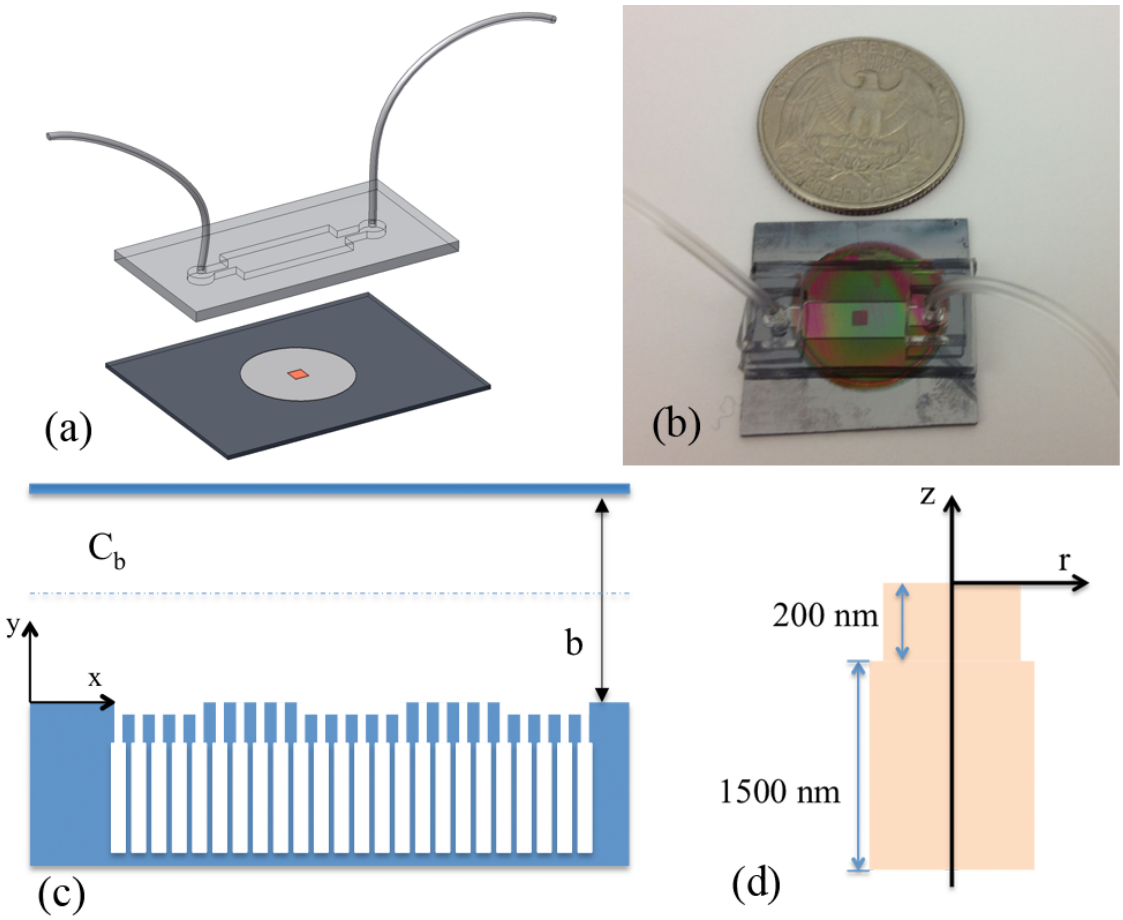

Figure 4. 1 Design of the PDMS flow cell integrated biosensor. (a) A schematic of the two components: the bottom is the PSi (light grey round area) with grating couplers (orange rectangular area); the top is the PDMS flow cell. (b) A picture of the fabricated device. (c) PSi waveguide integrated with the flow cell geometry used for Equation (4.1)~(4.6). (d) A single pore cross-section geometry (axially symmetric) used for finite element simulations with COMSOL.

First, assume the rate of molecules entering into PSi is unlimited, which means when a molecule arrive at the inlet of PSi, it is absorbed inside the pores

immediately. This can be treated as the perfect sink condition, e.g. *c(y=0,t)=0* [155]. Combining the perfect sink boundary condition with Equations (4.1)-(4.4), the molecule surface concentration *Γ*, which denotes the molecule interactions in PSi, can be obtained after a simple math calculation (here it is assumed that molecular distribution is uniform inside the pores):

$$\Gamma(t) = 2c_b \cdot \sqrt{\frac{Dt}{\pi}} \cdot \frac{S_{inlet}}{S_{PSi}} \tag{4.5}$$

where S_{inlet} is the pore entry area, and S_{PSi} is the overall internal surface area of a single pore. From Equation (4.5), it can be seen that the diffusion dominates in the mass balance process.

For a second circumstance, when molecular binding in the PSi is very slow and the molecules inside the pores are saturated, the volume concentration within the pores is approximately equal to the volume outside, resulting in zero diffusion. Therefore, a stationary layer of molecules with concentration c_b is established near the top of the PSi film, e.g. $c(y=0,t) = c_b$. With this boundary condition, the molecule surface concentration *Γ* can be solved as:

$$\Gamma(t) = \Gamma_{\max} \cdot \frac{k_{ad} \cdot c_b}{k_{ad} \cdot c_b + k_{des}} \cdot \left\{1 - \exp\left[-\left(k_{ad} \cdot c_b + k_{des}\right) \cdot t\right]\right\} \cdot \frac{S_{inlet}}{S_{PSi}} \tag{4.6}$$

For this circumstance, adsorption and desorption of molecules on the internal surfaces of the pores dominate the mass balance process. Again, Equation (4.6) assumes a uniform distribution inside the pore.

During the actual mass transport process in PSi, molecular dynamics cannot be simply classified into one of the two ideal circumstances described previously. At the beginning of the process, however, molecular transport by

diffusion is very rapid, and the molecules within the pores are adsorbed to the surface quickly which can be described as the diffusion-dominated process. As time progresses, the diffusion of molecules into the pore becomes slow. The process therefore tends towards the second circumstance. Thus, the above two analytical results are suitable to describe the initial and long-time processes, and allow for preliminary estimation of the diffusion coefficient, as well as the adsorption and desorption rate constants. To fill the gap between the two extreme circumstances, the commercial software COMSOL is used to setup an axially symmetric model (Figure 4.1(d)) to simulate the biomolecule diffusion and attachment process in a single pore: the pore in the upper region (the waveguide layer) is 10 nm in radius, 200 nm thick; for the lower region (the substrate layer), the radius is 11.7 nm, and the thickness is 1500 nm; a fluidic domain outside the pore (modeling the flow cell, not shown in Figure 4.1(d)) is 100 μm in height. In the following sections, the parameters calculated from Equation (4.5) and (4.6), which give good agreement with the COMSOL numerical simulation employed, will be shown.

4.2 Fabrication

The fabricated biosensor is composed of two components. One is a PSi waveguide sample, which is similar to the all-PSi grating-coupled waveguide structure introduced in chapter III. PSi films were fabricated by electrochemical etching of silicon (p-type, 0.01 Ω·cm) in a 15% ethanolic hydrofluoric acid based electrolyte. The two-layer PSi waveguide structure was produced by applying

current density 5 mA/cm^2 for 80 s and 48 mA/cm^2 for 53 s in sequence, followed by a 30 min soak in 1.5 mmol·L^{-1} KOH to widen the pore opening and 500°C oxidation for 5 min to form a thin SiO_2 layer on the surface. A 300 nm film of PMMA 950 photoresist was spun onto each PSi waveguide and exposed by a Raith eLINE electron beam lithography tool to form a diffraction grating with a grating period of 1350 nm. After development, the PSi waveguide with PMMA gratings was reactive ion etched (Trion Phantom II) with 30 sccm SF_6 under 100 W RF power and 30 mTorr chamber pressure for 70 s. The remaining PMMA was removed by acetone.

The second component of the device is a PDMS flow cell. It is fabricated using standard soft-lithography techniques [157] with replica molding PDMS (Ellsworth Adhesives, Germantown, WI). The mold was created using a photo-sensitive material (SU-8 2100, MicroChem, MA) patterned through a transparent photomask and positioned over a silicon wafer [158]. A pre-polymer solution of PDMS was then mixed with a curing agent at a 10:1 weight ratio and poured over the mold. After degassing, the PDMS layer was allowed to solidify over the mold at 70^{o}C for 2 h. The solidified layer of PDMS was then peeled from its mold, and a sharp metal puncher was used to generate holes for the media wells. As shown in Figure 4.1(a), the dimensions of the flow channel are 10 × 4 × 0.2 mm.

A thin layer of curing agent as glue was used to bond the PDMS flow cell to the silicon wafer [159]. A glass coverslip as the carrier substrate was spin coated with the curing agent at 5000 rpm. After the surfaces were treated with oxygen plasma, the PDMS was stamped onto the curing agent coated coverslip.

Subsequently, PDMS was aligned and transferred onto the silicon wafer with the PSi. The integrated sample was secured by a mechanical clamp and then baked at 70^{o}C overnight to generate a permanent bonding between the PDMS flow cell and the silicon wafer. The biosensor system was completed by attaching two microbore tubes (Cole-Parmer, Vermon Hills, IL) to the punched holes (Figure 4.1(b)).

4.3 NaCl solution measurement

Different concentrations of NaCl solutions were injected into the flow cell integrated biosensor to test its performance. The flow cell-bonded PSi biosensor was mounted in a Metricon Model 2010/M to monitor the angular interrogated reflectance in real-time. Deionized water (DI water, representing the 0% NaCl solution) was first injected into the flow cell to be used for reference. Then, 1%, 2%, 3%, 5%, 7.5% and 10% NaCl solutions were injected in sequence. Reflectance spectra were measured every 90 sec. The time resolution was limited by the speed of the rotation stage in scanning from 0-45^{o}. DI water was re-injected after the 10% NaCl solution to verify that the system returned to the original, solute-free status.

Figure 4.2(a) shows the resonance angle shifts during each injection. Because the higher concentration solutions have larger refractive indices, the resonance angle shift becomes larger as the concentration increases. The return of the resonance angle to the initial position at the end of the experiment after reintroducing a pure DI water solution demonstrates that there is no permanent

adsorption of NaCl on the pore walls and that the biosensor is stable during the ~2 hour process. Since the diffusion of NaCl is very rapid immediately after injection of a different concentration NaCl solution, the response time of the biosensor is lower than the interval time of the measurement, resulting in discontinuous resonance angles changes after each injection. Figure 4.2(b) gives the relation between the resonance angle shifts and the NaCl concentration. The sensitivity of the biosensor is calculated to be approximately 37°/RIU based on this linear relationship. Note that this value is slightly lower than that reported in chapter III, in part due to the reduced index contrast between the waveguide film and cover/substrate regions.

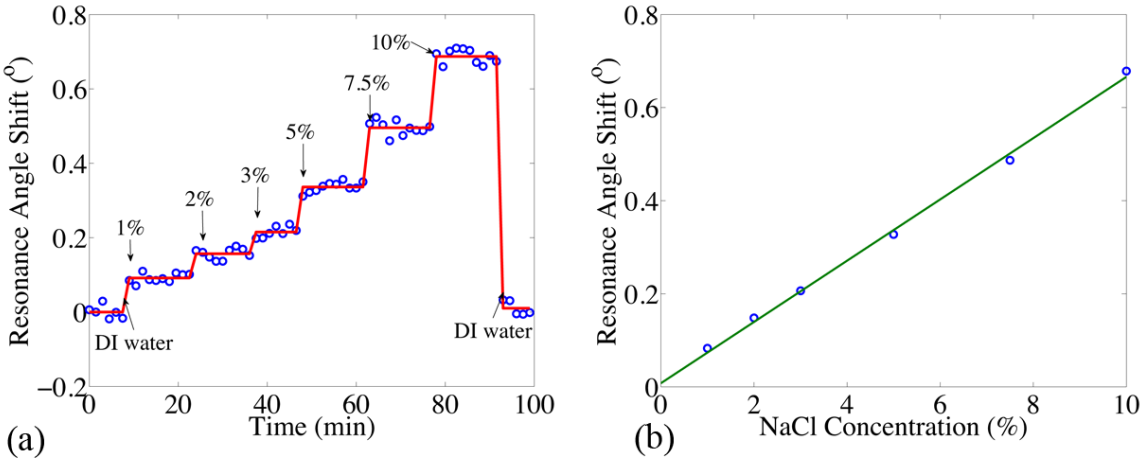

Figure 4. 2 (a) Resonance angle positions during the injections of 0%, 1%, 2%, 3%, 5%, 7.5% and 10% NaCl solutions. The blue circles are experimental data, and the red lines are the average value of each concentration and drawn as visual guides. (b) The relation between NaCl concentrations and resonance angle shifts with a linear fit shown. The typical variation in the resonance angle shift for each data point is ± 0.005°.

4.4 Biomolecule kinetics in PSi

Kinetics parameters of several kinds of biomolecules were measured during the DNA hybridization process. Complete details of the process are same to the functionalization procedure in chapter II. In this work, all solutions were injected into the flow cell to achieve PSi functionalization. First, 3-APTES and Sulfo-SMCC were injected and attached to the oxidized PSi waveguide. After that, the integrated PSi biosensor is heated by a back-attached silicone rubber fiberglass insulated flexible heater (OMEGALUX®, Omega Engineering, Inc.) to 37^{o}C. Then, 100 μmol·L-1 of 16-base thiol modified probe DNA (5'-TAG CTA TGG TCC TCG T-3', 3' Thiol C3, Eurofins MWG Operon) oligos is injected and bound to the modified surface. Complementary peptide nucleic acid (PNA, ACG AGG ACC ATA GCT A, BioSynthesis) is chosen as the target molecule and is used with the same concentration as the probe DNA. HEPES buffer and DI water were injected between each molecular step to clean the flow cell and the sample surface. Angular reflectance spectra were measured by the prism coupler during the binding processes every 75 s, which was determined by the 0-37.5^{o} scan range.

The time-dependent change in the waveguide resonance angle during injection of the 3-APTES solution is shown in Figure 4.3(a). Within the first ~2 min, the resonance angle increases significantly as the methanol/DI water mixture inside the PSi is rapidly replaced by the 4% 3-APTES solution, which has a greater refractive index. Diffusion dominates the mass balance process during this interval, and the perfect sink condition can therefore be assumed.

Accordingly, the diffusion coefficient of 3-APTES in PSi environment is calculated to be 5.41×10^{-9} $m^2\cdot s^{-1}$ from Equation (4.5). After this short period, the rate of the change of the resonance angle decreases in magnitude. At long time periods, slow adsorption on the PSi pore walls dictates the reflectance changes and, therefore, Equation (4.6) provides an appropriate fit to the experimental data during this time, from 2-25 min. The adsorption and desorption rate constants of 3-APTES in PSi were calculated to be 0.02958 $M^{-1}\cdot s^{-1}$ and 7.652×10^{-5} s^{-1}, respectively. For comparison, an experiment was conducted to monitor the 3-APTES binding process on a flat silicon surface using a laser reflectometry approach that is fully described in Ref. [160]. The experimental result is shown in Figure 4.3(b), in which the surface coverage Γ/Γ_{max} change denotes the 3-APTES binding process. With the same concentration of 3-APTES solution as was introduced to the PSi waveguide, nearly complete 3-APTES coverage on the surface is achieved in approximately 10 s, which translates into an adsorption rate constant k_{ad} = 2.826 $M^{-1}\cdot s^{-1}$ and desorption rate constant k_{des} = 8.5×10^{-4} s^{-1}. The adsorption rate constant of 3-APTES on a flat surface is about 100 times greater than that in PSi, which is consistent with a previous report of avidin adsorption in anodic aluminum oxide [155]. The reason for the substantial discrepancy between the adsorption rate constants of flat surface and porous material is not entirely clear at this time. It is hypothesized, however, that compared to the flat surface, the steric and electrostatic hindrance present for biomolecules on the pore walls, slows the biomolecule interactions inside the PSi film [161, 162].

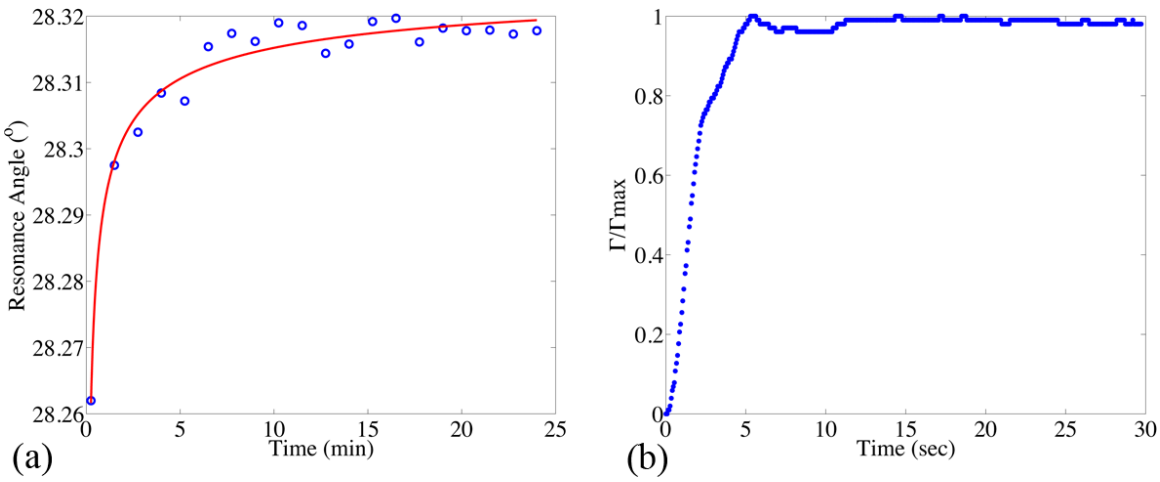

Figure 4. 3 (a) Resonance angle shifts of integrated PSi waveguide biosensor during the injection of 3-APTES. The fitted curve is shown for visual guidance. (b) Time dependent change of 3-APTES surface coverage upon binding to a flat silicon surface.

Using the same method, the diffusion coefficient, adsorption rate constant, and desorption rate constant of Sulfo-SMCC, probe DNA and antisense PNA were calculated by Equation (4.5) and (4.6). The results are summarized in Table 4.1. For small linkers, the diffusion coefficient is on the order of 10^{-9} $m^2 \cdot s^{-1}$, and the adsorption rate constant is in the range of 10^{-1}-10^{-2} $M^{-1} \cdot s^{-1}$. For the larger oligos, the diffusion coefficient in PSi is on the order of 10^{-11} $m^2 \cdot s^{-1}$, which is nearly 10^1-fold smaller than that in free solution [163, 164]. The adsorption rate constant of DNA hybridization is near 10^1 $M^{-1} \cdot s^{-1}$, which is 10^2-10^4 times smaller than that on flat surface [161, 165]. Applying these parameters into the COMSOL simulation, biomolecule attachment processes were simulated. Figure 4.4 shows both the COMSOL simulation and the experimentally normalized resonance angle changes during 3-APTES, Sulfo-SMCC, probe DNA and antisense PNA

binding. The resonance angle changes proportionally with both the surface coverage of the molecules bound in the pores and the refractive index change of the free solution in the pore. As expected, the resonance angle increases in all cases over time. It is expected that a saturation behavior for the larger oligos would be observed at longer time scales. The experimental and simulation results show comparatively good agreement with each other, which suggests that the assumptions of Equation (4.5) and (4.6) are valid and can be applied for deriving kinetic parameters of molecules in nanoscale pores.

Table 4. 1 Diffusion coefficient, adsorption and desorption rate constants of 3-APTES, Sulfo-SMCC, probe DNA and antisense PNA in PSi.

	3-APTES	Sulfo-SMCC	Probe DNA	Antisense PNA
D ($m^2 \cdot s^{-1}$)	5.41×10^{-9}	2.442×10^{-9}	9.542×10^{-11}	9.576×10^{-11}
k_{ad} ($M^{-1} \cdot s^{-1}$)	0.02958	0.1274	5.641	4.442
k_{des}(s^{-1})	7.652×10^{-5}	1.748×10^{-5}	7.4×10^{-6}	1.422×10^{-5}

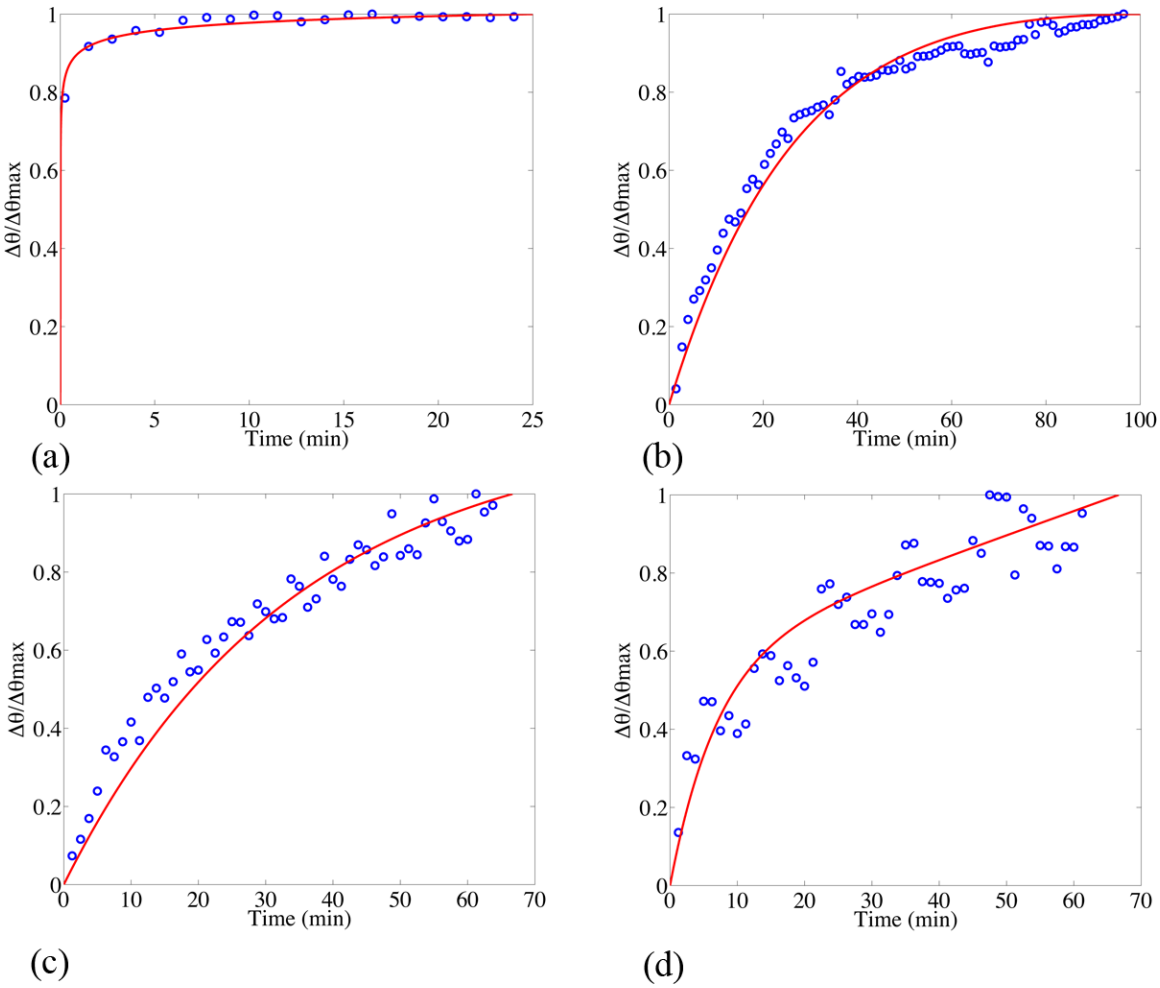

Figure 4. 4 Experimental (blue circle) and COMSOL simulated (red line) normalized resonance angle changes during (a) 3-APTES, (b) Sulfo-SMCC, (c) probe DNA and (d) antisense PNA binding.

4.5 Conclusion

The PDMS flow cell integrated grating-coupled PSi waveguide biosensor is demonstrated as a platform for near real-time detection of chemical and biological molecule binding events. Molecular attachments in the PSi waveguide are monitored by angle-resolved reflectance measurements. Precise and simplified mass balance equations, which reveal the binding events inside the pores, are given. Diffusion coefficient, adsorption and desorption rate constants

of different sized chemical linker and nucleic acid molecules are determined based on the changes of the measured resonance angle. For small linkers, the diffusion coefficient is on the order of 10^{-9} $m^2 \cdot s^{-1}$, and the adsorption rate constant in the range of 10^{-1}- 10^{-2} $M^{-1} \cdot s^{-1}$, while for the larger oligos, the diffusion coefficient is on the order of 10^{-11} $m^2 \cdot s^{-1}$, and the adsorption rate constant is near 10^{1} $M^{-1} \cdot s^{-1}$. Based on the experimental and calculated results, the PDMS flow cell integrated grating-coupled PSi waveguide shows great promise for sensitive, real-time detection of small chemical and biological molecules.

CHAPTER V

CONCLUSIONS AND FUTURE WORK

5.1 Conclusions and research contribution

Sensitive label-free optical biosensors based on grating-coupled PSi waveguides are demonstrated for biosensing applications. This is the first time that the benefits of both PSi and diffraction gratings have been combined for the detection of small molecules. The use of a grating coupler instead of a prism coupler allows the device to be more compact. The large surface area available for biomolecular attachment and strong field confinement in the waveguide region where biomolecules are immobilized make it possible to detect biomolecule interactions with high sensitivity in the PSi waveguide. Two kinds of gratings were presented on PSi waveguides for the first time: photoresist gratings and all-PSi gratings (fabricated by both electron beam lithography and DIPS stamping). The photoresist grating-coupled PSi waveguide biosensor and the DIPS grating-coupled PSi waveguide biosensor possess an easier fabrication process and were shown to be capable of detecting small biomolecules. Due to its enhanced available surface area for molecular binding in regions of strong field localization, the electron beam lithography-fabricated all-PSi grating-coupled waveguide biosensor was shown to be the most highly efficient biosensor. Theoretical simulations demonstrated that all-PSi grating-coupled waveguides support a 32-fold higher field distribution in regions where molecules can bind

compared to a planar grating-coupled SOI waveguide biosensor, and a 2-fold higher field distribution compared to the photoresist grating-coupled PSi waveguide biosensor. PNA-DNA hybridization experiments were carried out by measuring angular resonance changes. Negligible shift was measured for exposure to non-complementary DNA. The detection sensitivity of the all-PSi grating-coupled waveguide for small molecules is approximately 42°/RIU, and the PNA detection limit is on the order of 1 μM. A PDMS micro-channel was integrated with the all-PSi grating-coupled waveguide biosensor to form a near real-time detection platform. Diffusion coefficients as well as adsorption and desorption rate constants of different sized chemical linker and nucleic acid molecules were determined based on the changes of the measured resonance angle after exposure to the molecules. For small linkers, the diffusion coefficient is on the order of 10^{-9} $m^2 \cdot s^{-1}$, and the adsorption rate constant is in the range of 10^{-1}- 10^{-2} $M^{-1} \cdot s^{-1}$, while for the larger oligos, the diffusion coefficient is on the order of 10^{-11} $m^2 \cdot s^{-1}$, and the adsorption rate constant is near 10^{1} $M^{-1} \cdot s^{-1}$. The adsorption rate constants, which are 10^{2}- 10^{4} smaller than that of flat surface attachment, are greatly affected by the porous structure.

5.2 Future research opportunities

The basic characteristics and applications of PSi waveguide biosensors with grating couplers have been studied. In order to achieve improved performance, research could be continued in the following areas:

1) In-situ DNA synthesis

In the current DNA hybridization experiments, pre-synthesized DNA oligonucleotides, used as the probes, are directly infiltrated into pores and attached to the pore walls. However, due to the large probe DNA size (~3.5 nm) which is on the same order of the pore radius (~10nm), and the steric and electrostatic hindrance present in biomolecule films on the pore walls, which suppresses the probe attachment inside the PSi, the probe DNA coverage is very low, ~10%. Therefore, the resonance angle shifts when probe DNAs were attached are very small compared to the shifts of 3-APTES and Sulfo-SMCC. To increase the probe density and sequentially enhance the biosensor sensitivity, in-situ DNA synthesis could be applied, as has been performed on prism-coupled PSi biosensors. The probe DNA chain is formed inside the pores base by base using the in situ synthesis technique. Because of the small size of a single base, it can easily infiltrate into the pores and substantially raise the probe DNA coverage in a controllable manner up to 50% [134]. Furthermore, in-situ DNA synthesis also allows for flexibility in defining the probe sequence, which is convenient in practical applications.

2) Desorption process measurement

The PDMS flow cell integrated all-PSi waveguide biosensor is certified to be feasible for DNA hybridization detection. Several biomolecular kinetics parameters were obtained based on the adsorption process in chapter IV. However, the investigation on adsorption kinetics is not complete. The process of biomolecular attachment in PSi is complicated. It depends not only on the surface adsorption, but also on mass transport in porous media. Therefore, the

desorption process needs to be investigated to get a full picture of biomolecule binding events in nanoscale pores. Moreover, desorption kinetics bear much richer physics information in biochemistry studies [155]. For the current DNA hybridization biosensor, a special desorption solution is demanded to be found and used in the desorption process. An alternative way is using a temperature controlled system, which can manage the fluid temperature inside the PDMS flow cell. For 16-mer PNA, a 70^{o}C buffer rinse should be sufficient to break the DNA-PNA bonds, but binding between 3-APTES and Sulfo-SMCC may not be stable at this temperature. Thus, new linkers/cross-linkers should be investigated and applied during the desorption measurement.

3) Bloch surface wave biosensor

An alternate form of a guided mode sensor, called a Bloch surface wave sensor, may enable effective detection of large molecules on the surface of a PSi film while still maintaining sensitive detection of small molecules inside the film. Bloch surface waves are electromagnetic modes propagating at the interface between a homogeneous medium and a truncated periodic structure like a dielectric monodimensional photonic crystal [166]. At the resonance condition, an electromagnetic field is confined to the surface of the structure due to the photonic band gap. The strong field confinement at the surface gives the BSW biosensor the advantage of quickly detecting molecules that attach to the surface. Prism coupled BSW biosensors fabricated by silicon nitride, PSi, and tantalum pentoxide have been demonstrated in gas, fluid and biomolecule detections [167-169]. In order to create a more compact biosensor, the prism can be replaced by

a grating coupler to generate the BSW (Figure 5.1). Compared to a PSi waveguide sensor, the most significant advantage of a PSi BSW sensor is that the confined optical mode located adjacent to the surface is suitable for sensing large biomolecules, such as proteins and nucleic acid [167], which could only be detected through a leaky mode or weak evanescent field using a PSi waveguide. However, there would likely be a trade-off on the speed and sensitivity of detecting small molecules, which are likely to be more effectively detected using a waveguide geometry. . Moreover, field intensity distribution calculations need to be conducted to determine the true advantage of the BSW over a leaky waveguide for large molecule surface sensing.

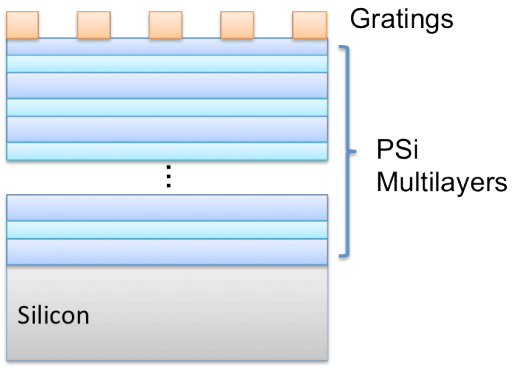

Figure 5.1 Schematic of BSW biosensor with a grating coupler.

4) Membrane PSi waveguide structure

In Chapter 4, kinetics parameters of several types of biomolecules were investigated by the flow cell integrated grating-coupled PSi waveguide biosensor. Compared to molecular attachment on a flat surface, the adsorption rate constants of molecules are affected by the nanoscale porous structure. To

maintain the high sensitivity of PSi waveguide biosensors and improve the binding kinetics, utilizing a PSi waveguide membrane is a reasonable choice. As shown in Figure 5.2, gratings and PSi waveguide film could be fabricated by electrochemical etching and lithography techniques. The silicon substrate can be etched away from the backside such that air serves as the cover layer and the substrate layer. The membrane structure enhances the refractive index contrast and increases the waveguide field confinement, resulting in a possibility of higher sensitivity. Furthermore, opening both sides of the PSi film to form a membrane allows a constant flow of analyte to be sustained from one side to the other. It is also possible to apply an electric or magnetic field to enhance the flow rate of charged ions or biomolecules. The mechanical properties of the PSi membrane will need to be considered during the preliminary design process to ensure robustness and the gratings will also require design modification in the new experimental environment.

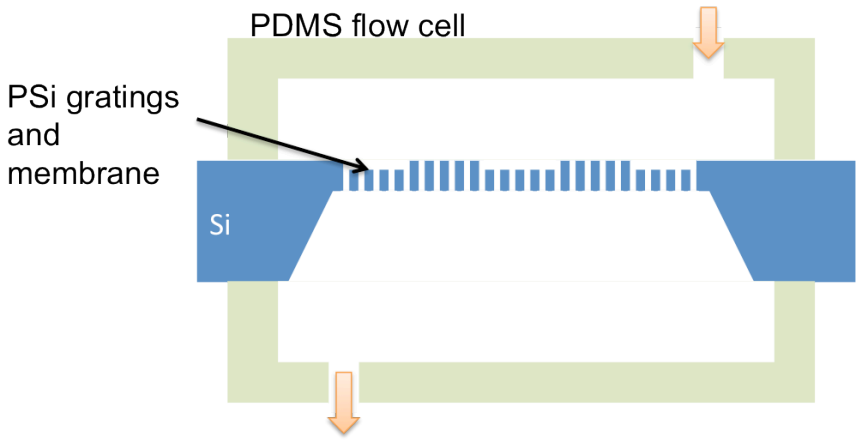

Figure 5.2 Schematic of PDMS flow cell integrated PSi membrane waveguide biosensor with a grating coupler.

5) Portable biosensors

The final goal of this PSi grating waveguide structure study is to make a point-of-care instrument which can facilitate convenient and rapid diagnoses. However, the angular interrogation applied in this work, which has a high cost rotation stage and is time-consuming, is not very appropriate for a portable system. The schematic of an ideal PSi based biosensor is shown in Figure 5.3. It contains a white light LED used as the light source, a sensor chip based on a PSi waveguide with a grating coupler, and a color CCD camera, which can detect the reflectance spectra in a wide wavelength range. When biomolecule interactions take place on the sensor chip, the reflectance spectra is changed. This change is monitored by the color CCD camera and the corresponding bio-information can be extracted.

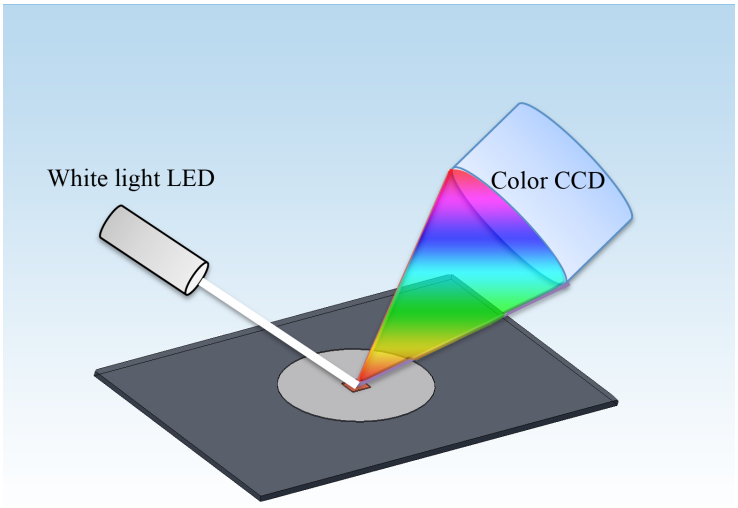

Figure 5.3 Schematic of an ideal portable biosensor based on PSi waveguide with a grating coupler structure.

APPENDIX A

MULTI-LAYER REFLECTANCE VS. INCIDENT ANGLE MATLAB CALCULATION CODE

```
clc;clear;
lamda=1550e-9;%1550nm
m=7;
n=zeros(1,m);
n(1)=2.1252;
n(2)=1;
n(3)=1.8;
n(4)=1.21;
n(5)=3.4784+0.00001233*i;
n(6)=3.4784+0.00001233*i;
n(7)=3.4784+0.00001233*i;
t=zeros(1,m);
t(2)=700e-9;
t(3)=340e-9;
t(4)=1500e-9;
t(5)=0e-9;
t(6)=0e-9;
thata=zeros(1,m);
q=1;
for p=1:0.01:90
   thata(1)=p/180*pi;
   for k=2:m
      thata(k)=asin(n(1)*sin(thata(1))/n(k));
   end
   phi=zeros(1,m-1);
   for j=1:m-1
      phi(j)=2*pi/lamda*n(j)*t(j)*cos(thata(j));
   end
   r=zeros(m,m);
   for j=1:m-1
      %TE
      r(j,j+1)=(n(j)*cos(thata(j))-…
n(j+1)*cos(thata(j+1)))/(n(j)*cos(thata(j))+n(j+1)*cos(thata(j+1)));
      %TM
      %r(j,j+1)=(n(j+1)*cos(thata(j))-…
n(j)*cos(thata(j+1)))/(n(j+1)*cos(thata(j))+n(j)*cos(thata(j+1)));
   end
   r567=(r(5,6)+r(6,7)*exp(-2*i*phi(6)))/(1+r(5,6)*r(6,7)*exp(-2*i*phi(6)));
   r4567=(r(4,5)+r567*exp(-2*i*phi(5)))/(1+r(4,5)*r567*exp(-2*i*phi(5)));
   r34567=(r(3,4)+r4567*exp(-2*i*phi(4)))/(1+r(3,4)*r4567*exp(-2*i*phi(4)));
   r234567=(r(2,3)+r34567*exp(-2*i*phi(3)))/(1+r(2,3)*r34567*exp(-2*i*phi(3)));
   r1234567=(r(1,2)+r234567*exp(-2*i*phi(2)))/(1+r(1,2)*r234567*exp(-2*i*phi(2)));
   R(q)=abs(r1234567)^2;
   q=q+1;
end
plot(1:0.01:90,R)
```

APPENDIX B

MULTI-LAYER REFLECTANCE VS. WAVELENGTH MATLAB CALCULATION CODE

```
clc;clear;
%lamda=1550e-9;%1550nm
m=7;
n=zeros(1,m);
n(1)=1;
n(2)=1.8;
n(3)=1.2;
n(4)=3.4784+0.00001233*i;
n(5)=3.4784+0.00001233*i;
n(6)=3.4784+0.00001233*i;
n(7)=3.4784+0.00001233*i;
t=zeros(1,m);
t(2)=340e-9;
t(3)=1500e-9;
t(4)=0e-9;
t(5)=0e-9;
t(6)=0e-9;
thata=zeros(1,m);
q=1;
for lamda=500e-9:1e-9:2000e-9
   %thata(1)=/180*pi;
   for k=2:m
      thata(k)=asin(n(1)*sin(thata(1))/n(k));
   end
   phi=zeros(1,m-1);
   for j=1:m-1
      phi(j)=2*pi/lamda*n(j)*t(j)*cos(thata(j));
   end
   r=zeros(m,m);
   for j=1:m-1
      %TE
      r(j,j+1)=(n(j)*cos(thata(j))-
n(j+1)*cos(thata(j+1)))/(n(j)*cos(thata(j))+n(j+1)*cos(thata(j+1)));
      %TM
      %r(j,j+1)=(n(j+1)*cos(thata(j))-
n(j)*cos(thata(j+1)))/(n(j+1)*cos(thata(j))+n(j)*cos(thata(j+1)));
   end
r567=(r(5,6)+r(6,7)*exp(-2*i*phi(6)))/(1+r(5,6)*r(6,7)*exp(-2*i*phi(6)));
   r4567=(r(4,5)+r567*exp(-2*i*phi(5)))/(1+r(4,5)*r567*exp(-2*i*phi(5)));
   r34567=(r(3,4)+r4567*exp(-2*i*phi(4)))/(1+r(3,4)*r4567*exp(-2*i*phi(4)));
   r234567=(r(2,3)+r34567*exp(-2*i*phi(3)))/(1+r(2,3)*r34567*exp(-2*i*phi(3)));
   r1234567=(r(1,2)+r234567*exp(-2*i*phi(2)))/(1+r(1,2)*r234567*exp(-2*i*phi(2)));
   R(q)=abs(r1234567)^2;
   q=q+1;
end
plot(500:2000,R)
```

APPENDIX C

WAVEGUIDE ELECTRICAL FIELD DISTRIBUTION MATLAB CALCULATION CODE

```
nf=1.8;
ns=1.21;
nc=1;
hf=0.60;
lamda=1.55;
k=2*pi/lamda;

kappamax=sqrt(k^2*nf^2-k^2*ns^2);
kappa=0:0.00001:kappamax;
beta=sqrt(k^2*nf^2-kappa.^2);
gammas=sqrt(beta.^2-k^2*ns^2);
gammac=sqrt(beta.^2-k^2*nc^2);
left=tan(kappa*hf);
right=(gammas+gammac)./(kappa.*(1-gammas.*gammac./kappa.^2));
subplot(2,1,1)
plot(kappa,left,kappa,right)
ylim([-10 10])
N=find(abs(left-right)<0.0001);
n=N(end);
kappa0=kappa(n);
gammac0=gammac(n);
gammas0=gammas(n);

x1=0:0.001:1;
E1=exp(-gammac0*x1);
x2=-hf:0.001:0;
E2=cos(kappa0*x2)-(gammac0/kappa0)*sin(kappa0*x2);
x3=-(hf+1.5):0.001:-hf;
E3=(cos(kappa0*hf)+(gammac0/kappa0)*sin(kappa0*hf))*exp(gammas0*(x3+hf));
subplot(2,1,2)
plot(x1,E1,x2,E2,x3,E3)
sum(E2.^2)/(sum(E1.^2)+sum(E2.^2)+sum(E3.^2))
```

REFERENCES

1. J. S. Schultz, *Biosensing : international research and development* (Springer, Dordrecht, 2006).

2. B. R. Eggins and Knovel (Firm), "Chemical sensors and biosensors," in *Analytical techniques in the sciences,* (J. Wiley, Chichester ; Hoboken, NJ, 2002).

3. T. Vo-Dinh, *Biomedical photonics handbook* (CRC Press, Boca Raton, Fla., 2003).

4. H. M. Haake, A. Schutz, and G. Gauglitz, "Label-free detection of biomolecular interaction by optical sensors," Fresenius J. Anal. Chem. **366**, 576-585 (2000).

5. M. A. Cooper, *Label-free biosensors : techniques and applications* (Cambridge University Press, Cambridge ; New York, 2009).

6. X. D. Fan, I. M. White, S. I. Shopova, H. Y. Zhu, J. D. Suter, and Y. Z. Sun, "Sensitive optical biosensors for unlabeled targets: A review," Anal. Chim. Acta **620**, 8-26 (2008).

7. B. Liedberg, C. Nylander, and I. Lundstrom, "Surface-Plasmon Resonance for Gas-Detection and Biosensing," Sens. Actuators **4**, 299-304 (1983).

8. J. Homola, S. S. Yee, and G. Gauglitz, "Surface plasmon resonance sensors: review," Sens. Actuators, B **54**, 3-15 (1999).

9. A. K. Sharma, R. Jha, and B. D. Gupta, "Fiber-optic sensors based on surface plasmon resonance: A comprehensive review," IEEE Sens. J. **7**, 1118-1129 (2007).

10. X. D. Hoa, A. G. Kirk, and M. Tabrizian, "Enhanced SPR response from patterned immobilization of surface bioreceptors on nano-gratings," Biosens. Bioelectron. **24**, 3043-3048 (2009).

11. F. J. Blanco, M. Agirregabiria, J. Berganzo, K. Mayora, J. Elizalde, A. Calle, C. Dominguez, and L. M. Lechuga, "Microfluidic-optical integrated CMOS compatible devices for label-free biochemical sensing," J. Micromech. Microeng. **16**, 1006-1016 (2006).

12. S. H. Hsu and Y. T. Huang, "A novel Mach-Zehnder interferometer based on dual-ARROW structures for sensing applications," J. Lightwave Technol. **23**, 4200-4206 (2005).

13. F. Prieto, B. Sepulveda, A. Calle, A. Llobera, C. Dominguez, and L. M. Lechuga, "Integrated Mach-Zehnder interferometer based on ARROW structures for biosensor applications," Sens. Actuators, B **92**, 151-158 (2003).

14. A. Ymeti, J. S. Kanger, J. Greve, G. A. J. Besselink, P. V. Lambeck, R. Wijn, and R. G. Heideman, "Integration of microfluidics with a four-channel integrated optical Young interferometer immunosensor," Biosens. Bioelectron. **20**, 1417-1421 (2005).

15. G. H. Cross, A. A. Reeves, S. Brand, J. F. Popplewell, L. L. Peel, M. J. Swann, and N. J. Freeman, "A new quantitative optical biosensor for protein characterisation," Biosens. Bioelectron. **19**, 383-390 (2003).

16. G. H. Cross, A. Reeves, S. Brand, M. J. Swann, L. L. Peel, N. J. Freeman, and J. R. Lu, "The metrics of surface adsorbed small molecules on the Young's fringe dual-slab waveguide interferometer," J. Phys. D: Appl. Phys. **37**, 74-80 (2004).

17. B. H. Schneider, E. L. Dickinson, M. D. Vach, J. V. Hoijer, and L. V. Howard, "Optical chip immunoassay for hCG in human whole blood," Biosens. Bioelectron. **15**, 597-604 (2000).

18. V. S. Y. Lin, K. Motesharei, K. P. S. Dancil, M. J. Sailor, and M. R. Ghadiri, "A porous silicon-based optical interferometric biosensor," Science **278**, 840-843 (1997).

19. C. L. Chang, G. Acharya, and C. A. Savran, "In situ assembled diffraction grating for biomolecular detection," Appl. Phys. Lett. **90**, 233901 (2007).

20. D. J. Bornhop, J. C. Latham, A. Kussrow, D. A. Markov, R. D. Jones, and H. S. Sorensen, "Free-solution, label-free molecular interactions studied by back-scattering interferometry," Science **317**, 1732-1736 (2007).

21. R. Cush, J. M. Cronin, W. J. Stewart, C. H. Maule, J. Molloy, and N. J. Goddard, "The Resonant Mirror - a Novel Optical Biosensor for Direct Sensing of Biomolecular Interactions .1. Principle of Operation and Associated Instrumentation," Biosens. Bioelectron. **8**, 347-353 (1993).

22. A. J. T. George, R. R. French, and M. J. Glennie, "Measurement of Kinetic Binding Constants of a Panel of Anti-Saporin Antibodies Using a Resonant Mirror Biosensor," J. Immunol. Methods **183**, 51-63 (1995).

23. J. D. Huang, X. M. Zhang, X. R. He, Q. Lin, X. R. Xing, K. Du, W. J. Lian, H. Zhu, T. Osa, and Q. Chen, "Real-Time Kinetic Analysis of Interaction Between Interleukin-2 (IL-2) and Soluble Interleukin-2 Receptor (sIL-2R) Using a Resonant Mirror Optical Biosensor," Sens. Lett. **9**, 485-490 (2011).

24. K. Hotta, A. Yamaguchi, and N. Teramae, "Properties of A Metal Clad Waveguide Sensor Based on A Nanoporous-Metal-Oxide/Metal Multilayer Film," Anal. Chem. **82**, 6066-6073 (2010).

25. J. P. Hulme, N. J. Goddard, and C. Lu, "Simple leaky-waveguide devices for the detection of bacterial spores," Sens. Actuators, B **160**, 1508-1513 (2011).

26. M. Zourob, S. Mohr, B. J. T. Brown, P. R. Fielden, M. McDonnell, and N. J. Goddard, "The development of a metal clad leaky waveguide sensor for the detection of particles," Sens. Actuators, B **90**, 296-307 (2003).

27. E. Krioukov, J. Greve, and C. Otto, "Performance of integrated optical microcavities for refractive index and fluorescence sensing," Sens. Actuators, B **90**, 58-67 (2003).

28. N. M. Hanumegowda, C. J. Stica, B. C. Patel, I. White, and X. D. Fan, "Refractometric sensors based on microsphere resonators," Appl. Phys. Lett. **87**, 201107 (2005).

29. H. Y. Zhu, I. M. White, J. D. Suter, P. S. Dale, and X. D. Fan, "Analysis of biomolecule detection with optofluidic ring resonator sensors," Opt. Express **15**, 9139-9146 (2007).

30. Y. Z. Sun and X. D. Fan, "Optical ring resonators for biochemical and chemical sensing," Anal. Bioanal.Chem. **399**, 205-211 (2011).

31. M. P. DeLisa, Z. Zhang, M. Shiloach, S. Pilevar, C. C. Davis, J. S. Sirkis, and W. E. Bentley, "Evanescent wave long period fiber Bragg grating as an immobilized antibody biosensor," Anal. Chem. **72**, 2895-2900 (2000).

32. J. Y. Lou, L. M. Tong, and Z. Z. Ye, "Modeling of silica nanowires for optical sensing," Opt. Express **13**, 2135-2140 (2005).

33. T. Wei, Y. K. Han, Y. J. Li, H. L. Tsai, and H. Xiao, "Temperature-insensitive miniaturized fiber inline Fabry-Perot interferometer for highly sensitive refractive index measurement," Opt. Express **16**, 5764-5769 (2008).

34. L. Rindorf, J. B. Jensen, M. Dufva, L. H. Pedersen, P. E. Hoiby, and O. Bang, "Photonic crystal fiber long-period gratings for biochemical sensing," Opt. Express **14**, 8224-8231 (2006).

35. E. Chow, A. Grot, L. W. Mirkarimi, M. Sigalas, and G. Girolami, "Ultracompact biochemical sensor built with two-dimensional photonic crystal microcavity," Opt. Lett. **29**, 1093-1095 (2004).

36. C. Kang, C. T. Phare, Y. A. Vlasov, S. Assefa, and S. M. Weiss, "Photonic crystal slab sensor with enhanced surface area," Opt. Express **18**, 27930-27937 (2010).

37. M. A. Cooper and V. T. Singleton, "A survey of the 2001 to 2005 quartz crystal microbalance biosensor literature: applications of acoustic physics to the analysis of biomolecular interactions," J. Mol. Recognit. **20**, 154-184 (2007).

38. Y. Y. Zhang and S. Tadigadapa, "Calorimetric biosensors with integrated microfluidic channels," Biosens. Bioelectron. **19**, 1733-1743 (2004).

39. A. Uhlir, "Electrolytic shaping of germanium and silicon," The Bell System Technical Journal **35**, 333-347 (1956).

40. Y. Watanabe and T. Sakai, "Semiconductor device and method of producing the same," US3640806 (1972).

41. Y. Watanabe, Y. Arita, T. Yokoyama, and Y. Igarashi, "Formation and Properties of Porous Silicon and Its Application," J. Electrochem. Soc. **122**, 1351-1355 (1975).

42. T. Unagami, "Formation Mechanism of Porous Silicon Layer by Anodization in Hf Solution," J. Electrochem. Soc. **127**, 476-483 (1980).

43. K. Imai, "A New Dielectric Isolation Method Using Porous Silicon," Solid-State Electron. **24**, 159-164 (1981).

44. "Science Citation Index Expanded", http://apps.isiknowledge.com/.

45. L. T. Canham, "Silicon Quantum Wire Array Fabrication by Electrochemical and Chemical Dissolution of Wafers," Appl. Phys. Lett. **57**, 1046-1048 (1990).

46. N. Koshida and H. Koyama, "Visible Electroluminescence from Porous Silicon," Appl. Phys. Lett. **60**, 347-349 (1992).

47. A. Richter, P. Steiner, F. Kozlowski, and W. Lang, "Current-Induced Light-Emission from a Porous Silicon Device," IEEE Electron Device Lett. **12**, 691-692 (1991).

48. T. Matsumoto, M. Daimon, H. Mimura, Y. Kanemitsu, and N. Koshida, "Optically Induced Absorption in Porous Silicon and Its Application to Logic Gates," J. Electrochem. Soc. **142**, 3528-3533 (1995).

49. J. P. Zheng, K. L. Jiao, W. P. Shen, W. A. Anderson, and H. S. Kwok, "Highly Sensitive Photodetector Using Porous Silicon," Appl. Phys. Lett. **61**, 459-461 (1992).

50. R. Herino, in *Properties of Porous Silicon*, L. T. Canham, ed. (IEE INSPEC, London, UK, 1997).

51. S. M. Weiss, "Biological applications of silicon nanostructures," in *Silicon nanophotonics : basic principles, present status and perspectives*, L. Khriachtchev, ed. (World Scientific distributor, Hackensack, NJ, 2009), pp. 425-448.

52. G. Rong, A. Najmaie, J. E. Sipe, and S. M. Weiss, "Nanoscale porous silicon waveguide for label-free DNA sensing," Biosens. Bioelectron. **23**, 1572-1576 (2008).

53. M. Qian, X. Q. Bao, L. W. Wang, X. Lu, J. Shao, and X. S. Chen, "Structural tailoring of multilayer porous silicon for photonic crystal application," J. Cryst. Growth **292**, 347-350 (2006).

54. L. A. DeLouise, P. M. Kou, and B. L. Miller, "Cross-correlation of optical microcavity biosensor response with immobilized enzyme activity. Insights into biosensor sensitivity," Anal. Chem. **77**, 3222-3230 (2005).

55. A. Jane, R. Dronov, A. Hodges, and N. H. Voelcker, "Porous silicon biosensors on the advance," Trends Biotechnol. **27**, 230-239 (2009).

56. V. P. Bondarenko, A. M. Dorofeev, and N. M. Kazuchits, "Optical Wave-Guide Based on Oxidized Porous Silicon," Microelectron. Eng. **28**, 447-450 (1995).

57. G. Maiello, S. LaMonica, A. Ferrari, G. Masini, V. P. Bondarenko, A. M. Dorofeev, and N. M. Kazuchits, "Light guiding in oxidised porous silicon optical waveguides," Thin Solid Films **297**, 311-313 (1997).

58. A. Loni, L. T. Canham, M. G. Berger, R. ArensFischer, H. Munder, H. Luth, H. F. Arrand, and T. M. Benson, "Porous silicon multilayer optical waveguides," Thin Solid Films **276**, 143-146 (1996).

59. M. Araki, H. Koyama, and N. Koshida, "Fabrication and fundamental properties of an edge-emitting device with step-index porous silicon waveguide," Appl. Phys. Lett. **68**, 2999-3000 (1996).

60. L. T. Canham, T. I. Cox, A. Loni, and A. J. Simons, "Progress towards silicon optoelectronics using porous silicon technology," Appl. Surf. Sci. **102**, 436-441 (1996).

61. H. F. Arrand, T. M. Benson, A. Loni, R. Arens-Fischer, M. Kruger, M. Thonissen, H. Luth, and S. Kershaw, "Novel liquid sensor based on porous silicon optical waveguides," IEEE Photonics Technol. Lett. **10**, 1467-1469 (1998).

62. H. F. Arrand, T. M. Benson, A. Loni, R. Arens-Fischer, M. G. Krueger, M. Thoenissen, H. Lueth, S. Kershaw, and N. N. Vorozov, "Solvent detection using porous silicon optical waveguides," J. Lumin. **80**, 119-123 (1998).

63. P. Rivolo, P. Pirasteh, A. Chaillou, P. Joubert, M. Kloul, J. F. Bardeau, and F. Geobaldo, "Oxidised porous silicon impregnated with Congo Red for chemical sensoring applications," Sens. Actuators, B **100**, 99-102 (2004).

64. P. Pirasteh, J. Charrier, Y. Dumeige, P. Joubert, S. Haesaert, A. Chaillou, L. Haji, P. Le Rendu, and T. P. Nguyen, "Light propagation and scattering in porous silicon nanocomposite waveguides," Phys. Status Solidi A **202**, 1712-1716 (2005).

65. J. J. Saarinen, S. M. Weiss, P. M. Fauchet, and J. E. Sipe, "Optical sensor based on resonant porous silicon structures," Opt. Express **13**, 3754-3764 (2005).

66. G. Rong, J. Saarinen, J. Sipe, and S. Weiss, "High Sensitivity Sensor Based on Porous Silicon Waveguide," Mat. Res. Soc. Symp. Proc. **934**, 64-69 (2006).

67. S. Weiss, "Porous silicon waveguide biosensors," IEEE LEOS, 310-311 (2006).

68. E. De Tommasi, L. De Stefano, I. Rea, V. Di Sarno, L. Rotiroti, P. Arcari, A. Lamberti, C. Sanges, and I. Rendina, "Porous Silicon Based Resonant Mirrors for Biochemical Sensing," Sensors **8**, 6549-6556 (2008).

69. K. Awazu, C. Rockstuhl, M. Fujimaki, N. Fukuda, J. Tominaga, T. Komatsubara, T. Ikeda, and Y. Ohki, "High sensitivity sensors made of perforated waveguides," Opt. Express **15**, 2592-2597 (2007).

70. G. G. Rong, J. D. Ryckman, R. L. Mernaugh, and S. M. Weiss, "Label-free porous silicon membrane waveguide for DNA sensing," Appl. Phys. Lett. **93**(2008).

71. Y. Jiao and S. M. Weiss, "Design parameters and sensitivity analysis of polymer-cladded porous silicon waveguides for small molecule detection," Biosens. Bioelectron. **25**, 1535-1538 (2010).

72. J. Xia, A. M. Rossi, and T. E. Murphy, "Laser-written nanoporous silicon ridge waveguide for highly sensitive optical sensors," Opt. Lett. **37**, 256-258 (2012).

73. P. C. Searson and J. M. Macaulay, "The fabrication of porous silicon structures," Nanotechnology **3**, 188-191 (1992).

74. K. H. Jung, S. Shih, and D. L. Kwong, "Developments in Luminescent Porous Si," J. Electrochem. Soc. **140**, 3046-3064 (1993).

75. V. Lehmann and U. Gosele, "Porous Silicon Formation - a Quantum Wire Effect," Appl. Phys. Lett. **58**, 856-858 (1991).

76. R. L. Smith and S. D. Collins, "Porous Silicon Formation Mechanisms," J. Appl. Phys. **71**, R1-R22 (1992).

77. X. G. Zhang, "Morphology and formation mechanisms of porous silicon," J. Electrochem. Soc. **151**, C69-C80 (2004).

78. H. Gerischer, "The Impact of Semiconductors on the Concepts of Electrochemistry," Electrochim. Acta **35**, 1677-1699 (1990).

79. P. Allongue, in *Properties of Porous Silicon*, L. T. Canham, ed. (IEE INSPEC, London, UK, 1997).

80. R. Herino, G. Bomchil, K. Barla, and C. Bertrand, "Porosity and pore size distribution of porous silicon layers," J. Electrochem. Soc. **134**, 1994-2000 (1987).

81. V. Lehmann and John Wiley & Sons., "The electrochemistry of silicon instrumentation, science, materials and applications," (Wiley-VCH, Weinheim, 2002).

82. J. E. Lugo, H. A. Lopez, S. Chan, and P. M. Fauchet, "Porous silicon multilayer structures: A photonic band gap analysis," J. Appl. Phys. **91**, 4966-4972 (2002).

83. M. G. Berger, C. Dieker, M. Thonissen, L. Vescan, H. Luth, H. Munder, W. Theiss, M. Wernke, and P. Grosse, "Porosity Superlattices - a New Class of Si Heterostructures," J. Phys. D: Appl. Phys. **27**, 1333-1336 (1994).

84. M. G. Berger, M. Thonissen, R. Arensfischer, H. Munder, H. Luth, M. Arntzen, and W. Theiss, "Investigation and Design of Optical-Properties of Porosity Superlattices," Thin Solid Films **255**, 313-316 (1995).

85. H. F. Arrand, "Optical waveguides and components based on porous silicon," PhD thesis (University of Nottingham, 1997).

86. A. W. Snyder and J. D. Love, *Optical waveguide theory* (Chapman and Hall, London ; New York, 1983).

87. R. Paschotta, *Encyclopedia of laser physics and technology* (Wiley-VCH, Weinheim, 2008).

88. C. R. Pollock, *Fundamentals of optoelectronics* (Irwin, Chicago, 1995).

89. A. Bruyant, I. Stefanon, G. Lerondel, S. Blaize, S. Aubert, R. Bachelot, P. Royer, P. Pirasteh, J. Charrier, and P. Joubert, "Light propagation in a porous silicon waveguide: an optical modes analysis in near-field," Phys. Status Solidi A **202**, 1417-1421 (2005).

90. R. E. Dessy, "Waveguides as chemical sensors," Anal. Chem. **61**, 1079A-1094A (1989).

91. E. Gizeli and C. R. Lowe, "Biomolecular sensors," (Taylor & Francis, London ; New York, 2002).

92. S. J. McNab, N. Moll, and Y. A. Vlasov, "Ultra-low loss photonic integrated circuit with membrane-type photonic crystal waveguides," Opt. Express **11**, 2927-2939 (2003).

93. M. P. Joshi, H. E. Pudavar, J. Swiatkiewicz, P. N. Prasad, and B. A. Reianhardt, "Three-dimensional optical circuitry using two-photon-assisted polymerization," Appl. Phys. Lett. **74**, 170-172 (1999).

94. P. K. Tien, R. Ulrich, and R. J. Martin, "Modes of Propagating Light Waves in Thin Deposited Semiconductor Films," Appl. Phys. Lett. **14**, 291-294 (1969).

95. R. Ulrich and R. Torge, "Measurement of Thin-Film Parameters with a Prism Coupler," Appl. Opt. **12**, 2901-2908 (1973).

96. R. T. Kersten, "Prism-Film Coupler as a Precision Instrument .1. Accuracy and Capabilities of Prism Couplers as Instruments," Optica Acta **22**, 503-513 (1975).

97. I. Mihalcescu, G. Lerondel, and R. Romestain, "Porous silicon anisotropy investigated by guided light," Thin Solid Films **297**, 245-249 (1997).

98. J. Charrier, E. Le Gorju, L. Haji, and M. Guendouz, "Optical waveguides fabricated from oxidised porous silicon," J. Porous Mater. **7**, 243-246 (2000).

99. R. Shubert and J. H. Harris, "Optical Surface Waves on Thin Films and Their Application to Integrated Data Processors," IEEE Trans. Microwave Theory Tech. **16**, 1048-1054 (1968).

100. P. K. Tien, "Light Waves in Thin Films and Integrated Optics," Appl. Opt. **10**, 2395-2413 (1971).

101. J. W. Goodman, *Introduction to Fourier optics,* 3rd ed. (Roberts & Co. Publishers, Englewood, Colo., 2005).

102. M. L. Dakss, L. Kuhn, P. F. Heidrich, and B. A. Scott, "Grating Coupler for Efficient Excitation of Optical Guided Waves in Thin Films," Appl. Phys. Lett. **16**, 523-525 (1970).

103. M. Hagberg, N. Eriksson, and A. Larsson, "High efficiency surface emitting lasers using blazed grating outcouplers," Appl. Phys. Lett. **67**, 3685-3687 (1995).

104. C. Fattinger, "The Bidiffractive Grating Coupler," Appl. Phys. Lett. **62**, 1460-1462 (1993).

105. R. Waldhausl, B. Schnabel, P. Dannberg, E. B. Kley, A. Brauer, and W. Karthe, "Efficient coupling into polymer waveguides by gratings," Appl. Opt. **36**, 9383-9390 (1997).

106. R. G. Heideman, R. P. H. Kooyman, and J. Greve, "Performance of a Highly Sensitive Optical Wave-Guide Mach-Zehnder Interferometer Immunosensor," Sens. Actuators, B **10**, 209-217 (1993).

107. W. Lukosz and K. Tiefenthaler, "Sensitivity of Integrated Optical Grating and Prism Couplers as (Bio)Chemical Sensors," Sens. Actuators **15**, 273-284 (1988).

108. A. Brandenburg, R. Polzius, F. Bier, U. Bilitewski, and E. Wagner, "Direct observation of affinity reactions by reflected-mode operation of integrated optical grating coupler," Sens. Actuators, B **30**, 55-59 (1996).

109. R. Polzius, T. Schneider, F. F. Bier, U. Bilitewski, and W. Koschinski, "Optimization of biosensing using grating couplers: Immobilization on tantalum oxide waveguides," Biosens. Bioelectron. **11**, 503-514 (1996).

110. R. Polzius, E. Diessel, F. F. Bier, and U. Bilitewski, "Real-time observation of affinity reactions using grating couplers: Determination of the detection limit and calculation of kinetic rate constants," Anal. Biochem. **248**, 269-276 (1997).

111. P. Kozma, A. Hamori, K. Cottier, S. Kurunczi, and R. Horvath, "Grating coupled interferometry for optical sensing," Appl. Phys. B **97**, 5-8 (2009).

112. R. E. Kunz and K. Cottier, "Optimizing integrated optical chips for label-free (bio-)chemical sensing," Anal. Bioanal.Chem. **384**, 180-190 (2006).

113. J. H. Schmid, W. Sinclair, J. Garcia, S. Janz, J. Lapointe, D. Poitras, Y. Li, T. Mischki, G. Lopinski, P. Cheben, A. Delage, A. Densmore, P. Waldron, and D. X. Xu, "Silicon-on-insulator guided mode resonant grating for

evanescent field molecular sensing," Opt. Express **17**, 18371-18380 (2009).

114. R. Magnusson, D. Wawro, S. Zimmerman, and Y. W. Ding, "Resonant Photonic Biosensors with Polarization-Based Multiparametric Discrimination in Each Channel," Sensors **11**, 1476-1488 (2011).

115. D. J. Sirbuly, A. Tao, M. Law, R. Fan, and P. D. Yang, "Multifunctional nanowire evanescent wave optical sensors," Adv. Mater. **19**, 61 (2007).

116. X. Wei, C. Kang, G. Rong, S. T. Retterer, and S. M. Weiss, "Porous silicon waveguide with integrated grating coupler for DNA sensing," Proc. SPIE **7167**, 71670C (2009).

117. T. Strother, W. Cai, X. S. Zhao, R. J. Hamers, and L. M. Smith, "Synthesis and characterization of DNA-modified silicon (111) surfaces," J. Am. Chem. Soc. **122**, 1205-1209 (2000).

118. M. C. Pirrung, "How to make a DNA chip," Angewandte Chemie-International Edition **41**, 1277 (2002).

119. E. D. Palik, *Handbook of optical constants of solids*, Academic Press handbook series (Academic Press, Orlando, 1985).

120. Z. Lin, T. Strother, W. Cai, X. P. Cao, L. M. Smith, and R. J. Hamers, "DNA attachment and hybridization at the silicon (100) surface," Langmuir **18**, 788-796 (2002).

121. B. R. Hart, S. E. Letant, S. R. Kane, M. Z. Hadi, S. J. Shields, and J. G. Reynolds, "New method for attachment of biomolecules to porous silicon," Chem. Commun., 322-323 (2003).

122. N. M. Ravindra, J. Narayan, D. Fathy, J. K. Srivastava, and E. A. Irene, "Silicon oxidation and Si–SiO2 interface of thin oxides," J. Mater. Res. **2**, 216-221 (1987).

123. T. Unagami, "Oxidation of Porous Silicon and Properties of Its Oxide Film," Japanese Journal of Applied Physics **19**, 231-241 (1980).

124. J. Salonen, V. P. Lehto, and E. Laine, "Thermal oxidation of free-standing porous silicon films," Appl. Phys. Lett. **70**, 637 (1997).

125. X. Wei, C. Kang, M. Liscidini, G. Rong, S. T. Retterer, M. Patrini, J. E. Sipe, and S. M. Weiss, "Grating couplers on porous silicon planar waveguides for sensing applications," J. Appl. Phys. **104**(2008).

126. P. Yeh, *Optical waves in layered media*, Wiley series in pure and applied optics (Wiley, New York, 1988).

127. M. G. Moharam, D. A. Pommet, E. B. Grann, and T. K. Gaylord, "Stable Implementation of the Rigorous Coupled-Wave Analysis for Surface-Relief Gratings - Enhanced Transmittance Matrix Approach," J. Opt. Soc. Am. A: Opt Image Sci Vis **12**, 1077-1086 (1995).

128. R. J. Stockermans and P. L. Rochon, "Narrow-band resonant grating waveguide filters constructed with azobenzene polymers," Appl. Opt. **38**, 3714-3719 (1999).

129. S. Fan and J. D. Joannopoulos, "Analysis of guided resonances in photonic crystal slabs," Phys. Rev. B **65**, 235112 (2002).

130. H. Ouyang, C. C. Striemer, and P. M. Fauchet, "Quantitative analysis of the sensitivity of porous silicon optical biosensors," Appl. Phys. Lett. **88**(2006).

131. B. H. Clare and N. L. Abbott, "Orientations of nematic liquid crystals on surfaces presenting controlled densities of peptides: amplification of protein-peptide binding events," Langmuir **21**, 6451-6461 (2005).

132. J. L. Lawrie, Y. Jiao, and S. M. Weiss, "Size-Dependent Infiltration and Optical Detection of Nucleic Acids in Nanoscale Pores," IEEE Trans. Nanotechnol. **9**, 596-602 (2010).

133. G. Rong and S. M. Weiss, "Biomolecule size-dependent sensitivity of porous silicon sensors," Phys. Status Solidi A **206**, 1365-1368 (2009).

134. J. L. Lawrie, Z. Xu, G. G. Rong, P. E. Laibinis, and S. M. Weiss, "Synthesis of DNA oligonucleotides in mesoporous silicon," Phys. Status Solidi A **206**, 1339-1342 (2009).

135. X. Wei and S. M. Weiss, "Guided mode biosensor based on grating coupled porous silicon waveguide," Opt. Express **19**, 11330-11339 (2011).

136. S. Grego, J. R. McDaniel, and B. R. Stoner, "Wavelength interrogation of grating-based optical biosensors in the input coupler configuration," Sens. Actuators, B **131**, 347-355 (2008).

137. M. Egholm, O. Buchardt, L. Christensen, C. Behrens, S. M. Freier, D. A. Driver, R. H. Berg, S. K. Kim, B. Norden, and P. E. Nielsen, "Pna Hybridizes to Complementary Oligonucleotides Obeying the Watson-Crick Hydrogen-Bonding Rules," Nature **365**, 566-568 (1993).

138. A. W. Peterson, R. J. Heaton, and R. M. Georgiadis, "The effect of surface probe density on DNA hybridization," Nucleic Acids Res. **29**, 5163-5168 (2001).

139. S. Elhadj, G. Singh, and R. F. Saraf, "Optical properties of an immobilized DNA monolayer from 255 to 700 nm," Langmuir **20**, 5539-5543 (2004).

140. J. D. Ryckman, M. Liscidini, J. E. Sipe, and S. M. Weiss, "Direct Imprinting of Porous Substrates: A Rapid and Low-Cost Approach for Patterning Porous Nanomaterials," Nano Lett. **11**, 1857-1862 (2011).

141. X. Wei and S. M. Weiss, "Grating Coupled Waveguide Biosensor Based on Porous Silicon," MRS Proceedings **1301**, mrsf10-1301-pp1303-1309 (2011).

142. P. Pirasteh, J. Charrier, Y. Dumeige, S. Haesaert, and P. Joubert, "Optical loss study of porous silicon and oxidized porous silicon planar waveguides," J. Appl. Phys. **101**, 083110 (2007).

143. Y. D. Yin and X. S. Zhao, "Kinetics and Dynamics of DNA Hybridization," Acc. Chem. Res. **44**, 1172-1181 (2011).

144. J. J. Ramsden, S. Y. Li, J. E. Prenosil, and E. Heinzle, "Kinetics of Adhesion and Spreading of Animal-Cells," Biotechnol. Bioeng. **43**, 939-945 (1994).

145. N. Darwish, D. Caballero, M. Moreno, A. Errachid, and J. Samitier, "Multi-analytic grating coupler biosensor for differential binding analysis," Sens. Actuators, B **144**, 413-417 (2010).

146. N. Kim, I. S. Park, and W. Y. Kim, "Salmonella detection with a direct-binding optical grating coupler immunosensor," Sens. Actuators, B **121**, 606-615 (2007).

147. V. Goral, Q. Wu, H. Y. Sun, and Y. Fang, "Label-free optical biosensor with microfluidics for sensing ligand-directed functional selectivity on trafficking of thrombin receptor," FEBS Lett. **585**, 1054-1060 (2011).

148. P. Kozma, A. Hamori, S. Kurunczi, K. Cottier, and R. Horvath, "Grating coupled optical waveguide interferometer for label-free biosensing," Sens. Actuators, B **155**, 446-450 (2011).

149. K. Schmitt, B. Schirmer, C. Hoffmann, A. Brandenburg, and P. Meyrueis, "Interferometric biosensor based on planar optical waveguide sensor chips for label-free detection of surface bound bioreactions," Biosens. Bioelectron. **22**, 2591-2597 (2007).

150. J. Voros, J. J. Ramsden, G. Csucs, I. Szendro, S. M. De Paul, M. Textor, and N. D. Spencer, "Optical grating coupler biosensors," Biomaterials **23**, 3699-3710 (2002).

151. T. Claes, W. Bogaerts, and P. Bienstman, "Vernier-cascade label-free biosensor with integrated arrayed waveguide grating for wavelength interrogation with low-cost broadband source," Opt. Lett. **36**, 3320-3322 (2011).

152. Z. A. Lai, Y. L. Wang, N. Allbritton, G. P. Li, and M. Bachman, "Label-free biosensor by protein grating coupler on planar optical waveguides," Opt. Lett. **33**, 1735-1737 (2008).

153. J. N. Yih, Y. M. Chu, Y. C. Mao, W. H. Wang, F. C. Chien, C. Y. Lin, K. L. Lee, P. K. Wei, and S. J. Chen, "Optical waveguide biosensors constructed with subwavelength gratings," Appl. Opt. **45**, 1938-1942 (2006).

154. H. N. Daghestani and B. W. Day, "Theory and Applications of Surface Plasmon Resonance, Resonant Mirror, Resonant Waveguide Grating, and Dual Polarization Interferometry Biosensors," Sensors **10**, 9630-9646 (2010).

155. T. D. Lazzara, I. Mey, C. Steinem, and A. Janshoff, "Benefits and Limitations of Porous Substrates as Biosensors for Protein Adsorption," Anal. Chem. **83**, 5624-5630 (2011).

156. A. W. Marczewski, "Analysis of Kinetic Langmuir Model. Part I: Integrated Kinetic Langmuir Equation (IKL): A New Complete Analytical Solution of the Langmuir Rate Equation," Langmuir **26**, 15229-15238 (2010).

157. G. M. Whitesides, E. Ostuni, S. Takayama, X. Y. Jiang, and D. E. Ingber, "Soft lithography in biology and biochemistry," Annual Review of Biomedical Engineering **3**, 335-373 (2001).

158. J. C. McDonald and G. M. Whitesides, "Poly(dimethylsiloxane) as a material for fabricating microfluidic devices," Acc. Chem. Res. **35**, 491-499 (2002).

159. H. K. Wu, B. Huang, and R. N. Zare, "Construction of microfluidic chips using polydimethylsiloxane for adhesive bonding," Lab Chip **5**, 1393-1398 (2005).

160. J. W. Mares and S. M. Weiss, "Diffusion dynamics of small molecules from mesoporous silicon films by real-time optical interferometry," Appl. Opt. **50**, 5329-5337 (2011).

161. Y. Gao, L. K. Wolf, and R. M. Georgiadis, "Secondary structure effects on DNA hybridization kinetics: a solution versus surface comparison," Nucleic Acids Res. **34**, 3370-3377 (2006).

162. H. Matsuyama, M. Teramoto, and K. Suzuki, "Simulation of solute diffusion through porous media," Sep. Sci. Technol. **32**, 2349-2366 (1997).

163. A. E. Nkodo, J. M. Garnier, B. Tinland, H. J. Ren, C. Desruisseaux, L. C. McCormick, G. Drouin, and G. W. Slater, "Diffusion coefficient of DNA molecules during free solution electrophoresis," Electrophoresis **22**, 2424-2432 (2001).

164. J. H. Park and N. R. Aluru, "Water film thickness-dependent conformation and diffusion of single-strand DNA on poly(ethylene glycol)-silane surface," Appl. Phys. Lett. **96**(2010).

165. E. S. Jeng, A. E. Moll, A. C. Roy, J. B. Gastala, and M. S. Strano, "Detection of DNA hybridization using the near-infrared band-gap fluorescence of single-walled carbon nanotubes," Nano Lett. **6**, 371-375 (2006).

166. F. Giorgis, E. Descrovi, C. Summonte, L. Dominici, and F. Michelotti, "Experimental determination of the sensitivity of Bloch Surface Waves based sensors," Opt. Express **18**, 8087-8093 (2010).

167. H. Qiao, B. Guan, J. J. Gooding, and P. J. Reece, "Protease detection using a porous silicon based Bloch surface wave optical biosensor," Opt. Express **18**, 15174-15182 (2010).

168. E. Descrovi, T. Sfez, M. Quaglio, D. Brunazzo, L. Dominici, F. Michelotti, H. P. Herzig, O. J. F. Martin, and F. Giorgis, "Guided Bloch Surface Waves on Ultrathin Polymeric Ridges," Nano Lett. **10**, 2087-2091 (2010).

169. V. N. Konopsky and E. V. Alieva, "Photonic crystal surface waves for optical biosensors," Anal. Chem. **79**, 4729-4735 (2007).